LOCAL FIELD ENHANCEMENT OF DIFFERENT CORE SHELL NANO-PARTICLES PLACED OVER A SUBSTRATE UNDER AN AFM TIP

by
Dilan Avşar
B.S., Mechanical Engineering, Boğaziçi University, 2016
B.S., Physics, Boğaziçi University, 2016

Submitted to the Institute for Graduate Studies in
Science and Engineering in partial fulfillment of
the requirements for the degree of
Master of Science

Graduate Program in Mechanical Engineering
Boğaziçi University
2019

ACKNOWLEDGEMENTS

Firstly, I would like to express my deepest gratitude and respect to my advisor, Prof. Hakan Ertürk, for his patience, motivation, and inspiring ideas during my 3 years long bumpy road of thesis study. In fact, without the discipline and working principle, which I have gained during well-organized weekly meetings with my advisor and TES-LAB colleagues, this study would never come to end. I feel so lucky that I had a chance to interact with wise and considerate people from the beginning of my academic study. I am also so grateful to my co-advisor, Prof. M. Pınar Mengüç, who supported me with the encouragement and envisions. I would like to thank Sina Talebi Moghaddam, with whom I collaborated in my very first academic research, for sharing the knowledge and experience. Moreover, I can't express my gratitude enough to Prof. M. Burçin Ünlü, who sprightly taught the real-life applications of physics with intriguing questions and led me to continue with scientific research.

I would also like to express my gratitude and love to my families both with and without genetic linkage. I felt never alone thanks to their never-ending supports. And I appreciate their patience and hopefulness during really hard times. I would also thank to my little students, whom I believe to see in good places in the future, for unknowingly helping me to be a responsible person and teacher.

This work has not been supported by any institution, which I am still thankful for: letting me learn how to put things in track and figure a way out of difficulties.

Once and for all, I would like to dedicate this thesis to my soulmate, Mehmet, for his existence, deep understanding, and wholehearted support throughout my thesis period.

ABSTRACT

LOCAL FIELD ENHANCEMENT OF DIFFERENT CORE SHELL NANO-PARTICLES PLACED OVER A SUBSTRATE UNDER AN AFM TIP

Metal nanoparticles (NPs) interacting with the light in near-field undergoes localized surface plasmon resonance (LSPR) when the oscillating charges on the surfaces resonates with the incident light frequency. The EM wave illumination at resonance wavelength will result in field localization and absorption enhancement with localized heating. Absorption enhancement and LSPR wavelength of nanoparticles can be analyzed with the hybrid structures such as core-shell NPs made of dielectric and metals. The scope of thesis is the absorption behavior of core-shell NPs placed on a glass substrate illuminated by total internal reflection,which creates surface evanescent waves. The near-field coupling of core-shell NP is analyzed by changing the material compositions at core and shell with different size configurations, which is called volumetric filling ratio of the core. The LSPR wavelength tunability and effective absorption efficiency values of each pair are analyzed with respect to their size parameter. Moreover, the sensitivity study of bimetallic core-shell NPs to changes in the refractive index of the medium showed that increasing the dielectric medium refractive index can result in increase in field intensity and red-shift of the LSPR wavelengths. For the localized heating purposes, core-shell NPs are also considered with the AFM tip placed over the NP. For this, wave polarizations and tip materials are compared for the spectral absorption behavior of the NPs. It is shown that NPs can have multipeak resonance either with absorption enhancement or damping. Designated problems are numerically investigated by using an open source $MATLAB^{TM}$ toolbox, which is the vectorized version of the discrete dipole approximation with surface interaction (DDA-SI-v).

ÖZET

AKM UCU ALTINDA DİELEKTRİK YÜZEYE YERLEŞTİRİLEN FARKLI ÇEKİRDEK KABUKLU NANOPARÇACIKLARIN LOKAL ALAN GELİŞTİRMESİ

Yakın alanda ışıkla etkileşime giren metal nanoparçacıklar, yüzeyindeki salınımlı yüklerin gelen ışın frekansıyla rezonansa girmesi ile bölgesel yüzey plazmon rezonansına uğrarlar. Rezonans dalga boyundaki elektromanyetik dalga aydınlatması ile alan lokalizasyonu ve soğurma artışlı bölgesel ısıtma oluşur. Nanoparçacıkların soğurma artışı ve plazmon rezonans dalga boyları, dielektrik ve metalden oluşan çekirdek-kabuklu nanoparçacıklar gibi hibrit yapılar ile incelenebilir. Bu tezin kapsamı toplam iç yansımayla genliği azalan dalgaların oluştuğu cam yüzey üzerinde çekirdek-kabuklu nanoparçacıkların soğurma davranışlarıdır. Nanoparçacıkların malzeme bileşimi ve çekirdek maddenin volumetrik doldurma oranları değiştirilerek yakın-alan kuplajı incelendi. Her parçanın boyut parametrelerine göre rezonans dalga boyu ayarlanabilirliği ve soğurma verimi analiz edildi. Bimetalik yapıların duyarlık çalışması, artan dielektrik ortam kırılma indisinin alan şiddetini arttırdığını ve rezonans dalga boylarını kırmızıya kaydırdığını gösterdi. Bölgesel ısıtılması amacıyla, çekirdek-kabuklu nanoparçacıklar üzerindeki atomik kuvvet mikroskobu (AKM) ucu ile düşünüldü. Bu yüzden nanoparçacıkların spektral soğurma davranışları için dalga polarizasyonları ve uç malzemeleri karşılaştırıldı. Nanoparçacıkların çift tepeli rezonanslarında soğurma artımı veya sönümünün olduğu görüldü. Problemlerin sayısal incelemeleri açık kaynaklı $MATLAB^{TM}$ aracı olan ‘vektörleştirilmiş yüzey etkileşimli ayrık dipol yaklaşımı (DDA-SI-v)’ kullanılarak yapıldı.

TABLE OF CONTENTS

ACKNOWLEDGEMENTS iii
ABSTRACT iv
ÖZET v
LIST OF FIGURES viii
LIST OF TABLES xiv
LIST OF SYMBOLS xv
LIST OF ACRONYMS/ABBREVIATIONS xvii
1. INTRODUCTION 1
  1.1. Nanotechnology 1
  1.2. Near Field Thermal Radiation 2
  1.3. Applications 3
    1.3.1. Nanopatterning and Local Heating 5
  1.4. Core-Shell Nanoparticles 8
    1.4.1. Metal/Dielectric Core-Shell Pairs 9
    1.4.2. Bimetallic Core-Shell Pairs 10
  1.5. Objective 10
2. THEORY AND NUMERICAL METHODS 13
  2.1. Theory 13
    2.1.1. Fluctuational Electrodynamics and Fluctuation-Dissipation Theorem 13
  2.2. Electromagnetic Local Density of States (LDOS) 15
    2.2.1. Surface Phonon-Polariton and Surface Plasmon-Polariton 16
  2.3. Numerical Methods 17
    2.3.1. DDA-SI and DDA-SI-v 18
3. METALLIC/DIELECTRIC CORE-SHELL NANOPARTICLES ON A DIELECTRIC SUBSTRATE 21
  3.1. Problem Statement 21
  3.2. Numerical Aspects 23
  3.3. Results and Discussions 23

3.3.1. Dielectric Core with Metal Shell 25
3.3.2. Metallic Core with Dielectric Shell 30
4. ABSORPTION AND PLASMON RESONANCE OF BI-METALLIC CORE-SHELL NANOPARTICLES ON A DIELECTRIC SUBSTRATE 34
4.1. Problem Statement and Method 34
4.2. Numerical Aspects 37
4.3. Results and Discussions 37
4.3.1. Fixed Core and Fixed Nanoparticle Size 37
4.3.2. Refractive Index Sensitivity 40
4.3.3. AFM Tip and Nanoparticle Interaction 42
5. CONCLUSIONS AND FUTURE WORK 50
5.1. Conclusions 50
5.2. Future Work 52
REFERENCES 54
APPENDIX A: OPTICAL DATA OF THE NANOPARTICLES 63
APPENDIX B: FREE SPACE COMPARISONS OF METAL NANOPARTICLES 64
APPENDIX C: ADDITIONAL PLOTS: FNP 68
C.1. Dielectric Core - Metal Shell 68
C.2. Metal Core - Dielectric Shell 70
APPENDIX D: FIXED CORE CASES WITH AFM AND TM-WAVE 72
D.1. Selected Pair: Ag@GaP Under GaP AFM Tip 75

LIST OF FIGURES

Figure 1.1. Sketch of EM field interaction between (a) single particle, and pair of particles aligned (b) parallel, and (c) perpendicular with respect to the field. 6

Figure 2.1. Illustration of near-field radiative heat exchange between plates due to (a) coupled surface polariton modes, (b) propagating waves, (c) evanescent fields by total internal reflection (TIR). 16

Figure 2.2. Spherical particle represented with N = 81, 552, 7208. 18

Figure 2.3. A schematic view of incident TM (a), and TE (b) polarized waves being incident below the dielectric substrate with total internal reflection that creates surface evanescent waves decaying in z-direction. 19

Figure 3.1. A schematic view of the configuration for single core-shell system being represented with core radius (R_c) and outer shell radius (R_s). TE-polarized wave is incident with an angle greater than the critical angle (θ_c) for TIR under the BK7 substrate that creates surface evanescent wave propagating and decaying in y- and z-directions, respectively. 21

Figure 3.2. Ag shell with GaP (a-b) and SiO_2 (c-d) core: Contour plots of absorption efficiency as a function of wavelength for FC (a,c). Maximum Q_{abs} and LSPR wavelengths, λ_{max}, as a function of f_r for FC and FNP (b,d). 25

Figure 3.3. Au shell with GaP (a-b) and SiO_2 (c-d) core: Contour plots of absorption efficiency as a function of wavelength for FC (a,c). Maximum Q_{abs} and LSPR wavelengths, λ_{max}, as a function of f_r for FC and FNP (b,d). 26

Figure 3.4. Normalized field intensity plots for SiO_2 core/ Au shell (a-c) and Au core/ GaP shell (d-f) NPs with a cut on x = 0 plane and D_s = 50 nm. Each case is shown with respect to k-vector direction. (a) $D_c = 15$ nm, $\lambda_{max} = 515$ nm, maximum $Q_{abs} = 1.04$. (b) $D_c = 33$ nm, $\lambda_{max} = 535$ nm, maximum $Q_{abs} = 1.34$. (c) $D_c = 45$ nm, $\lambda_{max} = 640$ nm, maximum $Q_{abs} = 1.06$. (d) $D_c = 15$ nm, $\lambda_{max} = 300$ nm, maximum $Q_{abs} = 0.58$. (e) $D_c = 27$ nm, $\lambda_{max} = 705$ nm, maximum $Q_{abs} = 1.12$. (f) $D_c = 33$ nm, $\lambda_{max} = 660$ nm, maximum $Q_{abs} = 1.61$. 29

Figure 3.5. Ag core with GaP (a-b) and SiO_2 (c-d) shell: Contour plots of absorption efficiency as a function of wavelength for FC (a,c). Maximum Q_{abs} and LSPR wavelengths, λ_{max}, as a function of f_r for FC and FNP (b,d). 31

Figure 3.6. Au core with GaP (a-b) and SiO_2 (c-d) shell: Contour plots of absorption efficiency as a function of wavelength for FC (a,c). Maximum Q_{abs} and LSPR wavelengths, λ_{max}, as a function of f_r for FC and FNP (b,d). 33

Figure 4.1. A cross-sectional view of the AFM probe and nanoparticle configuration. 36

Figure 4.2. Spectral absorption efficiency,Q_{abs}, of Ag core-Au shell (a-b) and Au core-Ag shell (c-d), represented for FC (a,c) and FNP (b,d) cases. 38

Figure 4.3. Ag core-Au shell (a-b) and Au core-Ag shell (c-d): Contour plots of spectral absorption efficiency, Q_{abs}, for FC (a,c). Maximum Q_{abs} and LSPR wavelengths, λ_{max}, with respect to volumetric filling ratio, f_r, for both FC and FNP cases (b,d). 39

Figure 4.4. Spectral absorption efficiency, Q_{abs}, for Ag@Au (a-c) and Au@Ag (d-f) in mediums with n_m= 1 (a,d), 1.25 (b,e), and 1.5 (c,f). . . . 40

Figure 4.5. Maximum Q_{abs} and LSPR wavelengths, λ_{max}, with respect to medium refractive indices, n_m for both both Ag@Au and Au@Ag. 42

Figure 4.6. Converged absorption efficiency, Q_{abs}, values of AuNP with changes in AFM shaft length. 43

Figure 4.7. Spectral absorption efficiency, Q_{abs}, of AgNP (a) and AuNP (b) under the effect of GaP and Si AFM tips with TE/TM-polarizations. 45

Figure 4.8. Spectral absorption efficiency, Q_{abs}, of core-shell pairs: Ag@Au (a) and Au@Ag (b) with and without using GaP AFM tip in TE/TM-polarization cases. 46

Figure 4.9. Normalized field intensity plots of Au@Ag illuminated with TE (a-c) and TM (d-f) polarized wave: (a,d) at λ=370 nm without AFM tip, (b,e) λ=370 nm and (c,f) λ=490 nm with GaP AFM tip. . . . 47

Figure 4.10. Normalized field intensity plots of Ag@Au with TE (a,b) and TM (c,d) polarized wave at λ=380 nm: (a,c) without AFM tip and (b,d) with GaP AFM tip. 48

Figure A.1. Spectral refractive indices of silver, gold, and copper. 63

Figure A.2. Spectral refractive indices of Gallium phosphide (GaP), Silicon dioxide (SiO_2), and Borosilicate glass (BK7). 63

Figure B.1. Absorption efficiency comparisons of single silver nanoparticle in free space approximated by different number of dipoles, N, using DDSCAT and DDA. 64

Figure B.2. Free space comparison of DDA method with Mie theory for spectral absorption, scattering, and extinction efficiency values of silver nanoparticle, AgNP, in 50 nm diameter. 65

Figure B.3. Free space comparison of DDA method with Mie theory for spectral absorption, scattering, and extinction efficiency values of gold nanoparticle, AuNP, in 50 nm diameter. 66

Figure B.4. Free space comparison of DDA method with Mie theory for spectral absorption, scattering, and extinction efficiency values of copper nanoparticle, CuNP, in 50 nm diameter. 67

Figure C.1. GaP core with Ag shell with D_s=50 nm: Contour plot of absorption efficiency as a function of wavelength for FNP size. 68

Figure C.2. GaP core with Au shell with D_s=50 nm: Contour plot of absorption efficiency as a function of wavelength for FNP size. 68

Figure C.3. SiO_2 core with Ag shell with D_s=50 nm: Contour plot of absorption efficiency as a function of wavelength for FNP size. 69

Figure C.4. SiO_2 core with Au shell with D_s=50 nm: Contour plot of absorption efficiency as a function of wavelength for FNP size. 69

Figure C.5. Ag core with GaP shell with D_s=50 nm: Contour plot of absorption efficiency as a function of wavelength for FNP size. 70

Figure C.6. Ag core with SiO_2 shell with D_s=50 nm: Contour plot of absorption efficiency as a function of wavelength for FNP size. 70

Figure C.7. Au core with GaP shell with D_s=50 nm: Contour plot of absorption efficiency as a function of wavelength for FNP size. 71

Figure C.8. Au core with SiO_2 shell with D_s=50 nm: Contour plot of absorption efficiency as a function of wavelength for FNP size. 71

Figure D.1. Spectral Q_{abs} values for single AgNP, and dielectric pairs with both Ag core and Ag shell under Si AFM tip at coordinate (0, 0, 52) nm. Fixed size with D_c=20 nm, D_s=50 nm for core-shell NPs. 72

Figure D.2. Spectral Q_{abs} values for single AgNP, and dielectric pairs with both Ag core and Ag shell under GaP AFM tip at coordinate (0, 0, 52) nm. Fixed size with D_c=20 nm, D_s=50 nm for core-shell NPs. . . 72

Figure D.3. Spectral Q_{abs} values for single AuNP, and dielectric pairs with both Au core and Au shell under Si AFM tip at coordinate (0, 0, 52) nm. Fixed size with D_c=20 nm, D_s=50 nm for core-shell NPs. . . 73

Figure D.4. Spectral Q_{abs} values for single AuNP, and dielectric pairs with both Au core and Au shell under GaP AFM tip at coordinate (0, 0, 52) nm. Fixed size with D_c=20 nm, D_s=50 nm for core-shell NPs. . . 73

Figure D.5. Spectral Q_{abs} values for single CuNP, and dielectric pairs with both Cu core and Cu shell under Si AFM tip at coordinate (0, 0, 52) nm. Fixed size with D_c=20 nm, D_s=50 nm for core-shell NPs. . . 74

Figure D.6. Spectral Q_{abs} values for single CuNP, and dielectric pairs with both Cu core and Cu shell under GaP AFM tip at coordinate (0, 0, 52) nm. Fixed size with D_c=20 nm, D_s=50 nm for core-shell NPs. . . 74

Figure D.7. Spectral Q_{abs} values of Ag core-GaP shell FC cases under an GaP tip. Shell thickness, t_s, is varied between 0-15 nm. 75

Figure D.8. Spectral Q_{abs} values of Ag core-GaP shell FC cases under an GaP tip. Shell thickness, t_s, is varied between 0-15 nm. 75

Figure D.9. Normalized field intensity plots of (a) single AgNP (D=20 nm) without the tip, (b) single AgNP (D=20 nm) with GaP tip, (c) Ag core-GaP shell D_c=20 nm, t_s=2.5 nm, with GaP tip, (d) Ag core-GaP shell D_c=20 nm, t_s=2.5 nm, with GaP tip. 76

LIST OF TABLES

Table 1.1. Present and Potential Impacts of the Developing Technologies . . . 2

Table 3.1. Core and shell sizes for FC and FNP cases of metallic-dielectric NPs with corresponding volumetric filling ratio (f_r) ranges. 22

Table 4.1. Core and shell sizes for FC and FNP cases of bimetallic NPS with corresponding volumetric filling ratio (f_r) ranges. 35

Table 4.2. Refractive indices of the medium, n_m, and corresponding incident angles, θ_i. 35

Table 4.3. Summary of the maximum absorption efficiency values of the nanoparticles with their LSPR peak wavelengths represented as Q_{abs} @ λ_{max}. 43

LIST OF SYMBOLS

a	Effective radius of sphere
A_{jk}	Interaction matrix
C_{abs}	Absorption cross-section
C_{sca}	Scattering cross-section
C_{ext}	Extinction cross-section
d	Lattice spacing
D_c	Core diameter
D_s	Outer shell diameter
D_{shaft}	Probe shaft diameter
E	Electric field strength
f_r	Volumetric filling ratio
H	Magnetic field strength
J	Current density
k	Imaginary part of the refractive index
k_e	Magnitude of the evanescent wave vector
k_o	Magnitude of the wave vector in vacuum
Kn	Knudsen number
l_e	Electronic mean free path
l_g	Mean free path of the gas
L_{shaft}	Truncated shaft length of the probe
n	Complex refractive index
n	Real part of the refractive index
n_m	Refractive index of the medium
N_{AFM}	Number of dipoles of the probe
N_{NP}	Number of dipoles of the nanoparticle
P	Dipole moment
Q_{abs}	Absorption efficiency
Q_{sca}	Scattering efficiency

Q_{ext}	Extinction efficiency
R_c	Core radius
R_s	Outer shell radius
$\vec{r}_j$	Point dipole coordinate
r_{tip}	Tip radius of the probe
$\vec{S}$	Poynting vector
t	Shell thickness
V	Volume of the sphere
α	Cone angle
ε_m	Dielectric function of medium
ε_o	Electric permittivity of free space
Θ	Average energy of an oscillator
θ_i	Incident wave angle
θ_c	Critical angle
λ_{max}	Resonance wavelength
λ_{th}	Thermally dominant wavelength
μ_o	Magnetic permeability of free space
ρ	Charge density
ω	Frequency

LIST OF ACRONYMS/ABBREVIATIONS

AFM	Atomic force microscope
AgNP	Silver nanoparticle
AuNP	Gold nanoparticle
BK7	Borosilicate glass
C@S	Core material in the shell material
CEM	Computational electromagnetic methods
DDA	Discrete dipole approximation
DGF	Dyadic Green's function
EM	Electromagnetic
FC	Fixed core size
FE	Fluctuational electrodynamics
FDT	Fluctuation-dissipation theorem
FNP	Fixed nanoparticle size
IR	Infrared
LDOS	Local density of states
LSPR	Localized surface plasmon resonance
NIR	Near-infrared
NP	Nanoparticle
SEM	Scanning electron microscope
SERS	Surface enhanced Raman spectroscopy
SNOM	Scanning near-field optical microscope
SPhP	Surface phonon-polariton
SPP	Surface plasmon-polariton
SPR	Surface plasmon resonance
TE	Transverse electric
TEM	Transmission electron microscope
TERS	Tip enhanced Raman spectroscopy
TIR	Total internal reflection

TM	Transverse magnetic
UV	Ultraviolet
VIS	Visible
XPS	X-ray photoelectron spectroscopy

1. INTRODUCTION

1.1. Nanotechnology

Nanoscale science and engineering are the emerging fields supported with the interdisciplinary studies after the discovery of new materials, which are being made of nanoscale building blocks (nanoparticles, nanotubes, nanolayers etc.), offering advanced performances of devices. The technology evolved within the nanoscale, which is in the range of 1 to 100 nanometers, also gave rise to develop new and efficient methods in manufacturing. Any given material property is associated with the material's bulk behavior until the critical length scale is exceeded. Hence, the behavior of the materials differs if it is considered at the nanoscale. With the discovery of size dependent properties of the materials in 80's, nanostructuring the materials for a specified functionality has been rapidly emerged over the world [1, 2]. Hence, the utilisation of the nanomaterials leads up a potential breakthrough in nanoengineering. While there are numerous applications in various industrial areas for engineering, there are also novel applications in nanoscience such as developing improved materials, and identification methods of nanosized materials.

There is a need for improved materials for challenging problems in both biomedical and energy applications. As listed in Table 1.1, nanoscale technology offers large variety of applications with their use as coatings, functional nanodevices, and high surface area materials. For instance, metallic nanoparticles are used as contrast agents for the biomedical applications such as imaging, labeling, and detecting due to their unique optical properties in nanoscale. Moreover, the use of nanoparticles is also important for targeted drug delivery, photothermal therapy, and photoacoustic imaging applications. [3–5]. Further researches in nanosized materials can promote the nanotechnology for the development of functional products.

Table 1.1. Present and Potential Impacts of the Developing Technologies [1].

Technology	Present Impact	Potential Impact
Dispersion and Coatings	Thermal barriers Optical (VIS/NIR) barriers Imaging enhancement Ink-jet materials	Targeted drug delivery Gene therapy Multifunctional nanocoating
High Surface Area Materials	Molecular sieves Drug delivery Tailored catalysts Absorption/desorption materials	Molecule-specific sensors Large hydrocarbon or bacterial filters Solar cells
Consolidated Materials	Low-loss soft magnetic materials Nanocomposite cements High hardness cutting tools	Superplastic forming of ceramics Ultrahigh-strength materials Nano filled polymer composites
Nano devices	GMR read heads	Terabit memory Micro processing Nanotubes for high brightness Biomedical sensors
Additional Biological Aspects	Bio-catalysts	Bioelectronics Bio inspired prostheses Single-molecule biosensors Designer molecules

1.2. Near Field Thermal Radiation

Radiative heat transfer is one of the fundamental modes of heat transfer that plays an indispensable role in everyday life such as medical treatments, thermal insulations, energy conversion systems, nanomanufacturing and numerous research areas. Radiant energy exchange also varies from macro- to nano-scales with respect to the governing physics considered. This exchange can be mainly categorized as far- and near-field radiation based on the dominant wavelength, λ_{th}, of emission and the length scale of the geometry that the radiative energy exchange is considered [6]. For the bodies separated by a distance, d, being larger than the dominant wavelength, which is predicted from Wien's displacement law, classical Stefan-Boltzmann law can explain the radiative transfer. Wien's law and Stefan-Boltzmann law link the radiative transfer only to propagating modes of the electromagnetic (EM) fields that arise from the charge density fluctuations at finite temperature of the material. These fluctuations develop out of the chaotic motion of free electrons for metals, and they are limited by electronic mean free path, l_e. On the other hand, optical phonons of the ionic crystals induce these fluctuations limited by a lattice constant. If the separation distance is much smaller than the dominant wavelength of the emission, then the propagating mode of electromagnetic waves on surface will lose its dominance and radiative heat transfer between the bodies exceeds the value predicted by classical theory. In this case, proximity, or near-field effects become dominant for the radiation as the larger wave vector, from $2\pi/\lambda_{th}$ to $2\pi/l_e$, results in localized fields decaying exponentially from the surface, which is known as *surface evanescent waves.* If the emitting body is far from the receiving body, evanescent wave cannot mediate the heat transfer since the time-average of Poynting vector $\langle\vec{S}\rangle$ (i.e. radiative heat flux) normal to the surface is zero. If the bodies become closer, then the receiver *'feels'* the field effect and energy flow can occur at such distances. This phenomenon is known as *radiation tunneling* or *near-field coupling* [7].

1.3. Applications

The metallic nanoparticles have unique properties due to their high surface area, surface plasmon resonance response, and quantum confinement of electron movement which can be utilized in many areas. Noble metals such as gold, silver, and copper, have always been the center of interest due to their unique plasmonic response. At nanoscales, after a critical length scale (i.e. Fermi wavelength, λ_f) is exceeded, oscillating charges on the surface of the nanoparticle are forced to resonate with the incident light frequency generating evanescent waves localized in the near-field. If an object is placed within few hundred nanometers, they engage in a near-field coupling resulting in EM field enhancement and increased absorption with localized heating. This phenomenon takes place where the resonance occurs at the highest level of field intensity and it is called as the localized surface plasmon resonance (LSPR) [8, 9].

There are numerous applications based on the optical response of the nanoparticles with their spectral absorption, scattering and extinction behavior at the LSPR wavelengths, including sensing with surface enhanced Raman spectroscopy (SERS) [10], near field optical microscopy (SNOM) [11], tip-enhanced Raman spectroscopy (TERS) [12], cancer therapies with photothermal ablation and targeted drug delivery [13, 14], imaging systems with contrast agents [15], and nano-manufacturing technologies [16, 17]. Selective and localized heating of nanoparticles are essential in both biomedical and nano-scale manufacturing applications. When the plasmonic particles are illuminated by an EM wave at a wavelength close to their LSPR wavelength, particles are heated. Then, they can be used not only to ablate the tumor tissue for photothermal therapies but also to tailor the surface by creating a deposit of molten nanoparticles for nano-manufacturing [13, 17, 18]. The plasmonic response of the nanoparticles are also used to enhance the sensitivity of the sensors for clinical, and environmental purposes. As the wide interest is on the applications of nanoparticles, quantization, and characterization of these materials in terms of their size and shape are important subjects as well. The well-known tools for the characterizations are transmission electron microscopy (TEM), scanning electron microscopy (SEM), X-ray photoelectron spectroscopy (XPS), and atomic force microscopy (AFM) [19].

Metallic nanoparticles (NPs) have also strong absorption behavior over entire visible light spectrum due to their relatively large absorptive index (k). An increase in metal particle size generally results in a red shift and damping of dipole resonance wavelength due to reduced restoring force and decreased effects of interband transitions. It should be noted that plasmon responses of the metal NPs are strongly dependent on the surrounding or neighboring medium. Hence, biological detection through optical sensing of refractive index of the surrounding medium can effectively be performed using metal particles and their hybrid structures [8,20,21]. Both experimental and numerical studies have shown that metal-metal core-shell nanoparticles can have hybridized plasmon modes, which are due to bimetallic structure inducing surface and cavity plasmons depending on the core/shell ratio [21–26]. Hybrid plasmon modes of the metal-metal core-shell nanoparticles can also be exploited for field enhancement, localized heating, optical detection, and controlled shell formation due to their wide tunability and multi-peak response of localized surface plasmon resonance (LSPR) [15, 26, 27]. LSPR response of metal-metal core-shell nanoparticles may not be well interpreted from their core/shell ratio unlike the case with dielectric-metal pairs [28]. Since the plasmon peak positions depend on the LSPR wavelengths of both core and shell plasmonic materials, the positions, and their amplitudes of the LSPR can be affected by both composition ratio and shielding of the metallic shell [21, 25, 28].

1.3.1. Nanopatterning and Local Heating

The concept of metals supporting surface plasmon polariton modes in the near-field regime introduced the possibility of utilizing surface plasmon resonance of these materials in nanopatterning applications. If a material supporting surface waves undergoes a surface polariton excitation, the absorptance of the material suddenly increases as the reflectance drops [29]. Since the excitation of surface polaritons are dependent both on material and length scale of the system, manipulation of SPP modes and tuning the localized surface plasmonic resonance (LSPR) of noble metallic nanoparticles render lots of possibilities in nanoscale manufacturing [17, 30]. Selective excitation of nanoparticles, such as gold, copper, and silver, can occur in the near-UV and visible region of the light spectrum unlike the polar crystals being excited in the IR region [7,30]. Moreover, size and shape differences in aggregate nanoparticles can be used in selective heating, melting, and/or fusing by utilizing their SPR frequency differences. The analytical models explaining near-field coupling have been done for simple geometries such as plane interfaces and multilayered structures [7]. For spherical objects EM field interaction can be explained by Lorenz-Mie theory with the dipole approximation of small particles. Understanding the SPR behavior of metallic nanoparticles is crucial when the particles are nearby. In that sense, the polarization direction and spacing of the particles affect the SPR frequency. This fact is explained in [31] as the particle is affected by additional forces that either decrease or increase the resonance frequency according to the particle alignment with respect to direction of the field. For metallic nanoparticles, surface charges create repulsive forces when the particle is excited. If the field is parallel to the particle alignment as shown in Figure 1.1(c), repulsive forces of the surface charges become weak and attractive forces develop between the particles. Therefore, parallel alignment of particles results in lower resonance frequency, red-shifting. Contrarily, as shown in Figure 1.1(c), when the field is normal to the particle alignment, both particles enhance the repulsion that increase the resonance frequency, i.e. blue-shifting. More- over, resonance frequency does not change anymore when the center-to-center spacing of gold nanoparticles, which are aligned either parallel or normal to the polarization direction, is increased more than two times of the diameter of the nanoparticles. The spacing, shape, and material effects on resonance frequency of the nanoparticles are needed to be considered and studied widely

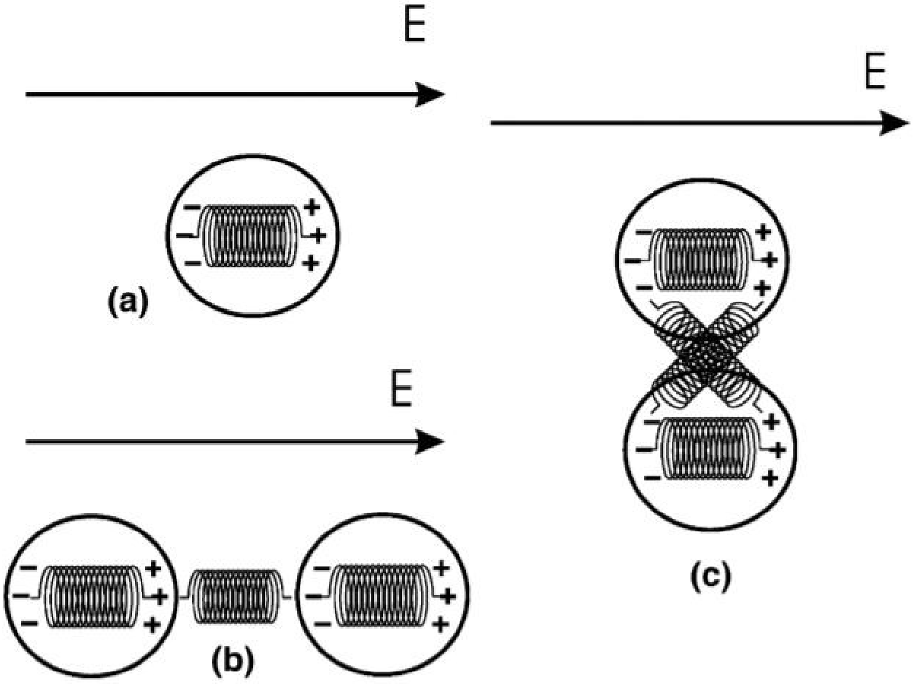

Figure 1.1. Sketch of EM field interaction between (a) single particle, and pair of particles aligned (b) parallel, and (c) perpendicular with respect to the field [31].

to fully understand their response in the near-field regime if one wants to utilize them for nanomanufacturing.

Hawes *et al.* [30] numerically analyzed the scattering and absorption profiles of nanosized particles on different substrates to study the spatial effects of particle arrangements and excitation behavior of these particles in terms of their resonance frequency and system configurations. Their computational study showed that 10 nm in diameter of gold and silver nanoparticles with different spacings on different surfaces such as glass, silver, and gold films have different absorption profiles under the illumination by total internal reflection (TIR). According to their results, gold and silver nanoparticles gain less absorption when they illuminated on silver film than on the glass one. Moreover, decreasing the separation of gold and silver NPs on a glass substrate resulted in red-shifting and blue-shifting of resonance frequencies of gold and silver nanoparticles, respectively. This can be a powerful design tool to selectively heat the desired particles at their specific resonance wavelength. Following with the study of Hawes *et al.*, several studies showed that local heating of gold nanoparticles on a dielectric glass substrate can be implemented with the exploitation of surface plasmon resonance and near-field coupling of an atomic force microscope (AFM) probe at various nanoparticle separations, sizes, and probe-particle distances [17,32]. In this configuration, transverse magnetic (TM) wave illumination is preferred for enhanced absorption efficiency due to additional perpendicular component of the evanescent wave from TM [9,17,32,33]. A numerical study for an array of gold nanoparticles on a glass substrate under an AFM tip shows that redshift of the plasmon resonance wavelength is observed with enhanced absorption when the separation distance of the particles was increased to an optimal value [32]. The study of complex nanostructures on a BK7 substrate also showed that gold array with combinations of cubical and spherical geometries can also provide a redshift of the plasmon resonance wavelength and greater absorption efficiency [34].

Moreover, absorption enhancement and LSPR wavelength changes are observed for the core-shell structures with dielectric and metal pairs, which can be utilized in optical tuning and localized heating applications [28, 33]. It is shown that near-field coupling can enhance the absorption of gold nanoparticles placed on a dielectric substrate under a dielectric tip due to perturbation on the dielectric environment [9]. Moreover, comparison of incident wave polarizations for the absorption enhancement of gold nanoparticles showed that TM-wave illumination creates greater field enhancement. This is attributed to the fact that TE polarization creates decaying evanescent wave transverse to tip-NP axis, while the TM one has additional partial polarization along the tip-NP axisleading to more perturbation on the dielectric environment of the nanoparticle [9, 33]. Nevertheless, the effect of dielectric tip on the absorption of metal nanoparticles should not be generalized. Comparison of Ag and Au nanoparticles showed that Si tip damps the absorption of AgNP in contrast with the case of AuNP. The spectral absorption behavior of AgNP with Si tip results in increased damping factor dominating over the driving force. However, an increase in driving force domination results in absorption enhancement in the AuNP case [35].

1.4. Core-Shell Nanoparticles

As discussed in Section 1.3.1, the spectral position of LSPR of the nanoparticles depends on their size, shape, and surrounding medium. In some applications, where optimum field enhancement is aimed, tuning the LSPR position may not be guaranteed with single component nanoparticles due to impurities, and/or difficulties in creating the specified shape and size. Hence, the idea of using alloys as well as different core and shell materials in the nanoparticle compositions draw great interest [27]. Other studies also report that hybrid structures of metal nanoparticles can have distinct optical responses than the bare metal nanoparticles [36]. Especially for selective heating applications, dielectric core with large refractive index can be used to alter the plasmonic response of the metallic particles [14, 18]. Other numerical and experimental studies also show that silica core with gold shell nanostructures can increase absorption with uniform heating [33] and LSPR response in a range of visible (vis) to near-infrared (NIR) region of the spectrum [37]. Aim of using core-shell nanoparticle is to optimize the plasmon response of the particles with greater field enhancement. Possible nanoparticle combinations can be considered as metal-metal [27], metal- dielectric [38, 39], and dielectric-metal [39, 40] core-shell structures.

1.4.1. Metal/Dielectric Core-Shell Pairs

One of the first experimental studies on core-shell nanoparticles was carried out by Zhou *et al.* [36] with dielectric core-metal shell NPs. It was observed that shifting of the plasmon resonance to longer wavelengths was possible varying gold shell thickness. Dielectric core-metal shell NPs are studied in optical contrast agents, targeted heat delivery, and photothermal ablation with their tunable LSPR wavelengths. The most advantageous optical response of the dielectric-metal core-shell nanoparticles is the redshift of plasmon peaks when the metal shell thickness is decreased. Therefore, dielectric-metal core-shell nanoparticles are good candidates for in vivo diagnosis of cancer tissues due to their optimum optical transmission through tissue within NIR regime [37, 41]. Oldenburg *et al.* [42] also showed that the optical resonance of silica core and gold shell NPs can be easily tuned from visible to mid-infrared wavelengths by increasing the core/shell ratio. Through numerical and experimental studies, similar conclusions have been reached with the dielectric core and noble metal shell nanoparticles [42, 43]. Dielectric-metal core-shell nanoparticles are also sensitive to the changes in the surrounding medium, where an increase of refractive index of the medium results in both redshift and increased intensity, facilitating their use in refractive index sensing applications [41, 44]. Dielectric coating of metal core provides chemical and physical stability of both the plasmonic core and the environment, while it can also prevent agglomeration of the particles [38, 39]. Metal-dielectric NPs can be used in photothermal therapy, biosensors, and solar cells with their enhanced plasmon resonance due to stronger Coulombic interactions between polarization charges of the dielectric shell and the free electrons in the plasmonic core as a result of the dielectric shell having larger refractive index than the core. This phenomenon has also been studied experimentally with gold core-silica shell for photothermal ablation techniques [45]. The numerical comparison of dielectric-metal and metal-dielectric core-shell nanoparticles has shown that gold core with silica shell has higher scattering/absorption ratio in NIR region, which is preferred in solar cell applications [39]. Moreover, studies have shown that contrary to dielectric-metal core-shell NPs, metal-dielectric ones have redshifted plasmon as the shell thickness increases while their absorption efficiency responses mostly depend on the volume of the NP and shielding effect of the dielectric shell [39].

1.4.2. Bimetallic Core-Shell Pairs

Zhang *et al.* [26] showed in their theoretical study that bimetallic structure of core-shell NPs can have two different surface plasmon resonance (SPR) modes that leads to two peaks with ordinary and extraordinary modes. They also showed that different metal-metal arrangements can support both red-shift and blue-shift in the short (extraordinary mode) and long (ordinary mode) wavelengths as the core/shell size is varied. Since the field localizations occur both at the core-shell interface and at the outer shell surface, the size configurations of metal-metal structures can be utilized for optical detection and bio-sensing. Navas and Soni [46] experimentally and theoretically showed that metal NPs can have enhanced absorption in water compared to those in air. Moreover, they found that LSPR wavelengths red-shift as the excitation of surface electrons needs smaller energy in medium with larger refractive index. Comparisons of plasmon response of the metal NPs showed that Ag and Au NPs are good candidates as they have higher refractive index sensitivity, which can be utilized in bio-sensing applications.

1.5. Objective

Although there are numerous numerical studies based on NPs and their LSPR response, most of them were analyzed within a free space without surface interactions or in an aggregate form. As stated earlier, numerical study of silica core-gold shell NP being placed on a BK7 substrate showed that enhanced absorption efficiency and a redshift of the plasmon response can be achieved for selective heating and nanomanufacturing purposes [33]. There are, however, limited number of studies on material comparisons that will guide the experimentalists to the optimum configurations for the enhanced effects. The objective of this study is to focus on the spectral absorption profiles of core-shell nanoparticles with various core-shell material and size configurations accompanied with surface interactions.

Chapter 3 is presented in this study as a follow-up investigation of [33] with single core-shell nanoparticle placed on a semi-infinite BK7 glass substrate being illuminated by an EM light from bottom with total internal reflection. The spectral absorption behavior of core-shell nanoparticle is numerically studied with selected metal-dielectric, and dielectric-metal pairs for core and shell materials, respectively. In this study, volumetric filling ratio of core material to the whole nanoparticle will be utilized to be able to set standards for size configurations. This ratio will be used for the comparisons of metal and dielectric pairs with their LSPR response and absorption efficiency. This problem and its results are also published in [28].

Moreover, in bio-sensing applications the NP is usually placed at an interface, where it interacts with light and the surrounding media. Therefore, there is a need for investigation of optical absorption behavior under varying core/shell size at an interface so that these hybrid structures can be utilized in bio-sensing and material detection. Hence, the second part of the study, Chapter 4 focuses on Ag and Au bimetallic core-shell nanoparticles placed over a dielectric surface. Moreover, the absorption suppression of metal nanoparticles under a dielectric tip as reported in [35, 47] are also applied to core-shell structures, with Si and GaP tips being analyzed considering their spectral refractive index, especially where these materials behave as a dielectric for the wavelengths greater than 490 nm [28, 33, 48]. Since the LSPR wavelengths of Ag and Au NPs in 50 nm diameter are around 365 nm and 515 nm [28], respectively; the damping of absorption in AgNP may not be effectively seen for longer wavelengths. Therefore, there is a need for spectral absorption analysis in a wider range of spectrum including the LSPR wavelength of both Ag and Au nanoparticles.

For bimetallic NP case of the study in Chapter 4, both Ag core-Au shell (Ag@Au) and Au core-Ag shell (Au@Ag) metallic NPs are studied with their LSPR response and absorption efficiency profiles. Comparisons are done based on the plasmon responses with respect to varying size configurations and surrounding mediums. The medium refractive indices are chosen between 1 and 1.5 so that it can be applied to water, hemoglobin/plasma [41,49,50], and to other possible biological materials for bio-sensing applications. Further analysis will be conducted on selected core-shell pairs with greatest absorption scenario to compare the effect of near-field coupling of AFM tip on the spectral absorption behavior.

In this comparison study, numerical simulations are performed with DDA-SI-v for absorption efficiency calculations of core-shell NPs with at most 50 nm in diameter. This extensive study is expected to shed light on the material selections with their effects on the absorption efficiencies that can be useful for localized heating applications, bio-sensing, and nano-scale manufacturing.

2. THEORY AND NUMERICAL METHODS

2.1. Theory

2.1.1. Fluctuational Electrodynamics and Fluctuation-Dissipation Theorem

Through the solutions of Maxwell equations, classical electromagnetic wave theory can explain the well-known radiative transfer equations in terms of reflection, refraction, and diffraction. However, for the near-field calculations, the effect of oscillating dipoles to the thermal emission in the forms of propagating and evanescent wave is not included in the classical approach. The first theoretical attempt to solve this problem was done by Rytov in 1953 following with Polder and Van Hove's modeling for thermal emission [6,51]. At a macroscopic level, fluctuational electrodynamics (FE) transforms the Maxwell equations from time-domain to frequency-domain and focuses on the thermal fluctuations of charge and current volume densities, ρ and $\vec{J}$ respectively, that result in EM field fluctuations in local thermodynamic equilibrium [6,7]. In FE, fluctuations of the field are ascribed to random external sources defined with their location and frequency, $\vec{J^r}$ *(r,ω)*. Randomness of these sources comes out with a need for the solution of stochastic Maxwell equations, which can be done with a method of dyadic Green's function (DGF), and method of potentials [7,51]. The electric and magnetic fields obtained with those methods are;

$$\vec{E}(\vec{r},\omega) = i\omega\mu_o \int_V \bar{\bar{G}}^E(\vec{r},\vec{r}\,',\omega)\overrightarrow{J^r}(\vec{r}\,',\omega)dV' \tag{2.1}$$

$$\vec{H}(\vec{r},\omega) = i\omega\mu_o \int_V \bar{\bar{G}}^H(\vec{r},\vec{r}\,',\omega)\overrightarrow{J^r}(\vec{r}\,',\omega)dV' \tag{2.2}$$

where $\bar{\bar{G}}^E$ and $\bar{\bar{G}}^H$ are dyadic Green's function of electric (E) and magnetic (H) fields, respectively. DGFs relate the field observed at $\vec{r}$ with frequency ω resulting from the source at $\vec{r}\,'$. DGFs of electric and magnetic fields are represented as;

$$\bar{\bar{G}}^{E}(\vec{r},\vec{r}\,',\omega) = \left[\bar{\bar{I}} + \frac{1}{k^2}\nabla\nabla\right] G_o(\vec{r},\vec{r}\,',\omega) \tag{2.3}$$

$$\bar{\bar{G}}^{H}(\vec{r},\vec{r}\,',\omega) = \nabla \times \bar{\bar{G}}^{E}(\vec{r},\vec{r}\,',\omega) \tag{2.4}$$

where $\bar{\bar{I}}$ is 3×3 identity matrix, $k = (\omega^2 \varepsilon \mu_o)^{1/2}$ is magnitude of the wave vector, and G_o is the scalar Green's function. By using Green's function, radiative heat flux can be obtained from the cross product of E and H fields as follows;

$$\begin{aligned} \langle \vec{S}(\vec{r},\omega) \rangle = 2\Re\Big(i\omega\mu_o \int_V dV' \int_V dV'' \Big[\hat{x}(G^{E}_{yn}G^{H*}_{zj} - G^{E}_{zn}G^{H*}_{yj}) + \\ \hat{y}(G^{E}_{zn}G^{H*}_{xj} - G^{E}_{xn}G^{H*}_{zj}) + \hat{z}(G^{E}_{xn}G^{H*}_{yj} - G^{E}_{yn}G^{H*}_{xj}) \Big] SCF \Big) \end{aligned} \tag{2.5}$$

$$SCF = \langle \vec{J}^{\,r}_{n}(\vec{r}\,',\omega) \vec{J}^{\,r*}_{j}(\vec{r}\,'',\omega) \rangle \tag{2.6}$$

where SCF is the spatial correlation function of the random sources as an unknown that can be solved with fluctuation-dissipation theorem (FDT) with certain limitations. Although some of the FDT restrictions can be discarded or relaxed, the main assumptions for the FDT are the isotropic, nonmagnetic media defined with frequency dependent dielectric function, $\varepsilon(\omega)$, within local thermodynamic equilibrium [6,51,52]. In thermal radiation, FDT correlates the local temperature and $\vec{J}^{r}$ to obtain a reasonable heat flux expression, which can be shown as;

$$\langle \vec{S}(\vec{r},\omega) \rangle = \frac{2k_o^2 \Theta(\omega,T)}{\pi} \Re\Big(i\varepsilon''(\omega) \int_V dV' G^{E}_{m\alpha} G^{H*}_{m\alpha} \Big) \tag{2.7}$$

$$\Theta(\omega,T) = \frac{\hbar\omega}{\pi^2 c_o^3} \big[\exp(\frac{\hbar\omega}{k_b T}) - 1 \big] \tag{2.8}$$

where k_o is the magnitude of the wave vector in vacuum, and $\Theta(\omega, T)$ is the average energy of an oscillator decreasing exponentially, which is found by Max Planck, in 1990, with the discovery of energy quantization. Moreover, mean energy of a Planck oscillator induces the well-known Stefan-Boltzmann law at large wavelengths, which falls in the far-field regime [53].

2.2. Electromagnetic Local Density of States (LDOS)

Local density of EM states is a generalized local form of the density of states (DOS) that is used for calculating the macroscopic quantities such as energy density in this survey's topic. In [54], LDOS at any point is expressed as the sum of location dependent and independent terms. Joulain *et al.* [55] described the LDOS as the multiplier of a mean energy of a Planck oscillator which yields the local density of spectral electromagnetic energy such as;

$$u(\vec{r}, \omega, T) = \rho(\vec{r}, \omega)\Theta(\omega, T) \equiv \left[\varepsilon_0 \langle |\vec{E}(\vec{r}, \omega)|^2 \rangle + \mu_0 \langle |\vec{H}(\vec{r}, \omega)|^2 \rangle\right] \tag{2.9}$$

where $\rho(\vec{r}, \omega)$ is the function of local density of states including the electric and magnetic contributions [54–56]. This definition is proved to be useful, when density of states becomes prominent for the inside of the material. Narayanaswamy *et al.* extended the definition of LDOS for absorbing media by including spatial dispersion, and by splitting the function into homogeneous, and inhomogeneous parts [54]. Joulain *et al.* used the analogy between Scanning Tunneling Microscope (STM) measuring the electronic LDOS in order to relate the signals of Scanning Near-Field Optical Microscope (SNOM) to the electromagnetic LDOS. They showed that resonance frequency of the material in the near-field experiments yields and electric contribution of LDOS [55]. Moreover, it is shown that when the length scale is reduced, resonance frequency of the real materials, i.e. metals and dielectrics whose dielectric function $\varepsilon(\omega)$ is described by a free-electron Drude model for near-UV and IR spectrum, resulted in large density of electromagnetic states. Hence, heat transfer enhancement can be achieved by dipole resonance in near-field regime. As shown in [6,55], transverse magnetic (TM) polarized surface waves in materials increase the energy transfer more than the transverse electric (TE) polarized ones in the near-field regime. Until now, the relation between density of states and effect of surface waves in near-field radiation have been discussed. The next discussion will be based on the surface wave supporting materials and their usage in local heating for nanostructures and energy conversion devices.

2.2.1. Surface Phonon-Polariton and Surface Plasmon-Polariton

As discussed above, chaotic motion of oscillating charges in metal and optical phonons in ionic crystals results in exponentially decaying fields that are called *evanescent waves*. If the separation of the surfaces, d, approaches to zero, evanescent waves can decay in each surface material. Surface plasmon-polariton (SPP) results from the longitudinal out of phase oscillations of electrons in metals whereas surface phonon-polariton (SPhP) occurs due to transverse oscillations of optical phonons in ionic crystals. Dispersion relations for both TE and TM polarized waves play an important role in order to understand the effect of surface waves in near-field radiation. For instance, when the poles of Fresnel coefficients for TE and TM polarization of materials are considered for 2D geometry, it is shown that surface polariton can exist naturally for TE polarized wave. On the other hand, TM polarized wave can only result in surface

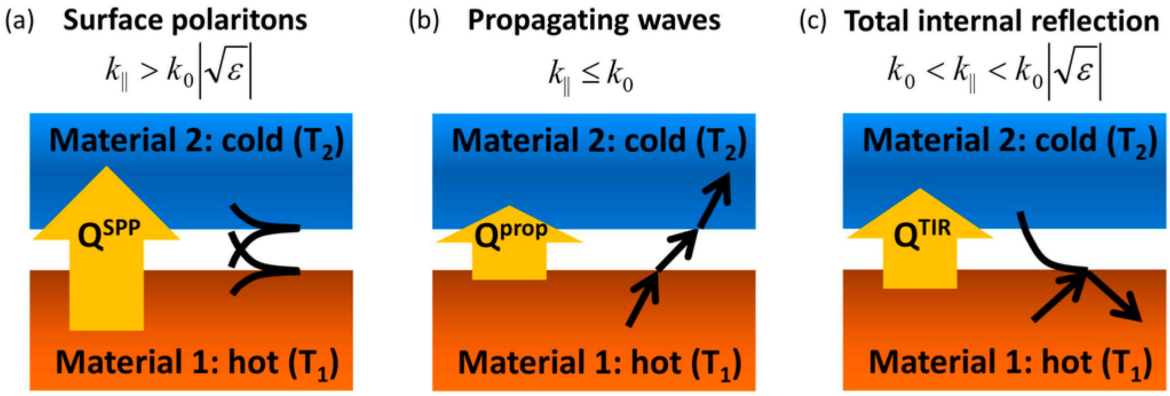

Figure 2.1. Illustration of near-field radiative heat exchange between plates due to (a) coupled surface polariton modes, (b) propagating waves, (c) evanescent fields by total internal reflection (TIR) [57].

waves if the dielectric function of the medium, $\varepsilon_m(\omega)$, has negative real part [6]. As shown in Figure 2.1, there are three types of waves that can occur between emitting and absorbing media.

Although SPP modes of waves in noble metals such as gold (Au) have relatively small mean energy of Planck oscillator as compared to SPhP modes due to Drude model dielectric function, plasmon frequency of these noble metals in tunable by varying the charge carrier densities. Moreover, metals have wide frequency range of negative permittivity, which can be utilized with their resultant SPP modes. By changing the surface properties of the material, near-field radiative energy exchange can be enhanced [52, 57]. Boriskina *et al.* showed that there can be various film-substrate combination of phase change materials to tailor the spectral behavior of the heat flux between media.They exemplified some of the tunable materials as vanadium dioxide (VO_2), indium tin oxide (ITO), although they correspond to lower enhancement than the polar dielectrics. Lastly, plasmonic film usage in substrates is proposed as a powerful tool to enhance energy transfer in some applications such as thermo-photovoltaic (TPV) energy conversion devices [57].

2.3. Numerical Methods

Electromagnetic wave interactions with NPs and their resulting optical response can be studied numerically with the computational electromagnetic methods (CEM) through the solutions of Maxwell's equations. The discrete dipole approximation (DDA) is one of the semi-analytical CEM for which the nanoparticle is represented by a number of dipoles. Since the general formulation of DDA, developed by Purcell and Pennypacker [58], many open source DDA methods have been implemented such as DDSCAT written in FORTRAN [59, 60], and ADDA written in C++ [61]. Another open source MATLAB$^{\text{TM}}$ toolbox, DDA with surface interactions (DDA-SI), was developed by Loke and Mengüç [62] for the objects placed on a dielectric surface. The method was extended for configurations, where nanostructures are placed over a dielectric substrate by considering the Sommerfeld integral formulation. The toolbox is validated against microwave analog experiments, and other discretization methods for

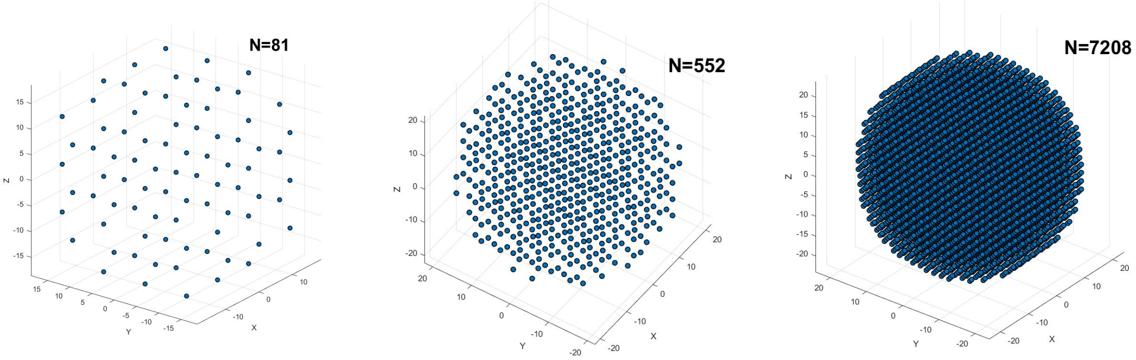

Figure 2.2. Spherical particle represented with N = 81, 552, 7208.

particles on a surface [63,64]. The toolbox was further improved for computational efficiency adopting a vector formulation in the vectorized version of DDA-SI (DDA-SI-v) by Talebi-Moghaddam et. al [33], where verification of the method is also provided. Recently, an updated version (DDA-SI-z) is developed by Rostampour-Fathi *et al.* for improved solver performance [34].

2.3.1. DDA-SI and DDA-SI-v

Discrete dipole approximation with surface interaction (DDA-SI) and vectorized version of it (DDA-SI-v) are useful semi-analytical methods for the analysis of near- and far-field scattering of objects placed on and near the substrate. The calculations are done through the discretization of dipoles with assigned dipole coordinates, and incident electric field at each dipole. In this section, the basic calculations for near-field interaction of the spherical nanoparticle and surface evanescent wave created by the total internal reflection (TIR) will be outlined.

Representing the dipoles at an accurate level is the first step of the implementation. The point dipoles of the object are created with the coordinates, $\vec{r}_j = (x_j, y_j, z_j)$, where *j=1,...,N*. An example of the spherical structure approximated with different number of dipoles are depicted in Figures 2.2, where the equivalent spherical volume is defined with the cubic volume occupied by N-dipole with lattice spacing, *d*, as defined in Equation 2.10.

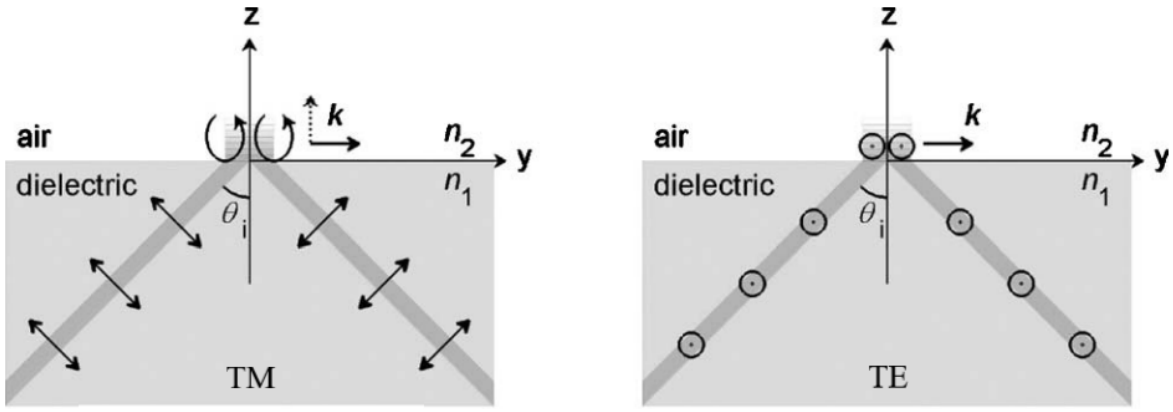

Figure 2.3. A schematic view of incident TM (a), and TE (b) polarized waves being incident below the dielectric substrate with total internal reflection that creates surface evanescent waves decaying in z-direction [16].

$$Nd^3 = \frac{4}{3}\pi a^3 \tag{2.10}$$

where a is defined as effective radius of the spherical particle. It should be noted that randomly generated dipole coordinates are nondimensional values that need to be converted into nanometer scale which is done by scaling lattice parameter with the incident wavelength λ as shown in Equation 2.11.

$$d^* = \frac{d}{\lambda} \tag{2.11}$$

where d^* is then used to calculate the scaled geometry of the sphere, which are $\vec{r}_{sph} = \vec{r}_j d^*$ and $a_{sph} = a\lambda^{-1}$.

After setting the geometry of the particle, surface decaying wave is to be formulated by defining the incident EM wave polarization characteristics and angle of incidence, θ_i, of the light illuminated from below the substrate. For the simulations the polarization directions are set as reference to the scheme shown in Figure 2.3. If the incident wave angle, θ_i, is beyond the critical angle, θ_c, calculated with Snell's law of refraction in Equation 2.12, then the resultant wave vector and polarization direction vectors can be calculated by the Equations 2.3.1.

$$n_1 cos(\theta_1) = n_2 cos(\theta_2) \quad \text{and} \quad \theta_c = arcsin(n_2/n_1) \tag{2.12}$$

$$\begin{aligned} k_e &= [\ 0 \quad 2\pi n_1 sin(\theta_i) \quad i2\pi\sqrt{n_1 sin(\theta_i) - n_2^2}\ ] \\ \hat{e_p} &= [\ 0 \quad icos(\theta_r) \quad sin(\theta_r)\ ] \qquad \text{and} \qquad \hat{e_s} = [\ 1 \quad 0 \quad 0\ ] \end{aligned} \tag{2.13}$$

where n_1 and n_2 are refractive indices of the dielectric surface and upper medium, respectively. The angle of the refracted wave in the upper medium is shown as θ_r in Equation 2.3.1, which is found from the Snell's law in Equation 2.12. In Equation 2.3.1, k_e is defined as surface evanescent wave vector. Following $\hat{e_p}$ and $\hat{e_s}$ unit vectors are found as the polarization directions of TM and TE wave vectors, respectively. These vectors are used with the Fresnel formula to find the transmitted fields in the upper medium, which are E_p and E_s. Then, the final resultant evanescent wave,E_e above the substrate is shown as;

$$\vec{E_e} = \vec{E_p} + \vec{E_s} \tag{2.14}$$

Assume that the point dipole represented at r_j undergoes a field interaction from other dipoles at r_j. In the presence of a surface, the dipole-dipole interaction matrix, A_{jk}, formulation should be extended with the Sommerfeld integral tensor to evaluate the Green's function for the field created from reflected-dipole interaction. After constructing the interaction matrix, the linear system can be solved to find dipole moment,P after which extinction, absorption, and scattering cross-sections and their efficiency can be evaluated [62]. The detailed formulation can be found in [16,62]. One example is given for the absorption efficiency is given in Equation 2.15, Q_{abs}, which is the ratio of absorption cross-section, C_{abs}, to the cross-sectional area of sphere with radius a_{sph};

$$Q_{abs} = \frac{C_{abs}}{\pi a_{sph}^2} \tag{2.15}$$

3. METALLIC/DIELECTRIC CORE-SHELL NANOPARTICLES ON A DIELECTRIC SUBSTRATE

3.1. Problem Statement

The system consists of single core-shell NP, which is placed on a semi-infinite BK7 glass substrate in vacuum ($n=1$). As shown in Figure 3.1, an incident wave is illuminated from below the dielectric surface with an incident angle greater than the critical angle for total internal reflection (TIR) that results in surface evanescent waves interacting with the nanoparticle. Unlike the study in [33], TE-polarized (rather than TM-polarized) EM wave illumination in the wavelength range from 300 nm to 800 nm is considered. Since we do not consider any vertically placed AFM probe, it is not

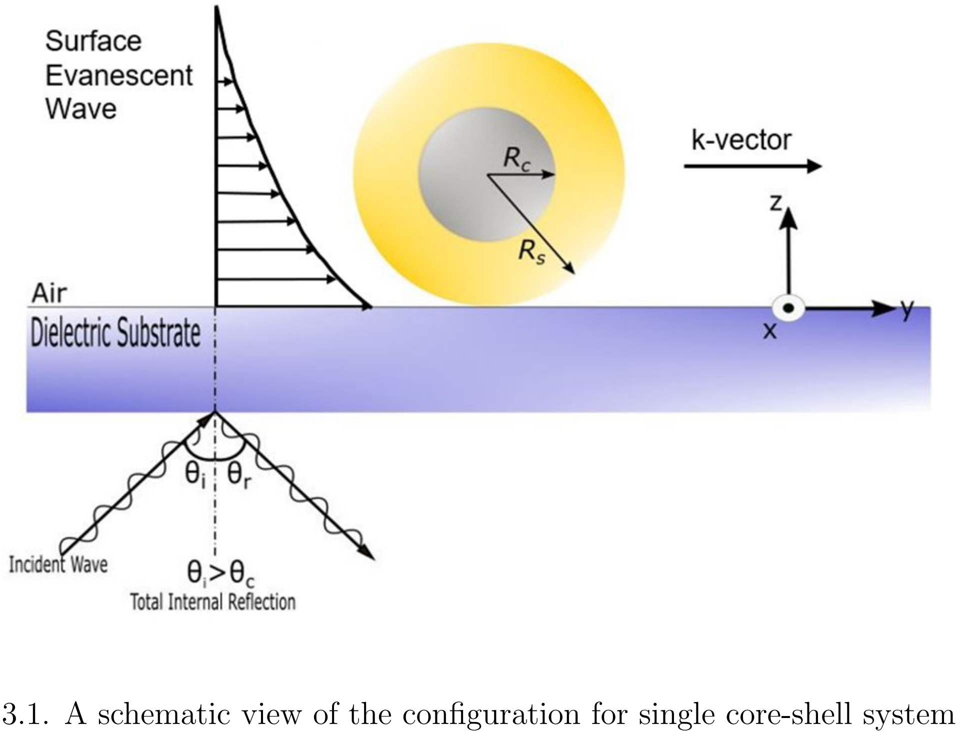

Figure 3.1. A schematic view of the configuration for single core-shell system being represented with core radius (R_c) and outer shell radius (R_s). TE-polarized wave is incident with an angle greater than the critical angle (θ_c) for TIR under the BK7 substrate that creates surface evanescent wave propagating and decaying in y- and z-directions, respectively.

Table 3.1. Core and shell sizes for FC and FNP cases of metallic-dielectric NPs with corresponding volumetric filling ratio (f_r) ranges.

NP Type	D_c **(nm)**	D_s **(nm)**	f_r **Range**
Fixed Core	20	22-50	0.751 – 0.064
(FC)	20	20	1
Fixed NP	15-45	50	0.027 – 0.729
(FNP)	50	50	1

required to use TM-polarized wave for field enhancement. Moreover, the simulations with TM-polarization have the same LSPR wavelength responses with slight decrease in absorption efficiency values. Therefore, the results presented for TE waves are also representative of TM polarization cases. In the analysis, dielectric-metallic and metallic-dielectric core-shell pairs are used. Materials chosen include gold (Au) and silver (Ag) for metals, and Gallium phosphide (GaP) and Silicon dioxide (SiO_2) for dielectrics. GaP is chosen due to its imaginary part of the refractive index, k, being nonzero for the wavelengths smaller than 490 nm. Unlike in the case of SiO_2, GaP has real part of the refractive index, n, greater than 3 that can create broadband near-field response and field confinement in sub-wavelength volumes [48, 65].

The absorption efficiency calculations are carried out for both varying shell thickness with fixed core diameter (D_c=20 nm) and varying core size with fixed NP diameter (D_s=50 nm). LSPR response of the particle is investigated through both fixed core (FC) and fixed nanoparticle (FNP) sizes. Size configurations are then used for the comparisons based on the volumetric filling ratio (f_r), which is defined as the ratio of the core volume with radius (R_c) to the nanoparticle volume defined based on shell radius (R_s), $f_r = (R_c/R_s)^3$. The summary of size configurations is tabulated in Table 3.1 with the corresponding f_r ranges.

For the simulations, refractive index of the core-shell nanoparticle materials are obtained from experimental measurements of [66] for Au and Ag while the data for GaP is used from [67]. For the optical properties of BK7 substrate and SiO_2, an empirical relation of refractive index and wavelength is used with Sellmeier equation.

3.2. Numerical Aspects

The DDA analysis through DDA-SI-v requires use of adequate number of dipoles (N) for an accurate representation of each nanoparticle. The optimum dipole number is identified as 1472, where the predicted absorption efficiency values converge. The lattice spacing (d) criterion is also considered especially for the metals that have large imaginary part of the refractive index at long wavelengths after 500 nm [60]. The lattice spacing of each material being used for the simulations show that the minimum lattice spacing is d_{min} = 5.57 nm for GaP with refractive index of 3.75+2.06i at 300 nm wavelength. The number of dipoles is selected larger than the one required for the minimum lattice spacing. Corresponding lattice spacings of the nanoparticles are then calculated based on nanoparticle volume (V) as, $d = (V/N)^3$. For the selected number of dipoles (N = 1472), the calculated lattice spacings are d_{min} = 1.06 nm and d_{max} = 3.54 nm for the limiting values of minimum core size (R_c = 7.5 nm) and maximum NP size (R_s = 25 nm), respectively. Hence, the nanoparticle representation with 1472 number of dipoles is enough for the lattice spacing criterion.

3.3. Results and Discussions

The absorption efficiency (Q_{abs}) is defined as the ratio ofabsorption cross-section to geometrical cross-section of the targeted NP. Accurate calculation of Q_{abs} requires adequate number of dipoles. Hence, the spectral absorption behaviour of specified core-shell nanoparticle being placed on BK7 glass substrate is studied with DDA-SI-v by using optimum number of dipoles (N = 1472) that is identified based on the converged maximum absorption efficiency values having less than 5% relative error with respect to the predicted values using N = 7208 dipoles. Moreover, DDA-SI-v simulations for a single NP in free space is compared with the analytical solution of Mie theory and the other DDA method, DDSCAT. The relative errors for the simulations are estimated as 6.3% and 4.1% when the maximum absorption efficiency values are compared against DDSCAT and the Mie theory, respectively. In both validation and verification studies of DDA-SI-v, the LSPR peak wavelengths are estimated with a relative error less than 5%.

After identifying the adequate number of dipoles, TE polarization of an EM wave is studied to identify the highest absorption efficiency value. The simulations are carried out based on the specified light spectrum range (300 - 800 nm). For each dielectric-metal and metal-dielectric core-shell NPs, there are two cases considered, one with fixed core (FC) and varying shell thickness, and one with fixed NP (FNP) size with varying core diameter. For both cases, a common metric is defined as volumetric filling ratio, f_r, as stated in Section 3.1. This dimensionless ratio is in the range of 0 - 1 (or equivalently, 0 - 100%) and it represents the core occupancy with respect to the overall NP volume. As the filling ratio increases in the FC case, the thickness of the shell material is decreased with decreasing NP size. Similarly, an increase in core size results in increasing filling ratio, while the NP size is fixed in the FNP case.

The following two sections are the results of dielectric-metal and metal-dielectric core-shell pairs and their spectral LSPR response with respect to size configurations. The scatter plots are designated to label the first maximum LSPR peak wavelengths with corresponding absorption efficiency values, Q_{abs}, as a function of f_r. The contour plots of absorption efficiencies with respect to size and wavelength are only shown for the FC case. The effect of the core size on the range of the LSPR wavelengths is also discussed in the sections in order to compare the range of LSPR tunability of the dielectric-metal pairs. Further analysis is carried out for selected core-shell NPs, which are SiO_2 core-Au shell and Au core-GaP shell, with their normalized field intensities for different core diameters. The effect of core size on the EM field localizations is shown for these selected core-shell NPs, while the overall NP diameter is kept at 50 nm.

3.3.1. Dielectric Core with Metal Shell

For this case, the results are depicted from Figure 3.2 to Figure 3.4. The absorption profiles of GaP core-Ag shell for both FC and FNP cases show a linear relation with respect to f_r of the GaP core. Figure 3.2(a) shows the maximum absorption efficiency values located near the LSPR wavelength of the bare Ag NP, which is around 365 nm. In this contour plot, apart from the first absorption maxima locations, the secondary peaks of LSPR response can be seen in cases with the outer shell diameter between 30 – 40 nm. In this range, hybrid modes with multipeak LSPR wavelengths are observed. Similar multipeak response is observed for the FNP case when the core diameter is between 25 – 35 nm. In this scenario, the primary LSPR wavelength supports EM field localizations both at the GaP core and the outer shell surface. Since the GaP has only the real part of the refractive index for the wavelengths longer than 490 nm, the secondary plasmonic mode causes field localizations at core-shell interface and Ag shell surface when the LSPR wavelength exceeds 490 nm.

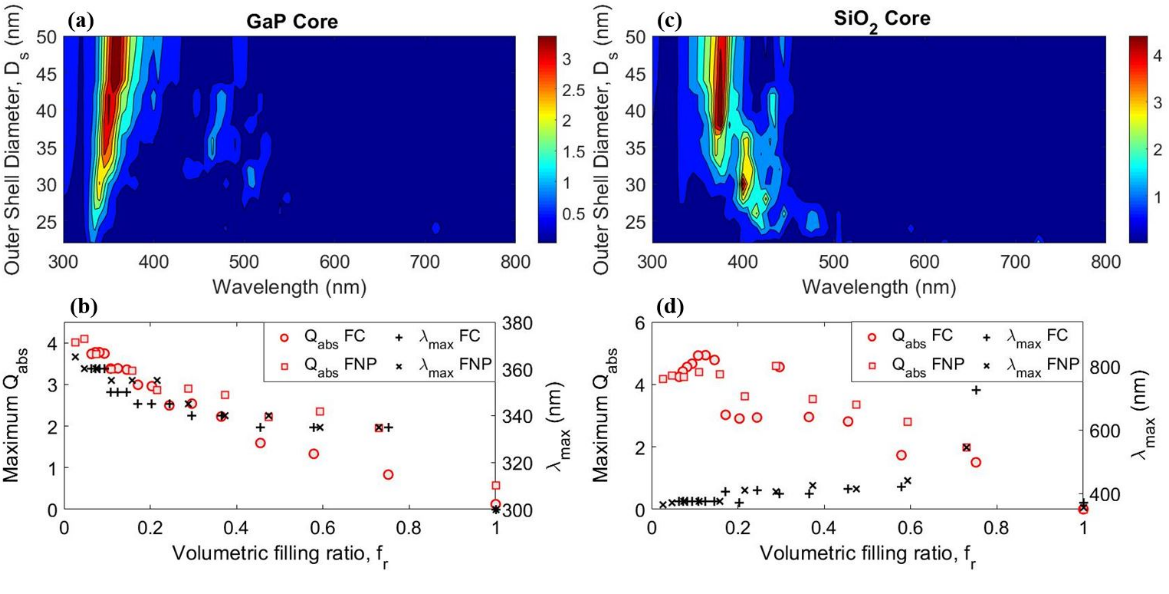

Figure 3.2. Ag shell with GaP (a-b) and SiO_2 (c-d) core: Contour plots of absorption efficiency as a function of wavelength for FC (a,c). Maximum Q_{abs} and LSPR wavelengths, λ_{max}, as function of f_r for FC and FNP (b,d).

As shown in Figure 3.2(b) for the fixed GaP core size, decreasing the f_r by increasing the Ag shell thickness results in a significant increase in the absorption efficiency from 0.83 to 3.77, while the corresponding LSPR wavelengths redshift from 335 nm to 360 nm. Similar response is observed in the FNP case with the increase of absorption efficiency from 1.95 to 4.09 and the total redshift from 335 nm to 365 nm when the GaP core size is decreased. It can be deduced that for both FC and FNP cases, increasing the f_r of the GaP core results in decreasing Q_{abs} with a blueshift of LSPR wavelength. When the f_r of the GaP core is increased, the field localization takes place on the outer surface of the Ag shell. Therefore, the NP with dielectric GaP core with relatively thinner absorbing shell material has smaller maximum absorption efficiency values.

The second case of the Ag shell is presented in Figures 3.2(c) and (d) with SiO_2 core material, which has larger redshift than the case with GaP core. In Figure 3.2(d), an increase of f_r of the SiO_2 core is shown with total redshifts by 355 nm and 180 nm for FC and FNP cases, respectively. Silica core having f_r greater than 30% results

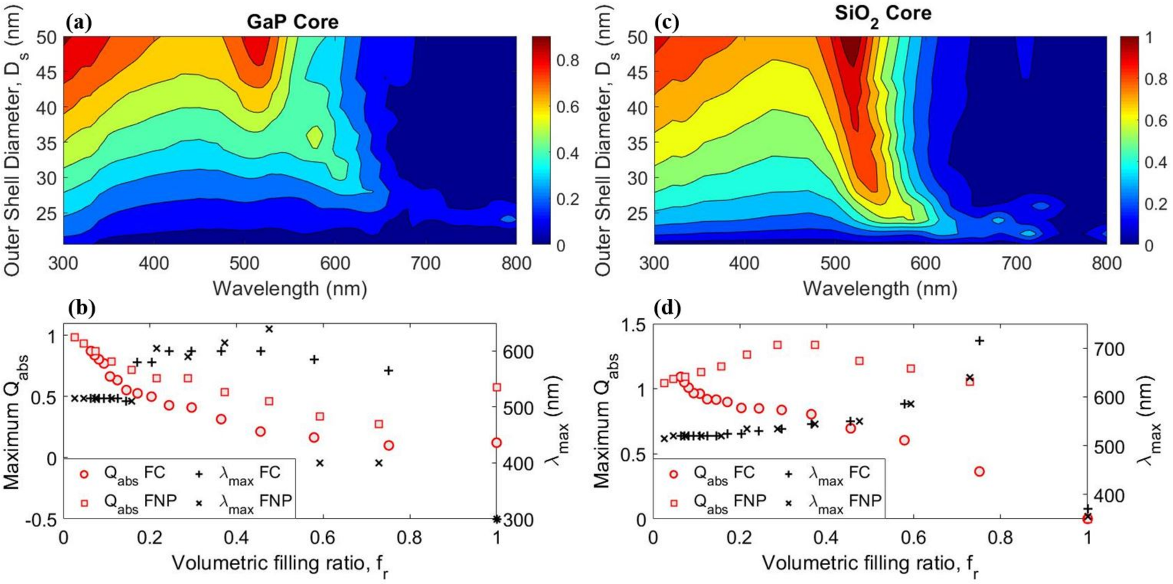

Figure 3.3. Au shell with GaP (a-b) and SiO_2 (c-d) core: Contour plots of absorption efficiency as a function of wavelength for FC (a,c). Maximum Q_{abs} and LSPR wavelengths, λ_{max}, as function of f_r for FC and FNP (b,d).

in decreasing absorption with a redshift in LSPR response. However, the absorption efficiencies and the LSPR wavelengths have no linear relation with the f_r. Moreover, comparison of the absorption efficiency values with the bare Ag NP with 50 nm diameter, which has maximum Q_{abs} value of 4.54 at 365 nm, showed that absorption enhancement of 8.81% is possible. The maximum absorption efficiency is found as 4.94 at 375 nm when the f_r of $SiO_2$2 core is 12.5% with 10 nm Ag shell as can be seen in Figure 3.2(d). For the NP diameter between 40 – 50 nm as shown in Figure 3.2(c), secondary peak regions can be observed because the shell thickness starts exceeding the skin depth (12 nm). Moreover, in these ranges, where the f_r of the dielectric core is below 20%, most of the absorption takes place within the shell material. In the Figures 3.2(b) and (d), both core-shell structures have LSPR wavelength patterns converging to 365 nm as the f_r of the dielectric core decreases, and Ag shell starts to dominate the plasmon response. Comparing Ag shell with dielectric core cases showed that wide tunability can be achieved with SiO_2 core, which redshifts the LSPR wavelength from the ultraviolet (UV) to the near-infrared (NIR) region of the light spectrum. However, wide tunability of LSPR response is not achieved when the core is GaP due to its non-zero imaginary part of refractive index, k, for the wavelengths smaller than 490 nm.

The absorption efficiency patterns for FC and FNP cases of the Au shell with GaP are presented in Figures 3.3(a,b), which show a wide range of tunability with small secondary peak regions. We observe that the LSPR wavelength values stay constant with decreasing absorption efficiency when the f_r of the GaP core increases up to 15%, for both FC and FNP cases. As shown in Figure 3.3(a), further increase of the f_r shows that first peak values of LSPR wavelength redshift to the 570 nm whilst the non-absorbing core reduces the absorption efficiency of the NP. There is a limiting f_r value for the core resulting in blueshift of the first LSPR wavelength when it is greater than 50%.

From the Figures 3.2(b) and 3.3(b), it can be observed that GaP core with the Au shell has large tunability with the range of 400 – 640 nm where the LSPR wavelength of the bare Au NP stays in between. On the contrary, the tunability of GaP core with Ag shell has narrower range of 335 – 365 nm that cannot go beyond the LSPR wavelength of the bare Ag NP (365 nm). Although GaP core with Au shell provides larger tunability of the LSPR wavelength, its absorption efficiency values are below the ones with the Ag shell.

The absorption profiles of SiO_2 core with Au and Ag shell cases shown in Figures 3.2(d) and 3.3(d) reveal that increasing f_r of the core after 0.2 results in a redshift of LSPR wavelength. Figure 3.3(d) depicts total redshift of LSPR wavelengths of 195 nm and 125 nm for FC and FNP cases, respectively. Due to the hybrid structure of the NP, secondary peaks similar to the case of GaP core-Au shell can be observed in Figure 3.3(c) for SiO_2 core-Au shell. Contrary to SiO_2 core-Ag shell case, maximum absorption efficiency values of SiO_2 core-Au shell has a smoother trend with respect to the f_r, as shown in Figure 3.3(d). For the FC case in Figure 3.3(d), decreasing the Au shell thickness decreases the absorption of the NP, while the LSPR wavelengths increase. Similar LSPR shift is observed in the FNP case with the maximum absorption efficiency values being enhanced to 1.34 at 535 nm wavelength when the f_r of the core is 30%.

As shown in Figures 3.4(a-c), the EM field localizations takes place between the core-shell interface and the outer surface of the metal shell. The case in Figure 3.4(b) shows the field intensity localizations in detail. Increasing the SiO_2 core size results in high energy confinements distributed evenly in thin shell structure while the LSPR wavelength of the NP redshifts from 515 nm to 640 nm. Moreover, compared to bare Au NP, maximum absorption efficiency is enhanced by 30% with SiO_2 core-Au shell case. Further increase of dielectric core volume for FNP case shows decreasing maximum Q_{abs} values, which are still larger than the absorption efficiency of bare Au NP with 50 nm diameter.

It is observed that SiO_2 core with Au and Ag shell cases have greater maximum absorption efficiencies due to the evenly distributed field localizations in the metal shells by comparing dielectric core/metal shell cases in Figures 3.2 and 3.3. However, when GaP is used at core, field localizations can shift to the core with a reduction of absorption efficiency of the NP.

Moreover, metal shell domination is observed for dielectric cores with f_r values smaller than 0.2 that results in LSPR wavelengths to be located around the LSPR wavelength of the bare metallic NP. For dielectric core-metal shell pairs, it is found that increasing f_r of the core material results in a redshift of the LSPR wavelength except in GaP core-Ag shell case, which can be attributed to nonzero imaginary part of the refractive index of the GaP for the wavelength range given for this pair. Therefore, the effect of dielectric cores on the plasmonic response of these core-shell pairs cannot be generalized and these pairs should be considered individually in order to study their absorption behavior and LSPR response.

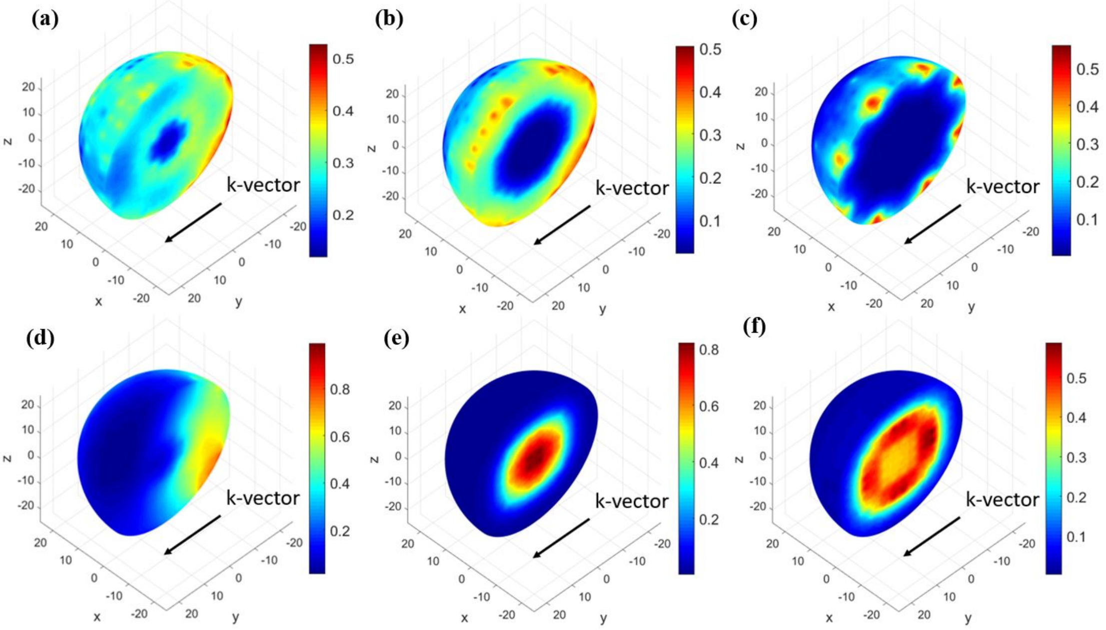

Figure 3.4. Normalized field intensity plots for SiO_2 core/ Au shell (a-c) and Au core/ GaP shell (d-f) NPs with a cut on x = 0 plane and $D_s = 50$ nm. Each case is shown with respect to k-vector direction. (a) $D_c = 15$ nm, $\lambda_{max} = 515$ nm, maximum $Q_{abs} = 1.04$. (b) $D_c = 33$ nm, $\lambda_{max} = 535$ nm, maximum $Q_{abs} = 1.34$. (c) $D_c = 45$ nm, $\lambda_{max} = 640$ nm, maximum $Q_{abs} = 1.06$. (d) $D_c = 15$ nm, $\lambda_{max} = 300$ nm, maximum $Q_{abs} = 0.58$. (e) $D_c = 27$ nm, $\lambda_{max} = 705$ nm, maximum $Q_{abs} = 1.12$. (f) $D_c = 33$ nm, $\lambda_{max} = 660$ nm, maximum $Q_{abs} = 1.61$.

3.3.2. Metallic Core with Dielectric Shell

Contrary to dielectric core-metallic shell pairs in the previous section, metallic core-dielectric shell NPs have opposite LSPR response especially for their tunability range. Comparing the Figures 3.2(a,b) and 3.5(a,b), the total LSPR shift of the GaP/Ag pairs is observed to be greater for Ag core-GaP shell. As the f_r of Ag core decreases, LSPR wavelength of the Ag core-GaP shell shifts from 465 nm to 620 nm for FC case, and from 445 nm to 630 nm for FNP case, as shown in Figure 3.5(b). Compared to the LSPR wavelength of the bare Ag NP, redshift of LSPR wavelength is observed for both FC and FNP cases of Ag core-GaP shell NP. Moreover, absorption enhancement of 4% can be achieved if Ag is at core rather than being at shell when it is paired with GaP. For both FC and FNP cases, almost 60% f_r of the Ag core leads to the highest absorption efficiency values. While the maximum absorption efficiency of single Ag NP with 50 nm diameter is 4.54 at 365 nm, the maximum absorption efficiency is found to be 4.74 at 510 nm for the Ag core-GaP shell with FNP case in Figure 3.5(b). Hence it is possible to use Ag core-GaP shell for enhanced absorption with a redshifted LSPR wavelength. The absorption profiles of Ag core-GaP shell in Figure 3.5(b) for both FC and FNP cases exhibit similar pattern with respect to f_r. Decreasing the f_r of the Ag core results in LSPR wavelength shifting from 365 nm to longer wavelengths. Contrary to GaP core-Ag shell case, where increasing the GaP core results in blueshift of LSPR wavelengths, increasing the GaP shell volume relative to the Ag core provides a redshift of LSPR. This opposite LSPR response is due to the increasing dielectric constant of the surrounding medium of Ag with the introduction of GaP shell.

Similar to the GaP/Ag pairs, the LSPR responses of SiO2/Ag pairs show different phenomenon, when the core and shell materials are switched. As shown in Figures 3.5(c,d), the range of LSPR wavelengths of Ag core-SiO_2 shell is narrower as compared to the ones in SiO_2 core-Ag shell case being presented in Figures 3.2(c,d). For both FC and FNP cases, changing the f_r of Ag core results in only 40 nm change of LSPR wavelength. There is an obvious trade-off between the absorption enhancement and LSPR wavelength with the tunability of the NP. As stated in dielectric core-metal shell section (3.3.1), SiO_2 core-Ag shell can have absorption enhancement of 8.81% with 355 nm of LSPR wavelength shift in FC case. However, when the core and shell are switched to Ag and SiO_2, respectively, absorption enhancement of 19% is obtained with an absorption efficiency of 5.40 and 25 nm redshift of LSPR wavelength.

As shown in Figures 3.5(c,d), decreasing the f_r of the Ag to 30% results in a redshift of LSPR peak wavelengths. Further decrease in the f_r of the Ag core with both GaP and SiO_2 dielectric shell cases, shell starts to dominate over the plasmon response with damping of absorption and fluctuating LSPR wavelengths.

For the GaP core-Au shell being shown in Figures 3.3(a,b), maximum absorption efficiency of the NP is below 1 with LSPR wavelength at 515 nm. However, when Au core-GaP shell pair is investigated, maximum absorption efficiency is obtained as 1.61 at 660 nm of LSPR wavelength with 30% f_r of the Au core in the FNP case, as shown in Figures 3.4(f) and 3.6(b). Considering bare Au NP having maximum absorption efficiency of 1.03 at 515 nm wavelength, GaP shell with Au core can both enhance

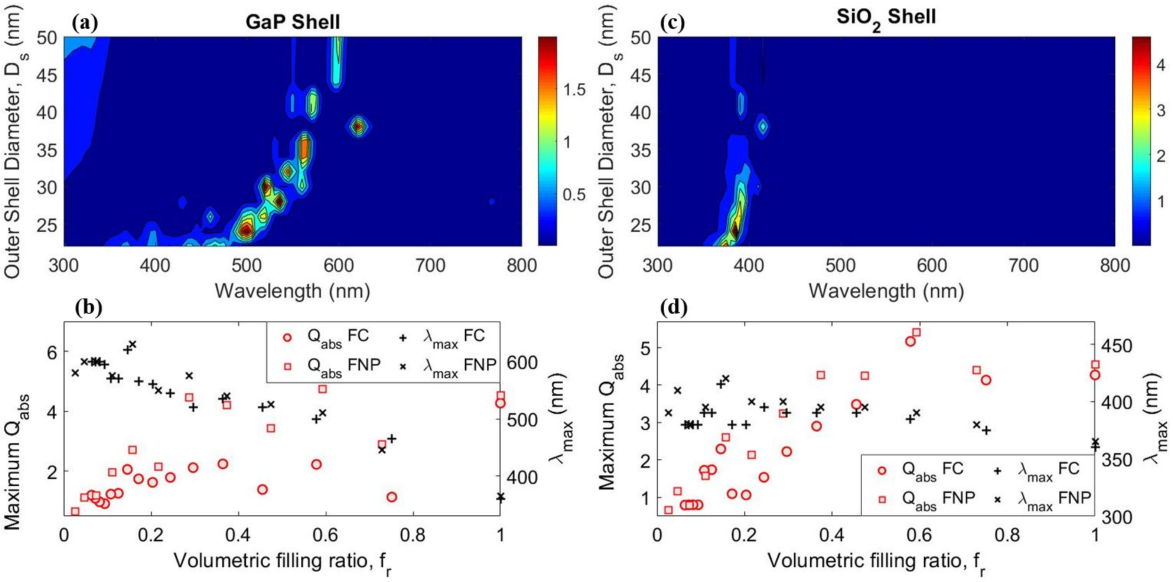

Figure 3.5. Ag core with GaP (a-b) and SiO_2 (c-d) shell: Contour plots of absorption efficiency as a function of wavelength for FC (a,c). Maximum Q_{abs} and LSPR wavelengths, λ_{max}, as function of f_r for FC and FNP (b,d).

the absorption up to 56% and redshift the LSPR wavelength by 145 nm. Moreover, tunability of LSPR wavelength is greater than the case with GaP core-Au shell. As shown in Figures 3.6(a,b), decreasing Au core f_r results in LSPR wavelengths being shifted from 550 nm to 705 nm. Similar redshift effect of the increasing dielectric shell was observed with the Ag core-dielectric shell cases as the dielectric constant of the surrounding medium is increased due to the introduction of shell. As shown in Figure 3.6(b), decreasing the f_r of the core below 30% drastically decreases the absorption efficiency as the GaP shell dominates the plasmon response of the core-shell at lower wavelengths.

As discussed in Sections 3.1 and 3.3.1, the wavelengths smaller than 490 nm can induce absorption in GaP material due to its nonzero imaginary part of the refractive index, k. Hence, most of the field localization takes place on the GaP shell with LSPR wavelength of 300 nm, as shown in Figure 3.4(d). Figures 3.4(e,f) depict increasing the Au core size, while keeping the NP diameter at 50 nm, shifts the maximum field intensity regions towards the Au core with greater absorption efficiency values. Since the LSPR wavelengths are greater than 490 nm in Figures 3.4(e,f), GaP shell can act as a perfectly dielectric material, which can induce a redshift of LSPR wavelengths with an increasing shell thickness.

As shown in Figure 3.6(a), for the FC case with the outer shell diameter between 40 – 50 nm, primary and secondary LSPR regions exist although the absorption is observed to be relatively low. Further decrease in the shell diameter prevents formation of the multiple peaks of the LSPR response as the Au core starts to dominate over GaP shell. Au core domination is also observed in Figures 3.4(d-f) and 3.6(b), where the LSPR wavelengths also blueshift towards the LSPR wavelength of the bare Au NP.

The GaP shell extends the range of LSPR wavelengths for both metallic cores. On the other hand, the SiO_2 shell restricts the range of LSPR shifts. Comparing the Figures 3.3(d) and 3.6(d) for SiO_2/Au pairs, it is observed that the range of LSPR wavelengths narrow down from 195 nm to 20 nm when SiO_2 shell is used. Moreover, shielding of SiO_2 shell leads to the lower absorption efficiency values with decreasing

f_r of the Au core, as shown in Figure 3.6(d). Hence, the absorption enhancement with respect to the bare Au NP cannot be achieved with this core-shell structure.

All metallic core-dielectric shell pairs show that dielectric shell can redshift the LSPR wavelength of the NPs compared to ones for the bare Ag and Au NPs. Besides a redshift of the LSPR wavelength, there is absorption enhancement with the introduction of dielectric shell except for the case of Au core- SiO_2 shell NPs. It is useful to choose silica shell with Ag core for selective heating applications of NPs that have enhanced absorption and chemically stable surface. The other case with Au core-GaP shell can be used for nanomanufacturing applications as they have 56% more absorption at wavelengths such as 660 nm.

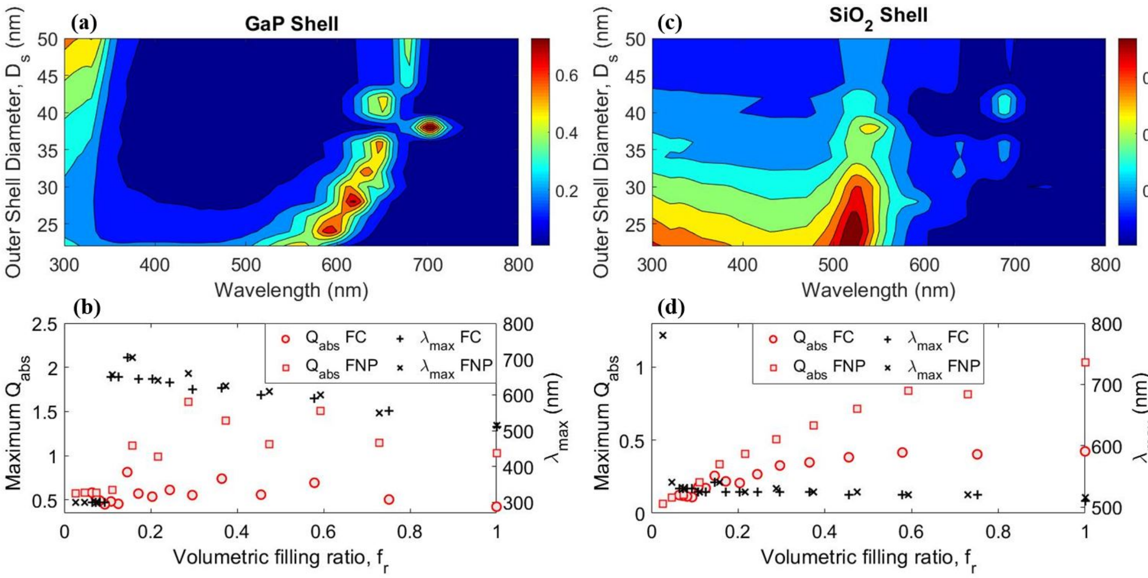

Figure 3.6. Au core with GaP (a-b) and SiO_2 (c-d) shell: Contour plots of absorption efficiency as a function of wavelength for FC (a,c). Maximum Q_{abs} and LSPR wavelengths, λ_{max}, as function of f_r for FC and FNP (b,d).

4. ABSORPTION AND PLASMON RESONANCE OF BI-METALLIC CORE-SHELL NANOPARTICLES ON A DIELECTRIC SUBSTRATE

4.1. Problem Statement and Method

This study is divided into three parts for the comparison of Ag-Au core-shell metallic structures placed on a semi-infinite BK7 glass substrate that is subjected to an incident wave below the surface with an incident angle (θ_i) greater than the critical angle (θ_c), resulting a total internal reflection (TIR). Figure 3.1 from Section 3.1 depicts the resultant surface evanescent waves that interacts with the core-shell structure defined with core radius (R_c) or outer shell radius (R_s). In this configuration, TE-polarized wave is preferred for the investigation as the resulting larger absorption efficiency (Q_{abs}) is than the TM-polarized wave. The incident TE-polarized wave is in the range of 300 nm to 800 nm. The first numerical analysis is based on the effect of size configuration on the absorption efficiency (Q_{abs}) and LSPR wavelength (λ_{max}) of the core-shell structure being placed in vacuum on top of the substrate. Size effect is studied for fixed core (FC) and fixed nanoparticle size (FNP) cases for Ag core-Au shell (Ag@Au) and Au core-Ag shell (Au@Ag) core-shell NPs. In the FC case, outer shell diameter is increased gradually to 50 nm while metallic core is kept at 20 nm in diameter. The FNP cases involve core diameters between 15 nm and 45 nm as the overall NP size is fixed at 50 nm in diameter. The size configurations for the FNP and FC cases are defined for core and outer shell diameters with 3 nm and 2 nm increments, respectively and is presented in Table 4.1. Moreover, the change in core-shell size is parameterized with the volumetric filling ratio (f_r) of the core material, which is defined as the ratio of the core volume based on core diameter, D_c, to the nanoparticle volume defined based on outer shell diameter, D_s, as $f_r = (D_c/D_s)^3$. The f_r range considered is presented in Table 4.1.

Table 4.1. Core and shell sizes for FC and FNP cases of bimetallic NPS with corresponding volumetric filling ratio (f_r) ranges.

NP Type	D_c **(nm)**	D_s **(nm)**	f_r **Range**
Fixed Core	20	22-50	0.751 – 0.064
(FC)	20	20	1
Fixed NP	15-45	50	0.027 – 0.729
(FNP)	50	50	1

Table 4.2. Refractive indices of the medium,n_m, and corresponding incident angles, θ_i.

$\boldsymbol{n_m}$	1	1.1	1.2	1.25	1.3	1.4	1.5
$\boldsymbol{\theta_i}$	45°	50°	55°	60°	60°	70°	85°

The second part of the problem considers the refractive index sensitivity of these structures as the dielectric medium is varied. The effect of the surrounding medium on the Q_{abs} and λ_{max} of the metallic core-shell NPs is studied with only FC cases. Since the refractive index of the BK7 substrate is about 1.52, the medium refractive indices are varied between 1 and 1.5 so that the incident angle between θ_c and 90°can support TIR to create surface evanescent wave above the substrate. Table 4.2 shows considered medium refractive indices (n_m) with their corresponding incident angles (θ_i), which are greater than the critical angles (θ_c) defined by Snell's law of refraction.

The last part of the problem is designated to consider the maximum absorption efficiency cases of Ag@Au and Au@Ag core-shell nanoparticles with fixed nanoparticle size found in the first part. The effects of AFM tip on the LSPR response of the nanoparticles is investigated with the selected pairs. In addition to the TE-polarized wave in the first and second parts, TM-polarized case is also considered in this part due to its partial polarization along the tip-NP axis as stated in [9,33,35]. The study in [35] showed that after 600 nm, absorption level of the AuNP is converged to minimum values with negligible changes. However, the wavelength range of 300 nm-450 nm in [35] and [47] was not enough for the AgNP to experience the effects of the dielectric transition of the AFM tip material. Therefore, the incident wavelength in this part is considered in 300 nm-600 nm range to examine the LSPR response of both bare metal and core-shell NPs. As shown in the Figure 4.1, the position of the spherical NP is considered as the origin of the cartesian coordinate system, and the tip is positioned over the NP at a coordinate (0, 0, 52) nm. The geometry of the AFM tip is defined with 10 nm tip radius, r_{tip}, 50 nm shaft diameter, D_{shaft}, so that the cone angle, α, is 16.7°. Both TE and TM polarized incident waves are considered; where TE-polarized wave creates the evanescent wave transverse to tip-NP axis in y direction, whereas TM-polarized wave has both y and z components.

Throughout this study, the spectral refractive indices of the Ag and Au metals are obtained from the experimental measurements reported in [66], while an empirical relation of refractive index with wavelength based on Sellmeier equation is used for the

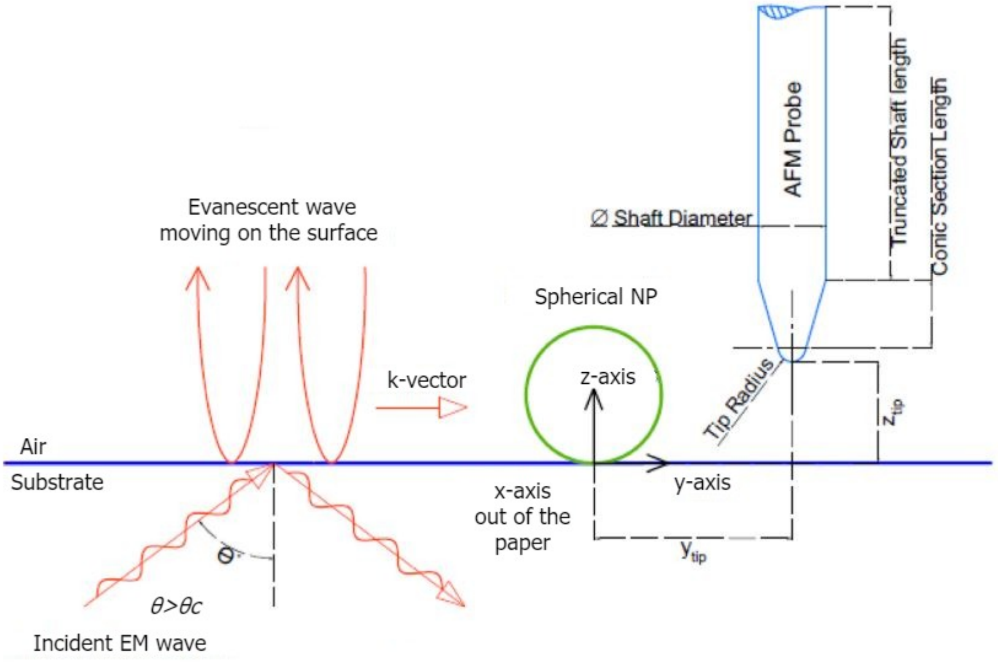

Figure 4.1. A cross-sectional view of the AFM probe and nanoparticle configuration [33].

BK7 substrate. For the AFM tip materials, the data for GaP and Silicon (Si) are used from [67,68], respectively.

4.2. Numerical Aspects

In the first part of the problem with single core-shell nanoparticles, the accurate calculation of absorption efficiency necessitates sufficient number of dipoles (N_{NP}) to represent the nanoparticles. Hence, an optimum dipole number is determined as N_{NP}=1472 based on the converged value of maximum Q_{abs} values, which has been considered in the previous study of dielectric-metal core-shell pairs [28]. However, for the AFM tip and NP interactions, N_{NP} is decreased to 552 due to significant increase in the required computation time and memory with the introduction of the AFM probe. Then, number of dipoles for the AFM probe, N_{AFM}, is analyzed for the optimum shaft length so that further increase in the probe length does not change the absorption significantly. In this study, the optimal shaft length is considered when the relative change of absorption becomes within 5%. Similar design has been used for the single AuNP and SiO_2 core-Au shell cases with the truncated shaft length of 390 nm in [32,33].

4.3. Results and Discussions

4.3.1. Fixed Core and Fixed Nanoparticle Size

The plasmon responses of metal-metal core-shell NPs are numerically analyzed considering their spectral absorption efficiency values for both FC and FNP cases as shown in Figure 4.2. Plasmon mode hybridizations are observed in FC and FNP cases of Ag core-Au shell (Ag@Au) NPs with varying shell thickness, *t*, between 5 nm and 15 nm. Increase in Au shell thickness results in a redshift of the ordinary modes (secondary peaks) in longer wavelength that are located around 515 nm as shown in Figures 4.2(a,b). This mode corresponds to the LSPR wavelength of bare Au NP, which explains the Au shell domination as its thickness increases. Even if the extraordinary modes (first peaks) in Figure 4.2(a) is not clear for shell thicknesses greater than 5 nm, an increase in shell thickness blueshifts this mode. This mode of plasmon resonance corresponds to field enhancements at the core-shell interface, while the ordinary modes are result of field localizations at the outer surface of the Au shell.

Contrary to Ag@Au case, the spectral absorption profiles of Au core-Ag shell (Au@Ag) case with varying shell thicknesses have greatest absorption peak at the extraordinary modes. Figures 4.2(c,d) show the shield effect of Ag shell on the plasmon response of the core-shell NP with narrower LSPR wavelength bandwidth. LSPR wavelengths redshifts by 10 nm to 365 nm, which corresponds to bare Ag NP's plasmon wavelength, as the Ag shell thickness increases for both FC and FNP cases. Ordinary modes (secondary peaks) are observed around 420 nm, with decreasing Q_{abs} values in Figure 4.2(d), for the Ag shell thickness greater than 5 nm. In this scenario, Ag shell dominates over the Au core with field localizations at the outer shell surface for both extraordinary and ordinary modes of the LSPR wavelength.

In Figure 4.3, the effects of size configuration on the LSPR response of the NPs are further analyzed with the contour plots of FC cases and the volumetric filling

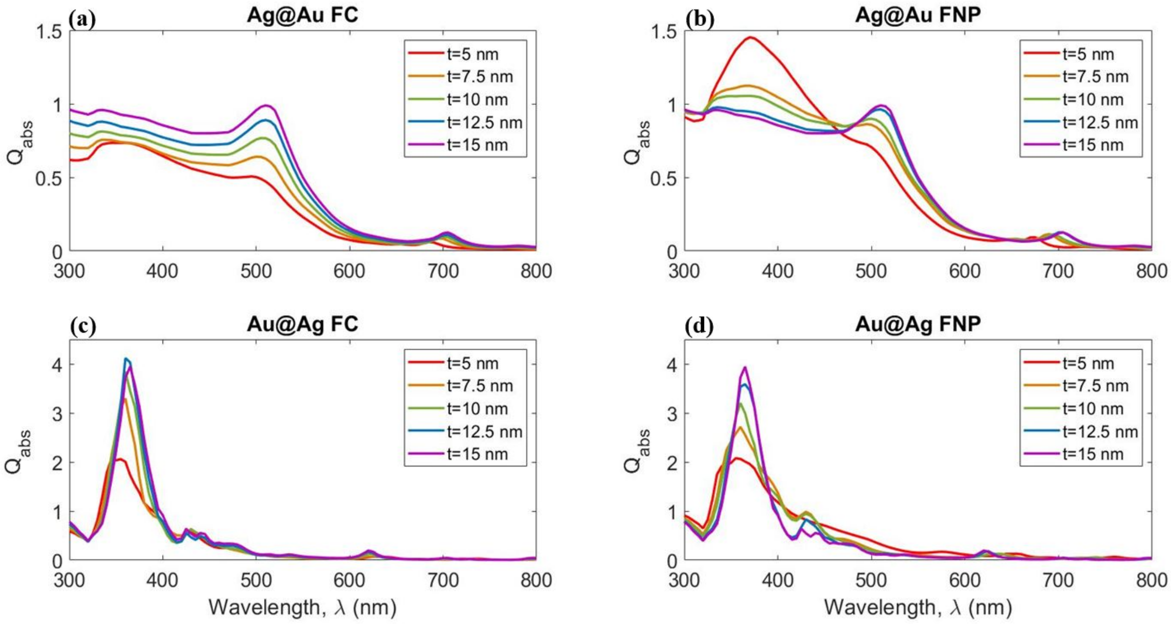

Figure 4.2. Spectral absorption efficiency,Q_{abs}, of Ag core-Au shell (a-b) and Au core-Ag shell (c-d), represented for FC (a,c) and FNP (b,d) cases.

ratio of the core materials based on the size configurations summarized in Table 4.1. As discussed above, Ag@Au core-shell NP can support plasmon hybridization, which is depicted in Figure 4.3(a) with two peak regions located around 365 nm and 515 nm. For outer shell diameters smaller than 25 nm, further decrease in shell thickness ($t < 5nm$) results in greater Q_{abs} values, which cannot be observed in Figure 4.2(a). Further Au shell thickness increase in this FC case dominates the ordinary mode so that its LSPR wavelength moves towards that of the bare Au NP (515 nm). When the volumetric filling ratio, f_r, of the core is smaller than 0.2, the absorption enhancement is not observed as shown in Figure 4.3(b). However, further increase in f_r beyond 0.2 leads to increasing maximum Q_{abs} values of Ag@Au NP by 22% and 91% for FC and FNP cases, respectively. When the f_r reaches its highest value, FNP case has a greater absorption than the one in the FC case since the FNP represents greater Ag core size (45 nm) than the FC case with 20 nm core diameter. As the f_r of the Ag core increases, the LSPR wavelength of the Ag@Au NP stabilizes around the bare Ag NP's

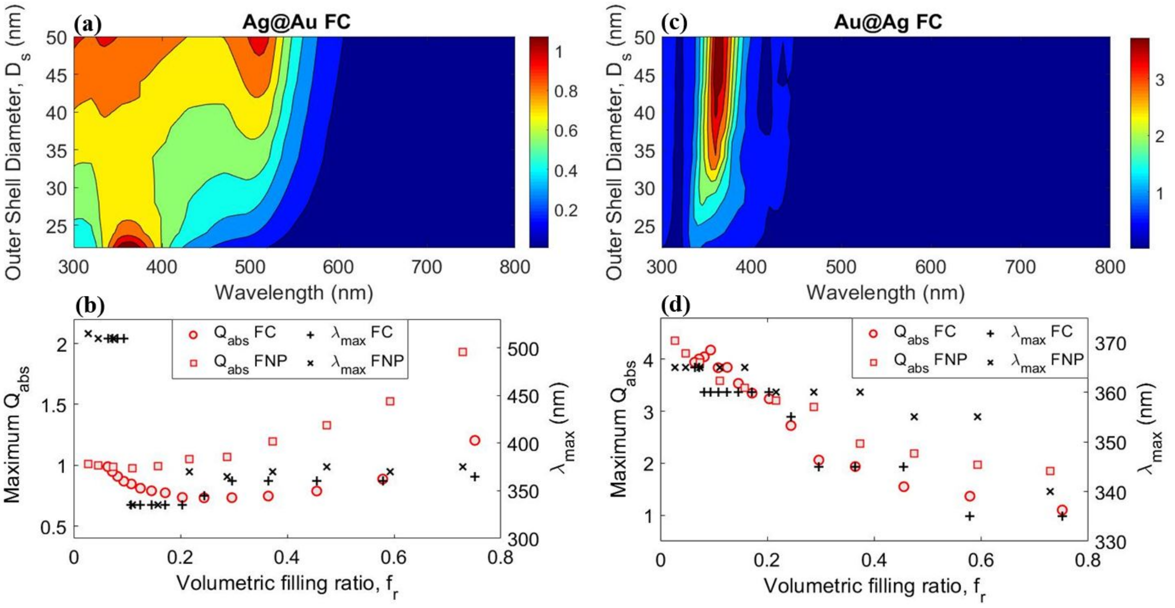

Figure 4.3. Ag core-Au shell (a-b) and Au core-Ag shell (c-d): Contour plots of spectral absorption efficiency, Q_{abs}, for FC (a,c). Maximum Q_{abs} and LSPR wavelengths, λ_{max}, with respect to volumetric filling ratio, f_r, for both FC and FNP cases (b,d).

LSRP wavelength. Similar to spectral absorption efficiency patterns shown in Figures 4.2(c,d), Ag shell dominates the LSPR wavelengths around 365 nm for the cases with f_r of the Au core smaller than 0.2, as shown in Figures 4.3(c,d). For both FC and FNP cases of the Au@Ag NP, further increase in f_r, results in blueshifts of the LSPR wavelength towards 335 nm as its maximum Q_{abs} values decreases by 280% and 135%, respectively. By comparing the amount of damping in the Q_{abs} values and shifts in the LSPR wavelengths, metal-metal core-shell NPs can be optically detected for material prediction and core/shell formation.

4.3.2. Refractive Index Sensitivity

The effect of surrounding medium on the plasmon response of the metal-metal core-shell NPs on BK7 substrate is analyzed for the FC cases with 5 different shell thicknesses in order to include the shell formation effect. Figure 4.4 depicts the spectral Q_{abs} values with three different medium refractive indices, n_m, for both Ag@Au and Au@Ag NPs. The corresponding incident angles of the TE-polarized wave are chosen from Table 4.2 for each medium refractive index. Hybridization of plasmon modes

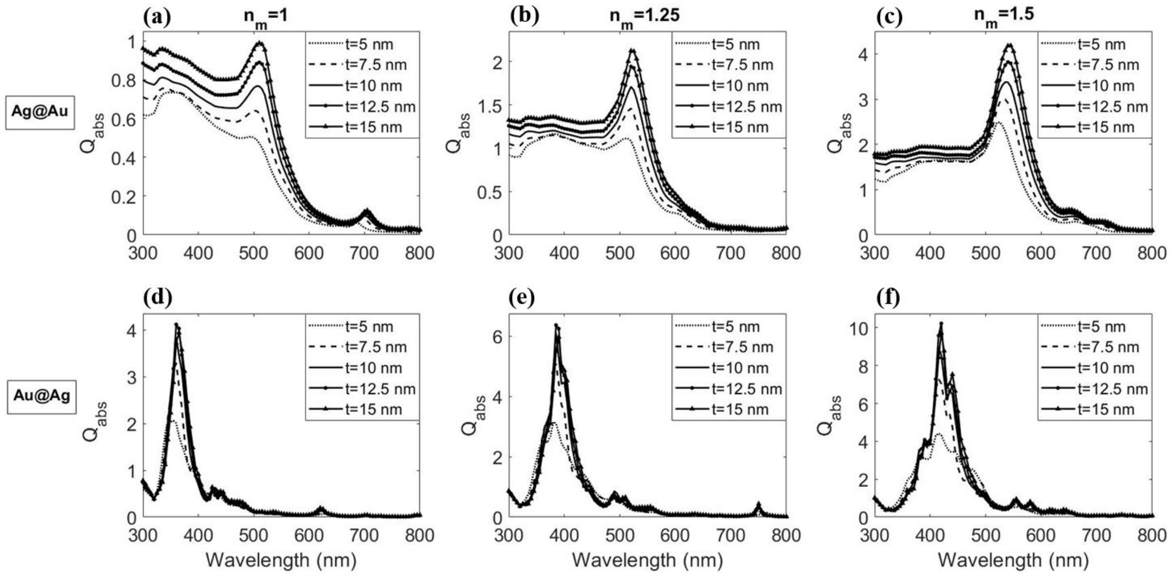

Figure 4.4. Spectral absorption efficiency, Q_{abs}, for Ag@Au (a-c) and Au@Ag (d-f) in mediums with n_m= 1 (a,d), 1.25 (b,e), and 1.5 (c,f).

diminishes as the refractive index of surrounding medium increases for Ag@Au core-shell case as shown in Figures 4.4(a-c). Compared to the vacuum case ($n_m = 1$) in Figure 4.4(a), increasing n_m leads to greater Q_{abs} values with redshifts in LSPR wavelengths from 510 nm to 540 nm, for maximum shell thickness case. Here, in Figures 4.4(a-c), an increase in n_m also leads to broadening and narrowing of extraordinary and ordinary LSPR modes, respectively. In this scenario, the interaction between Au shell and the dielectric medium dominates the one at core-shell interface. Hence, the only plasmon response of Ag@Au NP is observed for the ordinary mode. Similar LSPR wavelength redshifts and absorption enhancement can be observed in Au@Ag case with increase in n_m. However, the spectral Q_{abs} values of the Au@Ag case in Figures 4.4(d-f) show the opposite trend of plasmon peak formation of Ag@Au case. While the vacuum case provides one LSPR wavelength around 365 nm, increase in n_m causes distinguishable ordinary modes at longer wavelengths around 415 nm. These secondary peaks of the LSPR wavelengths start to move away from the first peaks as the refractive index of the medium is increased. Moreover, both Ag@Au and Au@Ag cases have enhanced absorption due to increase in both nanoparticle size and refractive index of the medium.

Further analysis is carried out with n_m values between 1 and 1.5 for the selected Ag@Au and Au@Ag NPs with D_c=20 nm and D_s=50 nm, which gives the maximum overall NP size in this study. As discussed above, increasing n_m values give rise to redshifts in LSPR wavelengths with an increase of Q_{abs} values. For the selected size configurations, numerical simulations are performed with finer wavelength ranges, which are around the previously evaluated LSPR wavelengths. Figure 4.5 shows the maximum Q_{abs} and corresponding LSPR wavelengths as a function of n_m for both metal-metal cases. A gradual increase in the refractive index of the medium from 1 to 1.5 shows that LSPR wavelength of the Ag@Au NP redshifts by 32 nm with absorption enhancement by more than 320%. In the Au@Ag case, this enhancement is observed as 140% with redshift in LSPR wavelength by 57 nm. This comparison shows that there is a balance between the tunability range of the LSPR wavelength and the absorption enhancement.

4.3.3. AFM Tip and Nanoparticle Interaction

As discussed in Section 4.1, an optimum shaft length is analyzed with the converged values of absorption efficiency of the metal nanoparticle. One case is evaluated for AuNP in 50 nm diameter illuminated by TM-polarized wave at λ=520 nm. The AFM probe is located above the NP at (0, 0, 52) nm and made of silicon with the shaft length varying between 150 nm and 810 nm while the nanoparticle is represented with N_{NP}=552 rather than 1472. As shown in Figure 4.6, changes in AFM shaft length results in oscillating absorption efficiency values that converge to Q_{abs}=1.74. Considering 5% relative error band, optimum truncated shaft length is found as L_{shaft}=470 nm with corresponding number of dipoles for the AFM probe, N_{AFM}=8083.

The effect of AFM tip material is compared with the spectral absorption efficiency

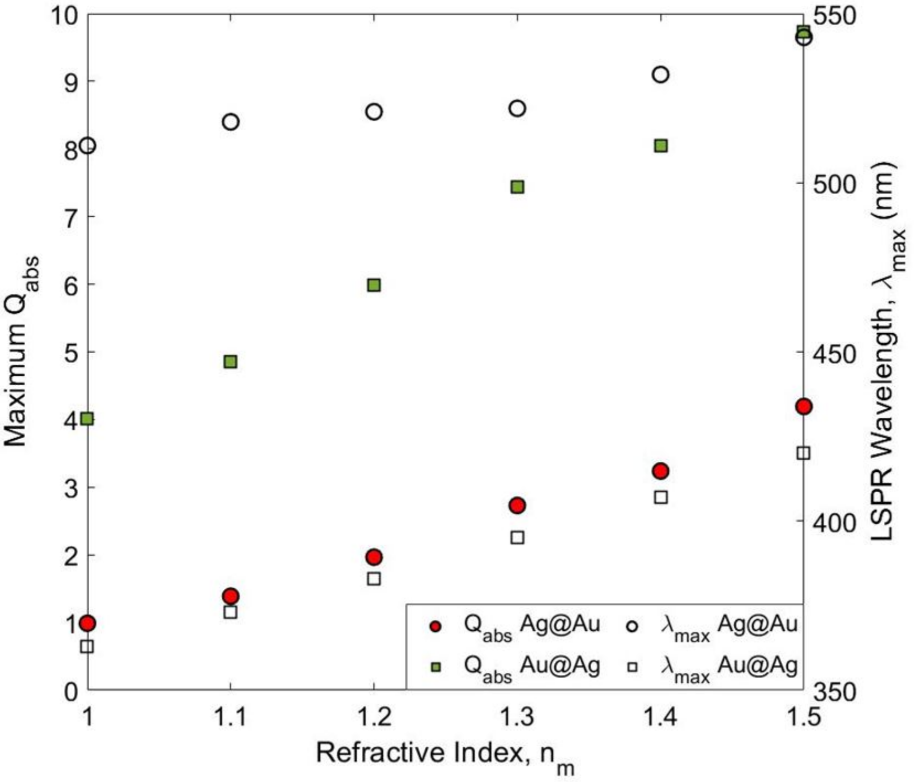

Figure 4.5. Maximum Q_{abs} and LSPR wavelengths, λ_{max}, with respect to medium refractive indices, n_m for both both Ag@Au and Au@Ag.

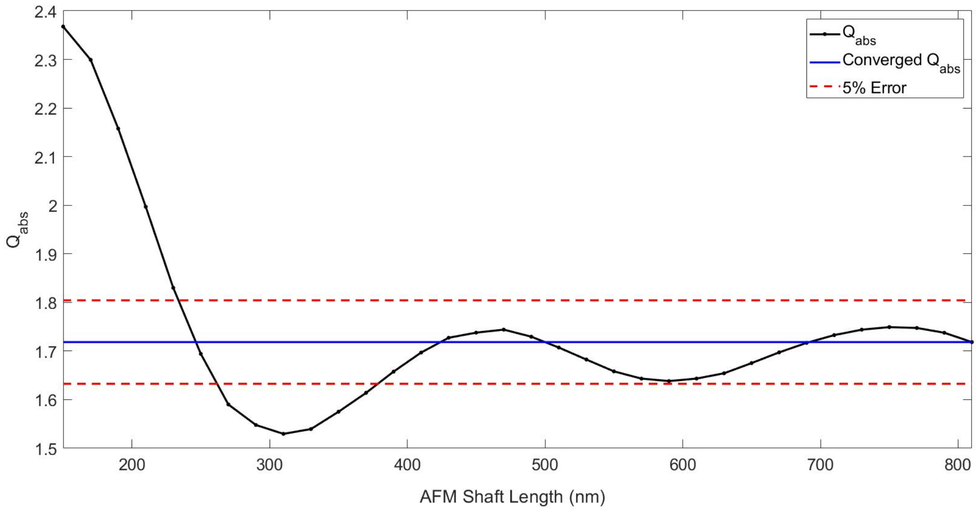

Figure 4.6. Converged absorption efficiency, Q_{abs}, values of AuNP with changes in AFM shaft length.

Table 4.3. Summary of the maximum absorption efficiency values of the nanoparticles with their LSPR peak wavelengths represented as Q_{abs} @ λ_{max}.

NP type *(D=50 nm)*	**Polarization**	Q_{abs} **@** λ_{max}		
		w/o AFM tip	**GaP AFM tip**	**Si AFM tip**
AuNP	TE	1.07 @ 515 nm	1.02 @ 520 nm	1.02 @ 520 nm
	TM	1.05 @ 515 nm	1.75 @520 nm	1.74@520 nm
AgNP	TE	4.95 @ 370 nm	4.77 @ 370 nm	4.75 @ 370 nm
	TM	4.62 @ 370 nm	3.31 @ 370 nm	2.95 @ 370 nm
		0.95 @ 490 nm	1.62 @ 490 nm	1.53 @ 490 nm
Ag@Au (D_c=45 nm)	TE	1.84 @ 380 nm	1.70 @ 380 nm	1.69 @ 380 nm
	TM	1.79 @ 380 nm	2.02 @ 390 nm	1.96 @ 390 nm
Au@Ag (D_c=15 nm)	TE	5.00 @ 370 nm	4.83 @ 370 nm	4.81 @ 370 nm
	TM	4.65 @ 370 nm	3.35 @ 370 nm	3.01 @ 370 nm
		0.93 @ 490 nm	1.61 @ 490 nm	1.52 @ 490 nm

values of core-shell and bare metallic nanoparticles for the wavelengths between 300 nm and 600 nm. The core-shell pairs are selected from the optimum size configurations found in Section 4.3.1 with Ag@Au (D_c=45 nm, D_s=50 nm) and Au@Ag (D_c=15 nm, D_s=50 nm). Predicted Q_{abs} values of the bare AgNP and AuNP with D=50 nm are taken as reference for the comparisons. An example of tip material effect is shown in Figure 4.7 for bare metallic nanoparticles illuminated with TE and TM polarized waves. The results show that TE-polarized cases represent negligible variation in maximum Q_{abs} values for both AgNP and AuNP under GaP and Si AFM tip. Since TE-polarized wave is transverse to tip-NP axis, the spectral Q_{abs} values follow the ones found for bare metallic NP's only with damping. The damping effect of AFM introduction is summarized for all NP types including the core-shell NPs in Table 4.3, where the maximum absorption efficiency values found in no AFM cases are decreased when GaP and Si AFM tips are used in TE-polarized case.

Considering TM-polarized cases of AgNP under AFM tip in Figure 4.7(a), the spectral absorption behavior shows that use of GaP tip results in maximum Q_{abs} values 12% at the 1^{st} peak and 6% at the 2^{nd} peak greater than the ones found with use of Si tip. The corresponding LSPR wavelength, λ_{max}, for these two peaks are 370 nm and 490 nm, respectively. Since both tip material behaves as a perfectly dielectric after λ=490 nm, absorbing behavior of the tips creates near-field interactions damping the absorption of AgNP at λ=370 nm. This effect can also be seen in Figure 4.7(b) for AuNP with TM-polarization, where there is an oscillatory behavior of Q_{abs} values for the wavelengths smaller than 490 nm. Therefore, the variation in maximum Q_{abs} values is negligible, below 1%, for both tip materials as they behave perfectly dielectric at the peak wavelength (λ_{max}) of the AuNP case.

Similar to bare metal cases, GaP AFM tip is found to be more effective than Si AFM tip for absorption enhancement of the core-shell NPs, as listed in Table 4.3. Hence, further comparisons for the spectral absorption behavior of the NPs will be based on GaP AFM tip. The comparison of the selected core-shell pairs with TE and TM polarized cases for the absorption enhancement is considered next.

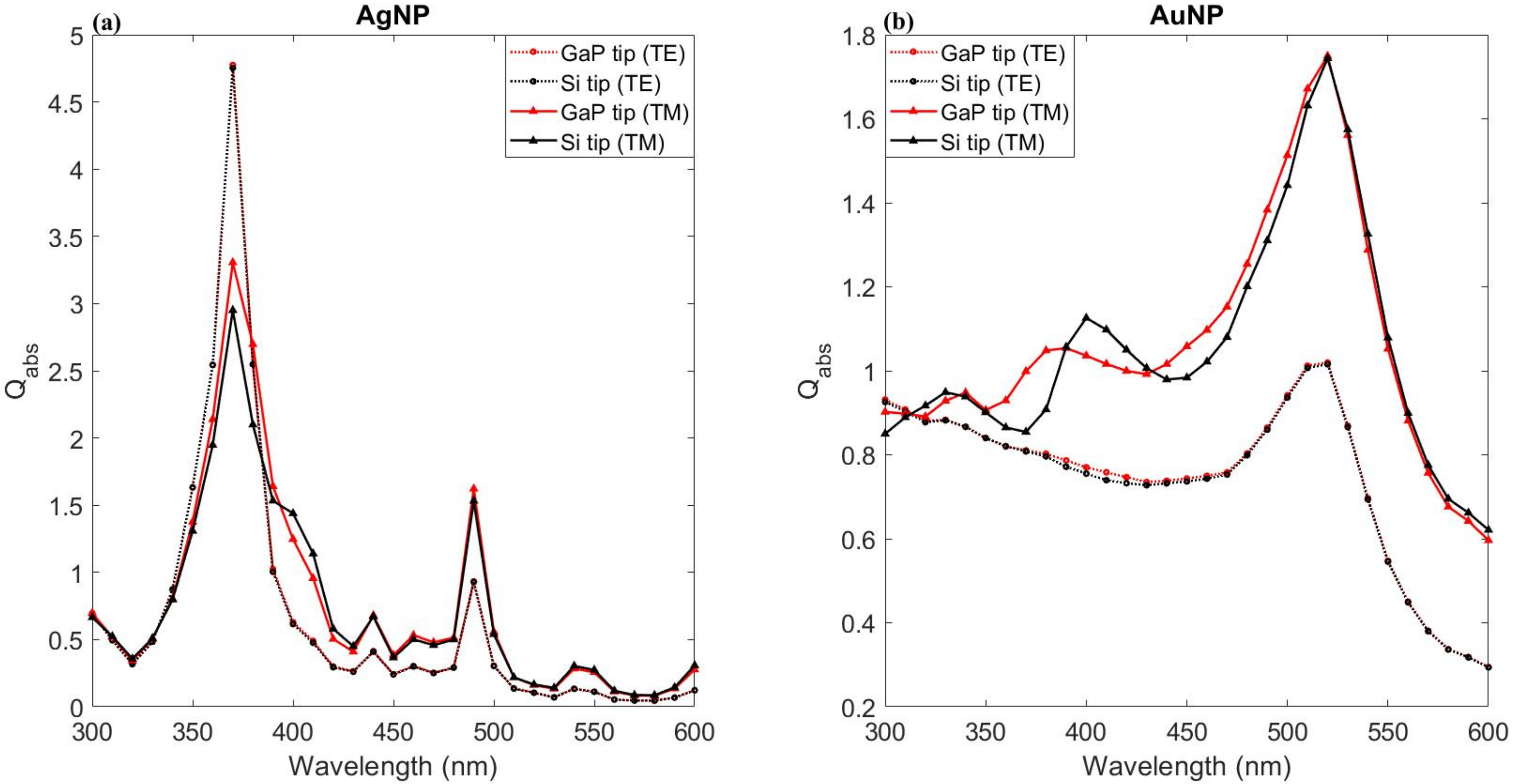

Figure 4.7. Spectral absorption efficiency, Q_{abs}, of AgNP (a) and AuNP (b) under the effect of GaP and Si AFM tips with TE/TM-polarizations.

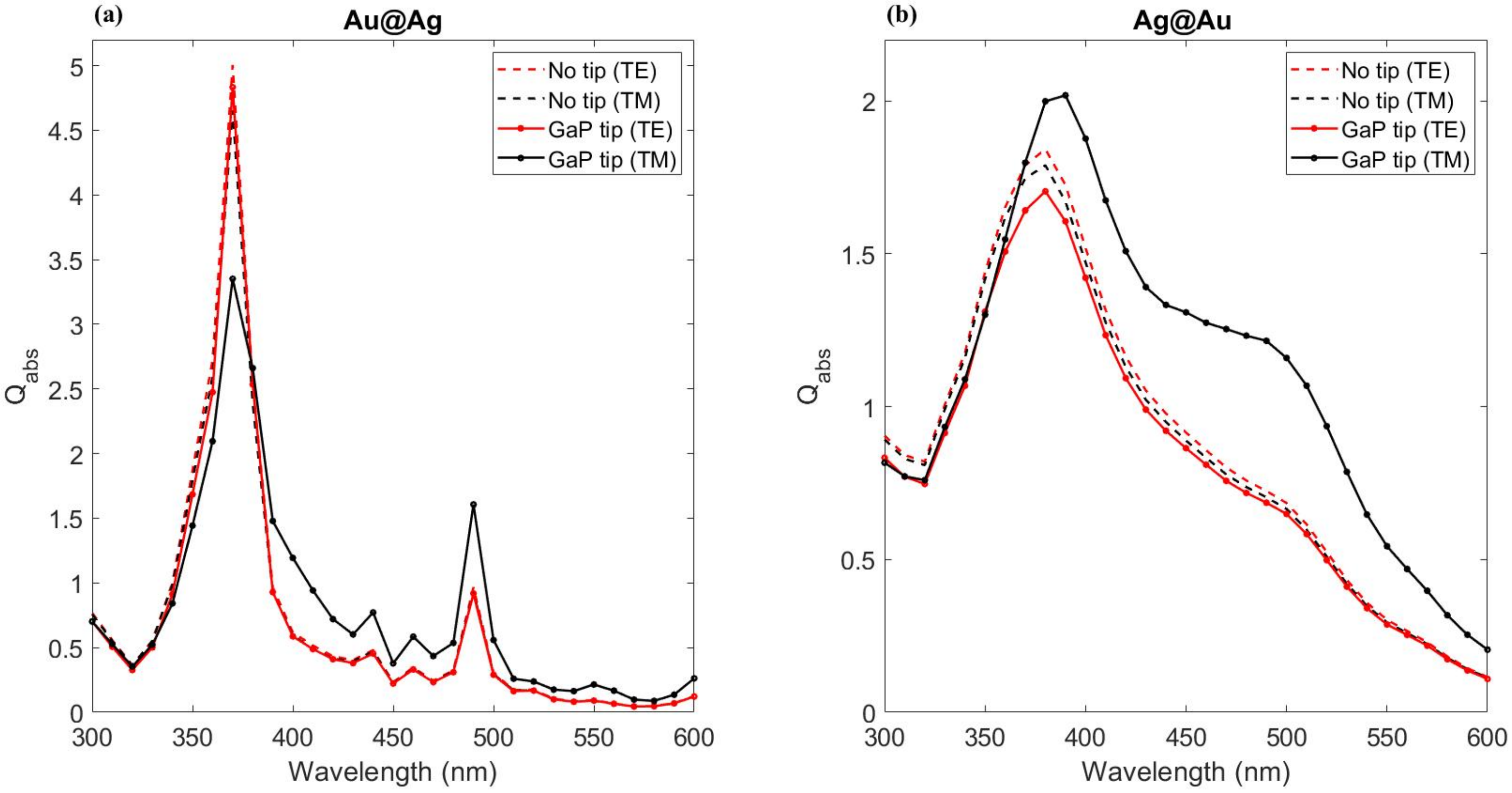

Figure 4.8. Spectral absorption efficiency, Q_{abs}, of core-shell pairs: Ag@Au (a) and Au@Ag (b) with and without using GaP AFM tip in TE/TM-polarization cases.

It is shown in Figure 4.8(a) that spectral absorption pattern of Au@Ag does not change for TE and TM-polarized cases when there is no AFM tip. Absorption pattern similarity is also observed in TE case with and without GaP AFM tip. As the TE-polarization direction is transverse to tip-NP axis, AFM tip does not alter the field localizations of the NP as shown in Figures 4.9(a,b). It is found that the use of GaP AFM tip decreases the maximum absorption efficiency only by 3.4% in TE-polarized case. For the TM-polarization cases, the maximum Q_{abs} of the Au@Ag NP is damped by 28% at λ=370 nm while it is enhanced by 73% at λ=490 nm due to presence of the GaP tip. This kind of damping and enhancement of the absorption efficiency also exist in bare AgNP case shown in Figure 4.7(a). The main reason behind this scheme is the Ag shell domination for the selected Au@Ag pair which can be seen in Figure 4.9, where the local field intensities are collected mostly on the outer shell of the NP.

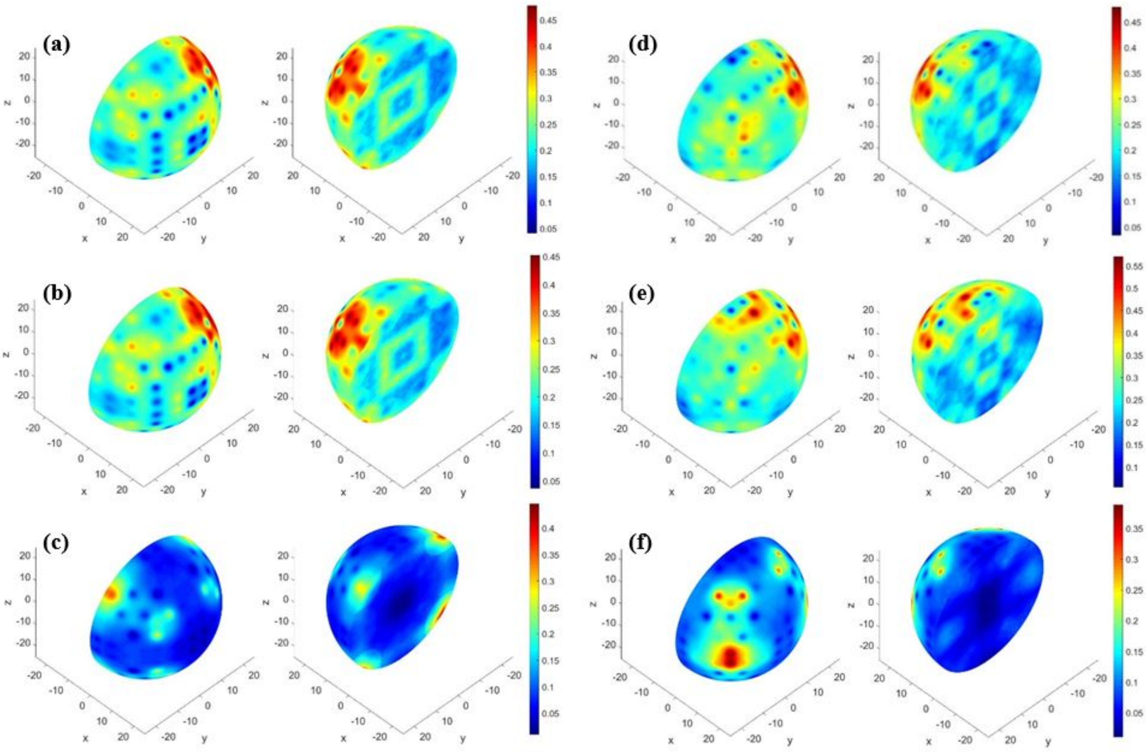

Figure 4.9. Normalized field intensity plots of Au@Ag illuminated with TE (a-c) and TM (d-f) polarized wave: (a,d) at λ=370 nm without AFM tip, (b,e) λ=370 nm and (c,f) λ=490 nm with GaP AFM tip.

Moreover, the dielectric transition of the GaP tip can be observed in Figures 4.9(e,f) in TM-polarized case. It is shown that the field intensity is localized on top of the NP for the 1^{st} peak wavelength, where the imaginary part of the refractive index, k, of GaP is nonzero in Figure 4.9(e). However, as shown in Figure 4.9(f), field localizations move away from apex of the NP and they are distributed over the Ag shell at the 2^{nd} peak wavelength, where the damping effect of GaP tip no longer exists.

It is observed in Figures 4.9(a,b) that TE-polarizedn cases with and without AFM tip for a given wavelength have similar field localizations over Au@Ag NP as there is no y component of the polarization. Similarly, for the Ag@Au NP with and without tip in Figures 4.10(a,b), field is localized both at Ag core and on outer surface of the Au shell. Considering Figure 4.8(b), the major effect on the absorption is observed for the GaP AFM tip with the TM-polarized wave case. Contrary to Au@Ag case, TM-polarized case with GaP AFM tip results in 13% absorption enhancement of Ag@Au at λ=390 nm. This can be attributed to the absorption enhancement of AuNP with AFM tips in TM-polarization cases in Table 4.3. When the driving force dominates over the damping due to Au shell material, absorption enhancement of Ag@Au NP is observed more than 65%. Therefore, Ag@Au NP have also similar behavior of bare

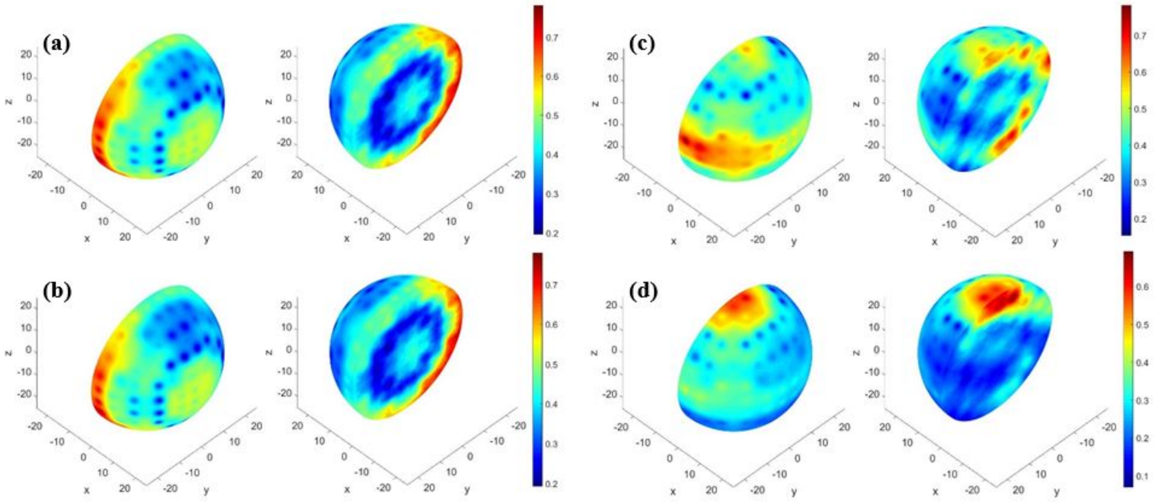

Figure 4.10. Normalized field intensity plots of Ag@Au with TE (a,b) and TM (c,d) polarized wave at λ=380 nm: (a,c) without AFM tip and (b,d) with GaP AFM tip.

AuNP as its Au shell dominates over Ag core material. Moreover, field intensity plots of Ag@Au in Figures 4.10(c),(d) show the effect of AFM tip placement over the NP as the field is collected from the -y side of the outer shell surface to the apex of the NP, which proves the vertical coupling between the tip and the NP.

5. CONCLUSIONS AND FUTURE WORK

5.1. Conclusions

Localized surface plasmon resonance (LSPR) of core-shell nanoparticle pairs are studied for their potential use in localized heating applications and sensing methods. Numerical analyses of core-shell pairs are carried out by using vectorized version of DDA-SI (DDA-SI-v). Optical tunability of the hybrid structures is investigated with dielectric-metal, metal-dielectrici and bimetallic pairs. Moreover, LSPR wavelength and absorption efficiency patterns are studied through various size configurations of the core-shell structure.

When the dielectric core-metal shell cases are examined, the maximum absorption enhancement is observed in SiO_2 core-Au shell which is preferably used as local heat sources in photothermal therapies. Although the maximum absorption enhancement of the SiO_2 core is observed with Au shell case, the greatest redshift of the LSPR wavelength occurs for the Ag shell case. Contrary to SiO_2 core- metal shell cases, it is shown that decreasing the metal shell thickness results in both redshift and blueshift of the LSPR wavelength for GaP core-metal shell pairs. Since there is no general conclusion for the effect of dielectric core on the LSPR wavelength response, each dielectric core material needs to be evaluated individually.

The metal core-dielectric shell cases are also good candidates for optical tuning and field enhancement. It is found that maximum LSPR wavelength shift with maximum absorption enhancement can be obtained with Au core-GaP shell. Moreover, using GaP at shell rather than at core results in both redshift of the LSPR wavelength and enhanced absorption for both Au and Ag metallic core cases. For the SiO_2 shell, maximum absorption efficiency increase is observed in Ag core case. If the shells are dielectric, then NPs redshifts the LSPR wavelengths since they act as a dielectric medium for the metallic cores. Hence, the hybrid structures of metal core-dielectric shell NPs can be utilized both with its enhanced absorption efficiency and with a wide range of optical tunability as compared to the bare metallic NPs.

For the bimetallic NPs, more than one plasmon mode can be observed due to the hybrid structure of the core-shell NPs. Plasmon response of Ag core-Au shell case is observed with blue-shift and red-shift in the LSPR wavelength for the first and secondary peaks, respectively. However, the plasmon response of Au core-Ag shell case is affected by the shielding of the Ag shell that leads to the greatest absorption only at the extraordinary mode.

Parametric size comparisons showed that increasing volumetric filling ratio, f_r, of core gives rise to maximum absorption enhancement over 91% for Ag@Au core-shell NP. However, increase in f_r of the core in Au@Ag case results in damping of absorption efficiency values by 135%. This huge differences in absorption can be utilized in the characterization or sensing of the core-shell NPs and core/shell formation applications. Moreover, the changes in the refractive index of the dielectric medium is compared for the absorption efficiency values and LSPR responses of the fixed core cases for both Ag@Au and Au@Ag core-shell NPs. It is shown that interaction between the metallic shell surface and dielectric medium leads to absorption enhancement as the refractive index of the medium increases. Maximum absorption enhancement is found for Ag@Au shell case while greater redshift in LSPR wavelength occurs in Au@Ag shell case. It is shown that there is a trade-off between the absorption enhancement and red-shift in the LSPR response. Therefore, selected core-shell NPs can be effectively used in biosensing and material detection by comparing their LSPR and absorption responses.

Further analyses are performed on the spectral absorption behavior of the selected core-shell (Ag@Au, Au@Ag) and bare metallic (Ag and Au) NPs that are placed under the dielectric AFM tip. The considered AFM materials are GaP and Si, due to their changing dielectric behavior at increasing wavelengths. The results showed that AFM tip introduction can both damp and enhance the absorption of the NPs. A detailed analysis is carried out on the AFM tip material, and it was found that the absorption enhancement with GaP AFM tip was greater. The TE-polarized incident wave with and without using the AFM tip is compared, and the introduction of tip was found to damp the absorption efficiency values of all NP types. It is observed that polarization direction transverse to tip-NP axis prevents vertical coupling of NP and AFM tip. For TM-polarized cases, bare Ag and Au@Ag core-shell NPs are observed to have multi-peak response, where the absorption enhancement occurs at the 2^{nd} LSPR wavelength, λ=490 nm. It is found that the damping of the absorption at the 1^{st} LSPR wavelength, λ=370 nm, results from the nonzero imaginary part of the refractive index of the tip material. However, the damping under TM-polarized incident light in presence of AFM tip is not observed for bare Au and Ag@Au core-shell NPs since the increasing driving force with the introduction of AFM tip can dominate over the damping factor of the NPs. Therefore, our study shows consistent results found in literature based on the damping effect. Moreover, extended spectral absorption analyses show that damping characteristic of the AFM tip use can alter for different shell materials.

5.2. Future Work

The future work plans for this study can be made both with additional developments in the DDA-SI package and with further design problems. The method used in this study was optimized with vectorization, DDA-SI-v, by Talebi *et al.* [33] for faster computation time. With the same purpose, the third version, DDA-SI-z, is developed by Rostampour-Fathi *et al.* [34] with the preconditioning of the iterative solver. Considering the large structures requiring more number of dipoles for adequate representation, improvements in solver methods can be studied in detail. Moreover, the use of DDA-SI package can also be simplified with a more user-friendly environment. The proposed simplifications are as follows;

- Shape generation process can be automated with predefined functions to be used in the main code. Loading the variables instead of defining in the code can improve the performance of the compiler.
- Number of dipole optimization can be adapted with constant lattice spacing criterion when the problem consists of different shapes such as the spherical NP and AFM considered in this study.

- Other executable programs can be used for a specific design problems to be compiled in MATLAB environment.

There are also some application based problems as follows;

- Local heating of an array of core-shell NPs in presence of AFM tip for nanomanufacturing purposes. Hence, absorption and the LSPR response of the central NP can be analyzed with the the tip position and alternating core-shell NP type and size located around the considered NP.
- Changing the medium refractive index similar to visceral organs can be utilized in tumor treatment applications to simulate the photothermal heating of the NPs under the effect absorption enhancement of AFM tip. With this purpose, multilayered core-shell structure can be designed and analyzed with more real cases such as enzyme and drug coating on the second shell of the NPs.
- Considering sensing applications, scattering intensities can be studied by changing the dielectric medium and substrate material. Constructing the spectral absorption/scattering efficiency data for core-shell NP types can be utilized further with the inverse problem solutions for the detection methods.

REFERENCES

1. Siegel, R. W., E. Hu, M. Roco, D. M. Cox and H. Goronkin, “Nanostructure Science and Technology. A Worldwide Study”, *NSTC*, p. 363, 1999.

2. Whitesides, G. M., “Nanoscience, Nanotechnology, and Chemistry”, *Small*, Vol. 1, No. 2, pp. 172–179, 2005.

3. He, G. S., M. Liu, J. W. Haus, M. T. Swihart and P. N. Prasad, “Strong Stimulated Mie Scattering from Plasmonic CuS Nanocrystals in Toluene or Pentane”, *IEEE Journal of Selected Topics in Quantum Electronics*, 2017.

4. Luo, L., R. Shu and A. Wu, “Nanomaterial-Based Cancer Immunotherapy”, *Journal of Materials Chemistry B*, Vol. 5, No. 28, pp. 5517–5531, 2017.

5. Wilson, R., “The Use of Gold Nanoparticles in Diagnostics and Detection”, *Chemical Society Reviews*, Vol. 37, No. 9, p. 2028, 2008.

6. Howell, J. R., R. Siegel and M. P. Mengüç, *Thermal Radiation Heat Transfer*, CRC Press, New York, 5 edn., 2010.

7. Xu, J., K. Läuger, R. Möller, K. Dransfeld and I. H. Wilson, “Heat Transfer Between Two Metallic Surfaces at Small Distances”, *Journal of Applied Physics*, Vol. 76, No. 11, pp. 7209–7216, 1994.

8. Maier, S. A., *Plasmonics: Fundamentals and Applications*, Springer US, 2007.

9. Huda, G. M., E. U. Donev, M. P. Mengüç and J. T. Hastings, “Effects of a Silicon Probe on Gold Nanoparticles on Glass Under Evanescent Illumination”, *Optics Express*, Vol. 19, No. 13, p. 12679, 2011.

10. Taylor, J., A. Huefner, L. Li, J. Wingfield and S. Mahajan, “Nanoparticles and

Intracellular Applications of Surface-Enhanced Raman Spectroscopy", *The Royal Society of Chemistry*, Vol. 141, No. 17, pp. 5037–5055, 2016.

11. Joulain, K., P. Ben-Abdallah, P. O. Chapuis, Y. De Wilde, A. Babuty and C. Henkel, "Strong Tip-Sample Coupling in Thermal Radiation Scanning Tunneling Microscopy", Vol. 136, pp. 1–15, 2014.

12. McCarthy, B., Y. Zhao, R. Grover and D. Sarid, "Enhanced Raman Scattering for Temperature Measurement of a Laser-Heated Atomic Force Microscope Tip", *Applied Physics Letters*, Vol. 86, No. 11, pp. 1–3, 2005.

13. Lal, S., S. E. Clare and N. J. Halas, "Photothermal Therapy : Impending Clinical Impact", *Accounts of Chemical Research*, Vol. 41, No. 12, pp. 1842–1851, 2008.

14. Pattani, V. P. and J. W. Tunnell, "Nanoparticle-Mediated Photothermal Therapy: A Comparative Study of Heating for Different Particle Types", *Lasers in Surgery and Medicine*, Vol. 44, No. 8, pp. 675–684, 2012.

15. Strobbia, P., E. Languirand and B. M. Cullum, "Recent Advances in Plasmonic Nanostructures for Sensing: A Review", *Optical Engineering*, Vol. 54, No. 10, p. 100902, 2015.

16. Loke, V. L. Y. and M. P. Mengüç, "Surface Waves and Atomic Force Microscope Probe-Particle Near-Field Coupling : Discrete Dipole Approximation with Surface Interaction", *Journal of the Optical Society of America A*, Vol. 27, No. 10, pp. 2293–303, 2010.

17. Hawes, E. A., J. T. Hastings, C. Crofcheck and M. P. Mengüç, "Spatially Selective Melting and Evaporation of Nanosized Gold Particles.", *Optics letters*, Vol. 33, No. 12, pp. 1383–1385, 2008.

18. Honda, M., Y. Saito, N. I. Smith, K. Fujita and S. Kawata, "Nanoscale Heating of Laser Irradiated Single Gold Nanoparticles in Liquid", *Optics Express*, Vol. 19,

No. 13, p. 12375, 2011.

19. Rodríguez-Santana, P., A. I. Jiménez-Abizanda, A. Hernández-Creus and F. Jiménez-Moreno, "Synthesis and Physical Characterization of Ag Nanoparticles and Their Interaction with Fe", *Journal of Luminescence*, Vol. 190, pp. 207–214, 2017.

20. Lee, Y. H., H. Chen, Q. H. Xu and J. Wang, "Refractive Index Sensitivities of Noble Metal Nanocrystals: The Effects of multipolar Plasmon Resonances and the Metal Type", *Journal of Physical Chemistry C*, Vol. 115, pp. 7997–8004, 2011.

21. Zhu, J., X. Li, J. jun Li and J. wu Zhao, "Enlarge the Biologic Coating-Induced Absorbance Enhancement of Au-Ag Bimetallic Nanoshells by Tuning the Metal Composition", *Spectrochimica Acta Part A: Molecular and Biomolecular Spectroscopy*, Vol. 189, pp. 571 – 577, 2018.

22. Zhu, J., J.-j. Li and J.-w. Zhao, "The Study of Surface Plasmon Resonance in Au-Ag-Au Three-Layered Bimetallic Nanoshell : The Effect of Separate Ag Layer", *Plasmonics*, Vol. 9, pp. 435–441, 2014.

23. Sharma, R., S. Roopak, P. Alok and R. P. Sharma, "Study of Surface Plasmon Resonances of Core-Shell Nanosphere : A Comparison between Numerical and Analytical Approach", *Plasmonics*, Vol. 12, pp. 977–86, 2017.

24. Chen, H., L. Shao, Y. C. Man, C. Zhao, J. Wang and B. Yang, "Fano resonance in (Gold Core)-(Dielectric Shell) Nanostructures without Symmetry Breaking", *Small*, Vol. 8, No. 10, pp. 1503–1509, 2012.

25. Xu, X.-b., M. Liu, J.-s. Luo, Y.-y. Wang, Z. Yi, X.-b. Li, Y.-g. Yi and Y.-j. Tang, "Nanoscale Energy Confinement and Hybridization of Surface Plasmons Based on Skin Depth in Au / Ag Core-Shell Nanostructures", *Plasmonics*, Vol. 10, pp. 797–808, 2015.

26. Zhang, C., B.-q. Chen, Z.-y. Li and Y.-g. Chen, “Surface Plasmon Resonance in Bimetallic Core − Shell Nanoparticles”, *The Journal of Physical Chemistry C*, Vol. 119, pp. 16836–16845, 2015.

27. Hubenthal, F., N. Borg and F. Träger, “Optical Properties and Ultrafast Electron Dynamics in Gold-Silver Alloy and Core-Shell Nanoparticles”, *Applied Physics B: Lasers and Optics*, Vol. 93, No. 1, pp. 39–45, 2008.

28. Avşar, D., H. Ertürk and M. P. Mengüç, “Plasmonic Responses of Metallic/Dielectric Core-Shell Nanoparticles on a Dielectric Substrate”, *Materials Research Express*, Vol. 6, No. 6, p. 065006, 2019.

29. Basu, S., Z. M. Zhang and C. J. Fu, “Review of Near-Field Thermal Radiation and Its Application to Energy Conversion”, *International Journal of Energy Research*, Vol. 33, No. 13, pp. 1203–1232, 2009.

30. Hawes, E. A., J. T. Hastings, C. Crofcheck and M. P. Mengüç, “Spectrally Selective Heating of Nanosized Particles by Surface Plasmon Resonance”, *Journal of Quantitative Spectroscopy and Radiative Transfer*, Vol. 104, No. 2, pp. 199–207, 2007.

31. Rechberger, W., A. Hohenau, A. Leitner, J. R. Krenn, B. Lamprecht and F. R. Aussenegg, “Optical Properties of Two Interacting Gold Nanoparticles”, *Optics Communications*, Vol. 220, pp. 137–141, 2003.

32. Talebi Moghaddam, S., D. Avşar, H. Ertürk and M. P. Mengüç, “Effect of the Probe Location on the Absorption by an Array of Gold Nano-Particles on a Dielectric Surface”, *Journal of Quantitative Spectroscopy and Radiative Transfer*, Vol. 197, pp. 106–113, 2017.

33. Talebi Moghaddam, S., H. Ertürk and M. P. Mengüç, “Enhancing Local Absorption within a Gold Nano-Sphere on a Dielectric Surface Under an AFM Probe”, *Journal of Quantitative Spectroscopy and Radiative Transfer*, Vol. 178, pp. 124–133, 2016.

34. Rostampour Fathi, Z., M. P. Mengüç and H. Ertürk, “Plasmon Coupling Between Complex Gold Nanostructures and a Dielectric Substrate”, *Applied Optics*, Vol. 57, No. 30, pp. 8954–8963, 2018.

35. Huda, G. M. and J. Todd Hastings, “Absorption Modulation of Plasmon Resonant Nanoparticles in the Presence of an AFM Tip”, *IEEE Journal on Selected Topics in Quantum Electronics*, Vol. 19, No. 3, p. 4602306, 2013.

36. Zhou, H. S., I. Honma, H. Komiyama and J. W. Haus, “Controlled Synthesis and Quantum-Size Effect in Gold-Coated Nanoparticles”, *Physical Review B*, Vol. 50, No. 16, pp. 12052–12056, 1994.

37. Hirsch, L. R., R. J. Stafford, J. A. Bankson, S. R. Sershen, B. Rivera, R. E. Price, J. D. Hazle, N. J. Halas and J. L. West, “Nanoshell-Mediated Near-Infrared Thermal Therapy of Tumors Under Magnetic Resonance Guidance”, *Proceedings of the National Academy of Sciences*, Vol. 100, No. 23, pp. 13549–13554, 2003.

38. Park, H. S., J. Y. Kim, M. W. Kim, Y. H. Cho and M. K. Kwon, “Localized Surface Plasmon-Enhanced Emission from Red Phosphor with Au-SiO_2 Nanoparticles”, *Materials Letters*, Vol. 205, pp. 145–149, 2017.

39. Yu, P., Y. Yao, J. Wu, X. Niu, A. L. Rogach and Z. Wang, “Effects of Plasmonic Metal Core-Dielectric Shell Nanoparticles on the Broadband Light Absorption Enhancement in Thin Film Solar Cells”, *Scientific Reports*, Vol. 7, No. 1, pp. 1–10, 2017.

40. Sershen, S. R., S. L. Westcott, N. J. Halas and J. L. West, “Independent Optically Addressable Nanoparticle-Polymer Optomechanical Composites”, *Applied Physics Letters*, Vol. 80, No. 24, pp. 4609–4611, 2002.

41. Sathiyamoorthy, K. and M. C. Kolios, “Numerical Investigation of Plasmonic Properties of Gold Nanoshells”, *Proceedings of SPIE*, Vol. 9340, p. 93400V, 2015.

42. Oldenburg, S. J., R. D. Averitt, S. L. Westcott and N. J. Halas, “Nanoengineering of Optical Resonances”, *Chemical Physics Letters*, Vol. 288, No. 2-4, pp. 243–7, 1998.

43. Prodan, E., C. Radloff, N. J. Halas and P. Nordlander, “A Hybridization Model for the Plasmon Response of Complex Nanostructures”, *Science*, Vol. 302, No. 5644, pp. 419–422, 2003.

44. Wang, Y., W. Qian, Y. Tan and S. Ding, “A Label-Free Biosensor Based on Gold Nanoshell Monolayers for Monitoring Biomolecular Interactions in Diluted Whole Blood”, *Biosensors and Bioelectronics*, Vol. 23, No. 7, pp. 1166–1170, 2008.

45. Riva, E. R., A. Desii, E. Sinibaldi, G. Ciofani, V. Piazza, B. Mazzolai and V. Mattoli, “Gold nanoshell/polysaccharide nanofilm for controlled laser-assisted tissue thermal ablation”, *ACS Nano*, Vol. 8, No. 6, pp. 5552–5563, 2014.

46. Navas, M. P. and R. K. Soni, “Laser-Generated Bimetallic Ag-Au and Ag-Cu Core-Shell Nanoparticles for Refractive Index Sensing”, *Plasmonics*, Vol. 10, No. 3, pp. 681–690, 2015.

47. Huda, G. M., M. P. Mengüç and J. T. Hastings, “Absorption Suppression of Silver Nanoparticles in the Presence of an AFM Tip: A Harmonic Oscillator Model”, *AIP Conference Proceedings*, Vol. 1475, No. August, pp. 134–136, 2012.

48. Albella, P., R. A. De La Osa, F. Moreno and S. A. Maier, “Electric and Magnetic Field Enhancement with Ultralow Heat Radiation Dielectric Nanoantennas: Considerations for Surface-Enhanced Spectroscopies”, *ACS Photonics*, Vol. 1, No. 6, pp. 524–529, 2014.

49. Friebel, M. and M. Meinke, “Model Function to Calculate the Refractive Index of Native Hemoglobin in the Wavelength Range of 250-1100 nm Dependent on Concentration”, *Applied Optics*, Vol. 45, No. 12, p. 2838, 2006.

50. Adair, G. S. and M. E. Robinson, “The Specific Refraction Increments of Serum-Albumin and Serum-Globulin”, *Biochemical Journal*, Vol. 24, No. 4, pp. 993–1011, 1930.

51. Francoeur, M., *Near-field Radiative Transfer: Thermal Radiation, Thermophotovoltaic Power Generation and Optical Characterization*, Ph.D. Thesis, University of Kentucky, 2010.

52. Francoeur, M. and M. P. Mengüç, “Role of Fluctuational Electrodynamics in Near-Field Radiative Heat Transfer”, *Journal of Quantitative Spectroscopy and Radiative Transfer*, Vol. 109, No. 2, pp. 280 – 293, 2008, the Fifth International Symposium on Radiative Transfer.

53. Rohlf, J. W., *Modern Physics from A to Z^0*, Wiley-VCH, 1994.

54. Narayanaswamy, A. and G. Chen, “Dyadic Green’s Functions and Electromagnetic Local Density of States”, *Journal of Quantitative Spectroscopy and Radiative Transfer*, Vol. 111, No. 12, pp. 1877 – 1884, 2010.

55. Joulain, K., R. Carminati, J.-P. Mulet and J.-J. Greffet, “Definition and Measurement of the Local Density of Electromagnetic States Close to an Interface”, *Phys. Rev. B*, Vol. 68, p. 245405, 2003.

56. Zhang, Z. M., *Nano/Microscale Heat Transfer*, McGraw-Hill, 2007.

57. Boriskina, S. V., J. K. Tong, Y. Huang, J. Zhou, V. Chiloyan and G. Chen, “Enhancement and Tunability of Near-Field Radiative Heat Transfer Mediated by Surface Plasmon Polaritons in Thin Plasmonic Films”, *Photonics*, Vol. 2, No. 2, pp. 659–683, 2015.

58. Purcell, E. M. and C. R. Pennypacker, “ Scattering and Absorption of Light by Nonspherical Dielectric Grains”, *The Astrophysical Journal*, Vol. 186, No. 2, pp. 705–714, 1973.

59. Draine, B. T., “The Discrete-Dipole Approximation and Its Application to Interstellar Graphite Grains”, *The Astrophysical Journal*, Vol. 333, p. 848, 1988.

60. Draine, B. T. and P. J. Flatau, “Discrete-Dipole Approximation for Scattering Calculations”, *Journal of Optical Society of America A*, Vol. 11, No. 4, pp. 1491–1499, 1994.

61. Yurkin, M. A. and A. G. Hoekstra, “The Discrete-Dipole-Approximation Code ADDA: Capabilities and Known Limitations”, *Journal of Quantitative Spectroscopy and Radiative Transfer*, Vol. 112, No. 13, pp. 2234–2247, 2011.

62. Loke, V. L. Y., M. P. Mengüç and T. A. Nieminen, “Discrete-Dipole Approximation with Surface Interaction: Computational Toolbox for MATLAB”, *Journal of Quantitative Spectroscopy and Radiative Transfer*, Vol. 112, No. 11, pp. 1711–1725, 2011.

63. Short, M. R., J. M. Geffrin, R. Vaillon, H. Tortel, B. Lacroix and M. Francoeur, “Evanescent Wave Scattering by Particles on a Surface: Validation of the Discrete Dipole Approximation with Surface Interaction Against Microwave Analog Experiments”, *Journal of Quantitative Spectroscopy and Radiative Transfer*, Vol. 146, pp. 452–458, 2014.

64. Loke, V. L., G. M. Huda, E. U. Donev, V. Schmidt, J. T. Hastings, M. P. Mengüç and T. Wriedt, “Comparison Between Discrete Dipole Approximation and Other Modelling Methods for the Plasmonic Response of Gold Nanospheres”, *Applied Physics B: Lasers and Optics*, Vol. 115, No. 2, pp. 237–246, 2014.

65. Cambiasso, J., G. Grinblat, Y. Li, A. Rakovich, E. Corte and S. A. Maier, “Bridging the Gap between Dielectric Nanophotonics and the Visible Regime with Effectively Lossless Gallium Phosphide Antennas”, *ACS Nano Letters*, Vol. 17, No. 2, pp. 1219–1225, 2017.

66. Johnson, P. B. and R. W. Christy, “Optical Constants of the Noble Metals”, *Phys-*

ical Review B, Vol. 6, No. 12, pp. 4370–4379, 1972.

67. Aspnes, D. E. and A. A. Studna, "Dielectric Functions and Optical Parameters of Si, Ge, GaP, GaAs, GaSb, InP, InAs, and InSb from 1.5 to 6.0 eV", *Phys. Rev. B*, Vol. 27, pp. 985–1009, 1983.

68. Palik, E. D., *Handbook of Optical Constants of Solids*, Academic Press, 1998.

APPENDIX A: OPTICAL DATA OF THE NANOPARTICLES

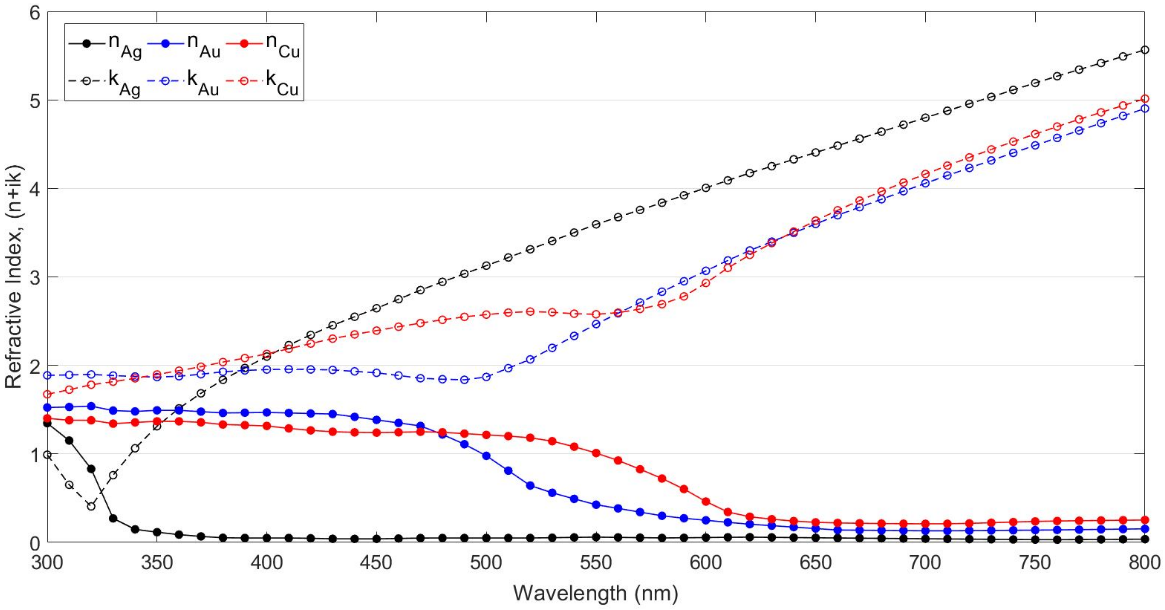

Figure A.1. Spectral refractive indices of silver, gold, and copper.

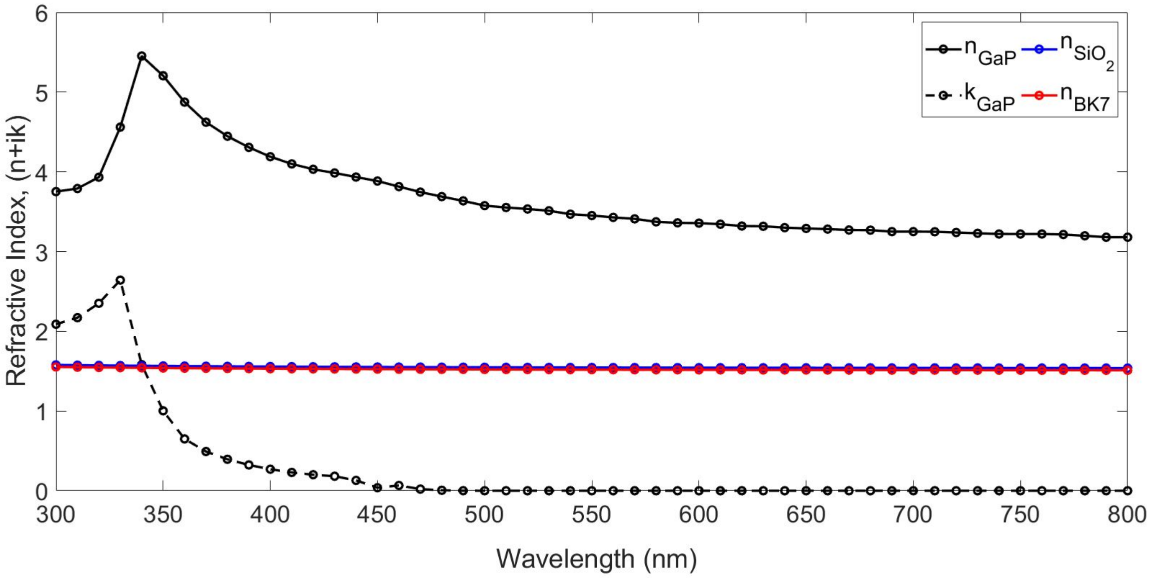

Figure A.2. Spectral refractive indices of Gallium phosphide (GaP), Silicon dioxide (SiO_2), and Borosilicate glass (BK7).

APPENDIX B: FREE SPACE COMPARISONS OF METAL NANOPARTICLES

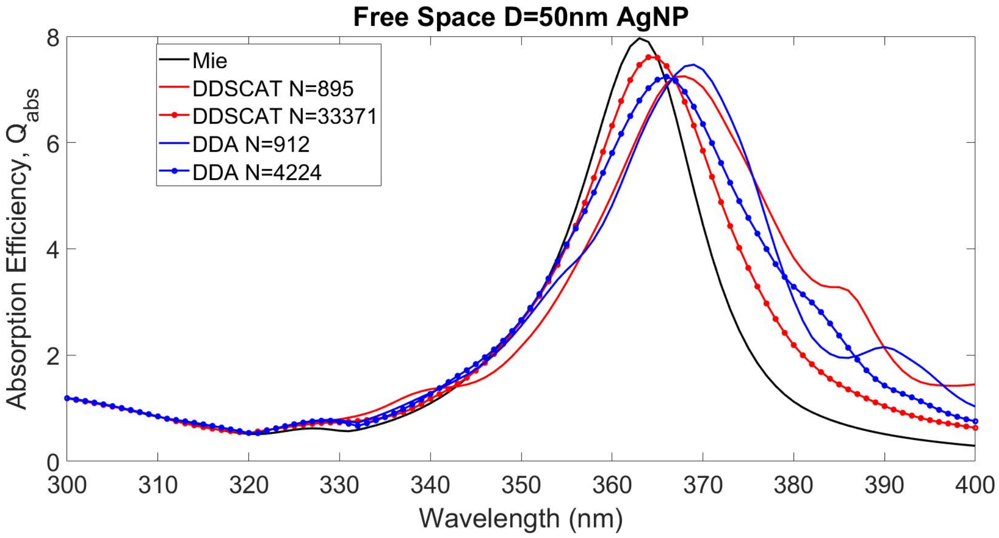

Figure B.1. Absorption efficiency comparisons of single silver nanoparticle in free space approximated by different number of dipoles, N, using DDSCAT and DDA.

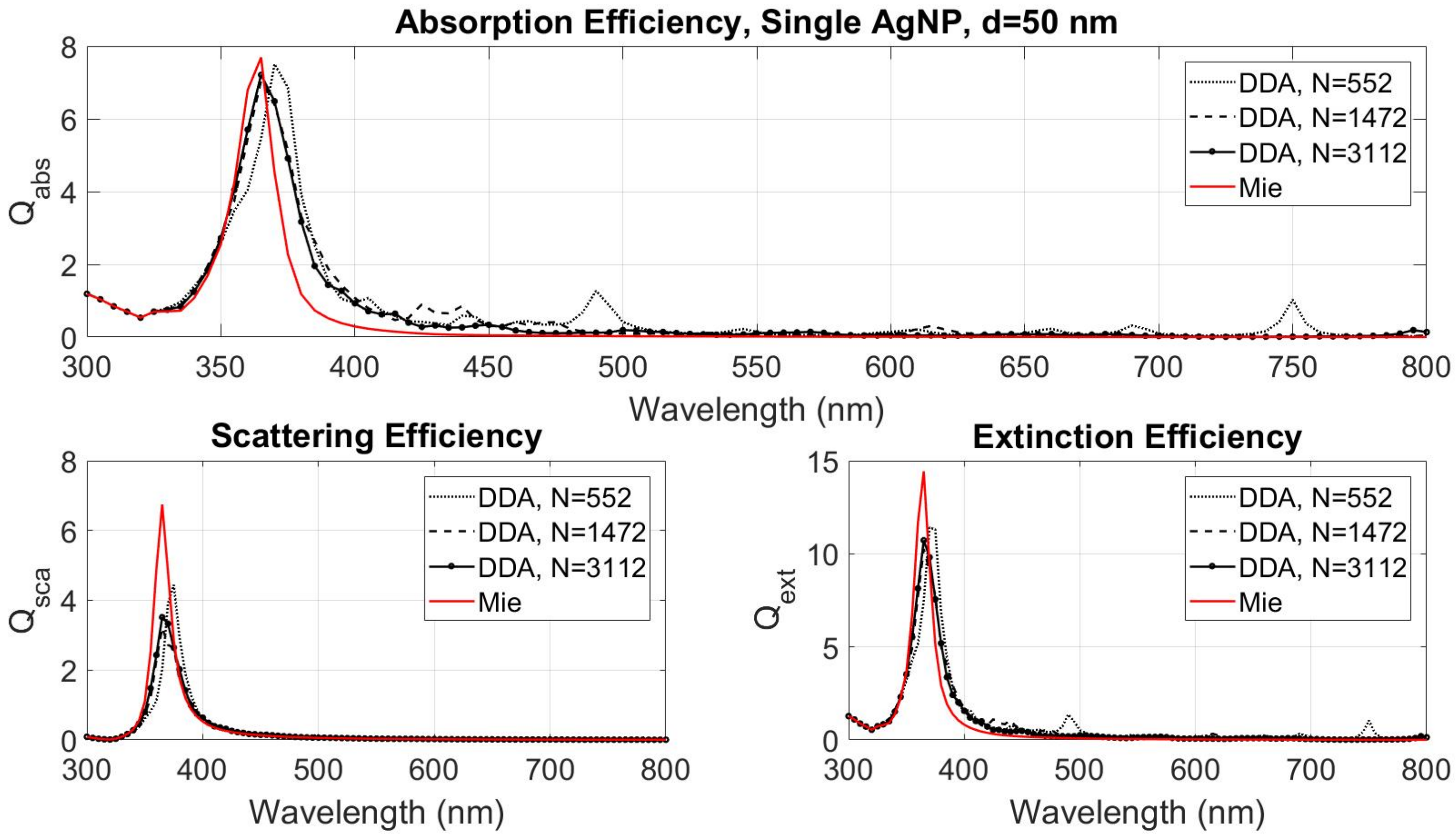

Figure B.2. Free space comparison of DDA method with Mie theory for spectral absorption, scattering, and extinction efficiency values of silver nanoparticle, AgNP, in 50 nm diameter.

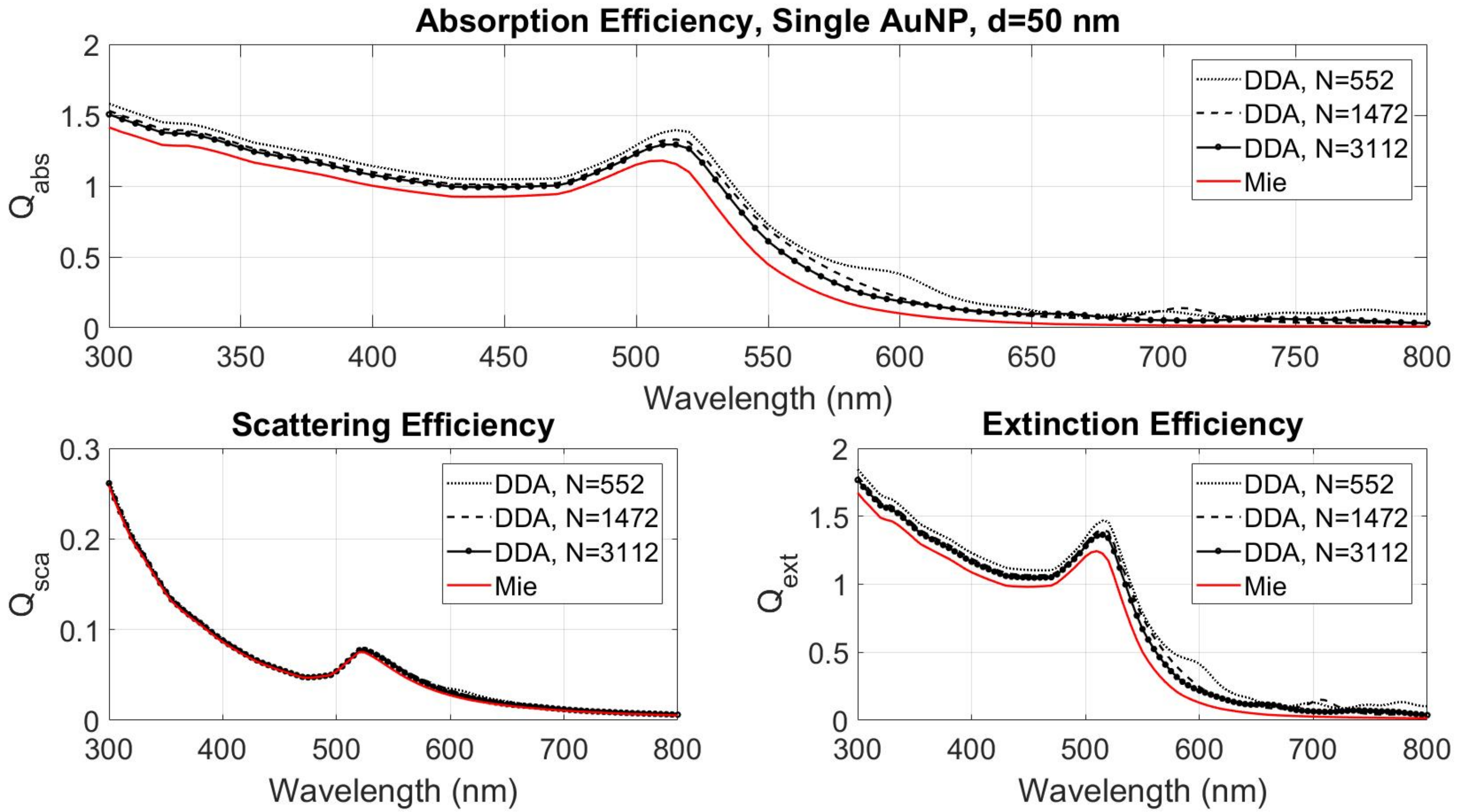

Figure B.3. Free space comparison of DDA method with Mie theory for spectral absorption, scattering, and extinction efficiency values of gold nanoparticle, AuNP, in 50 nm diameter.

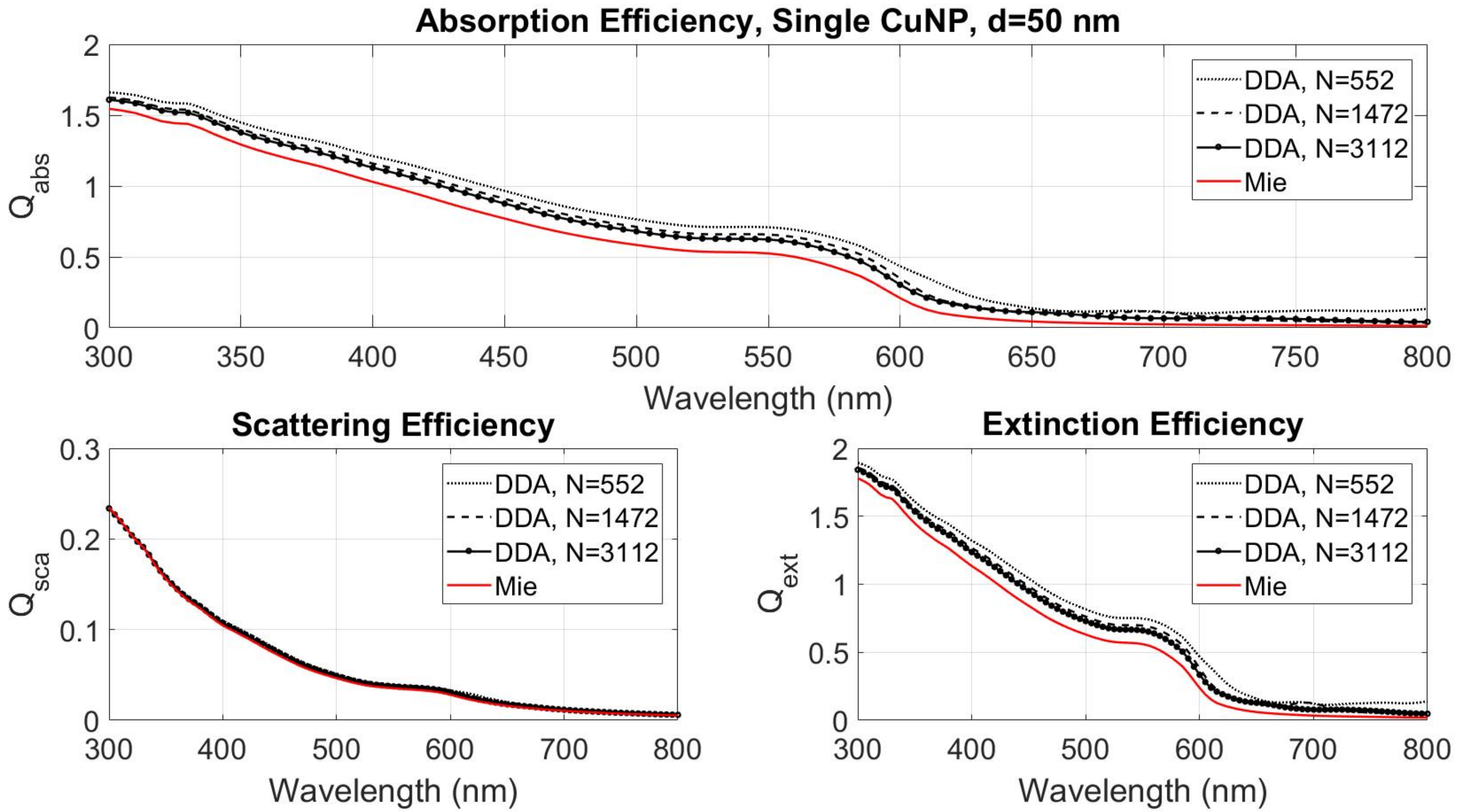

Figure B.4. Free space comparison of DDA method with Mie theory for spectral absorption, scattering, and extinction efficiency values of copper nanoparticle, CuNP, in 50 nm diameter.

APPENDIX C: ADDITIONAL PLOTS: FNP

C.1. Dielectric Core - Metal Shell

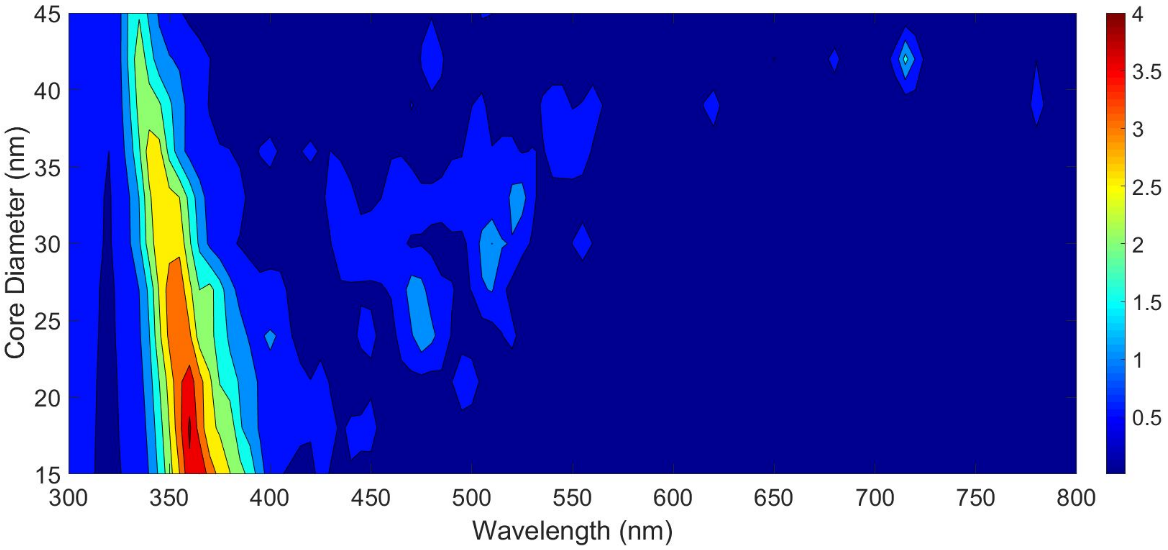

Figure C.1. GaP core with Ag shell with D_s=50 nm: Contour plot of absorption efficiency as a function of wavelength for FNP size.

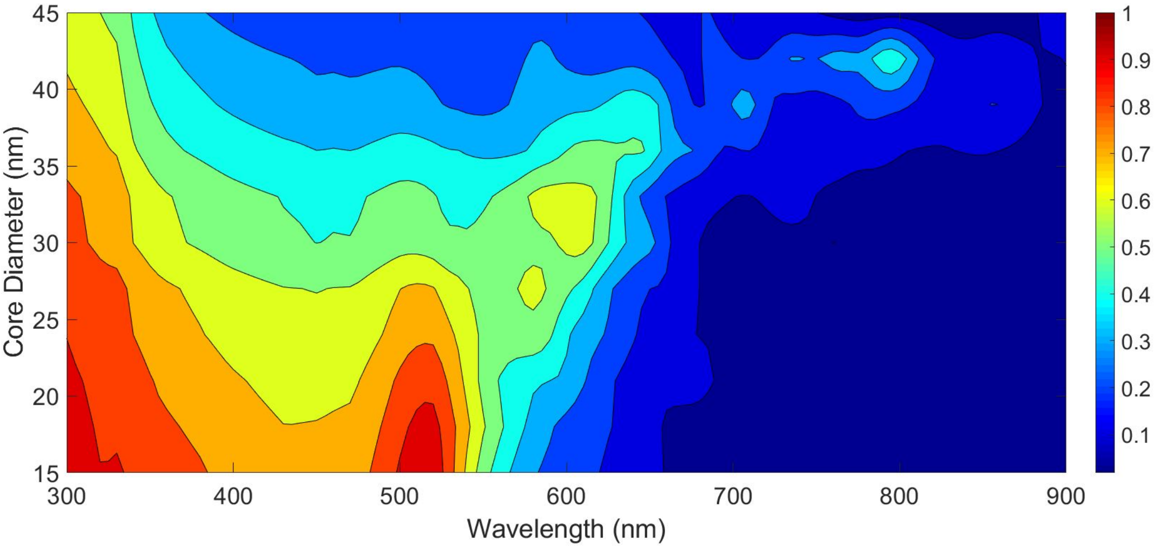

Figure C.2. GaP core with Au shell with D_s=50 nm: Contour plot of absorption efficiency as a function of wavelength for FNP size.

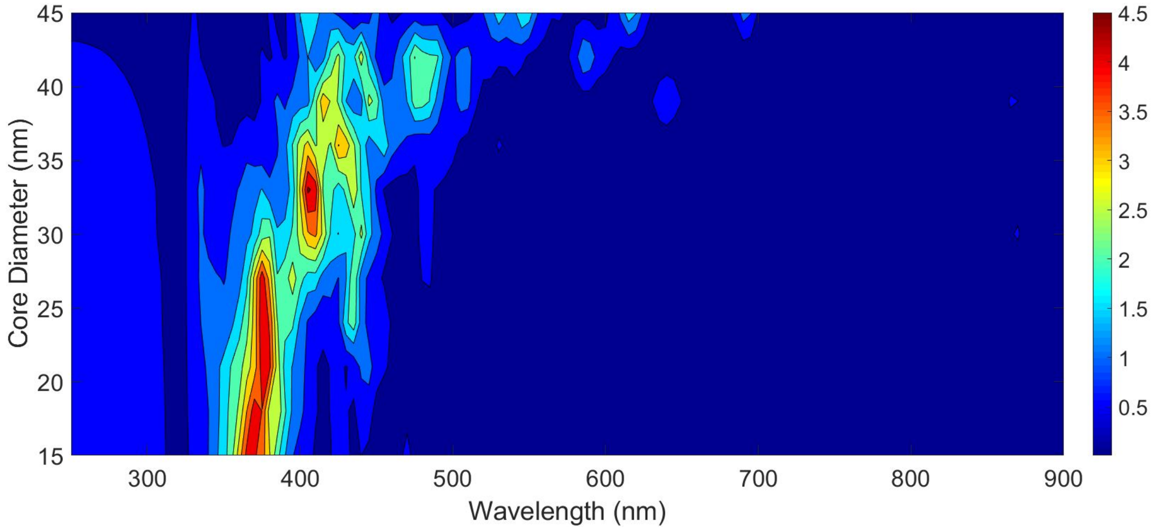

Figure C.3. SiO_2 core with Ag shell with D_s=50 nm: Contour plot of absorption efficiency as a function of wavelength for FNP size.

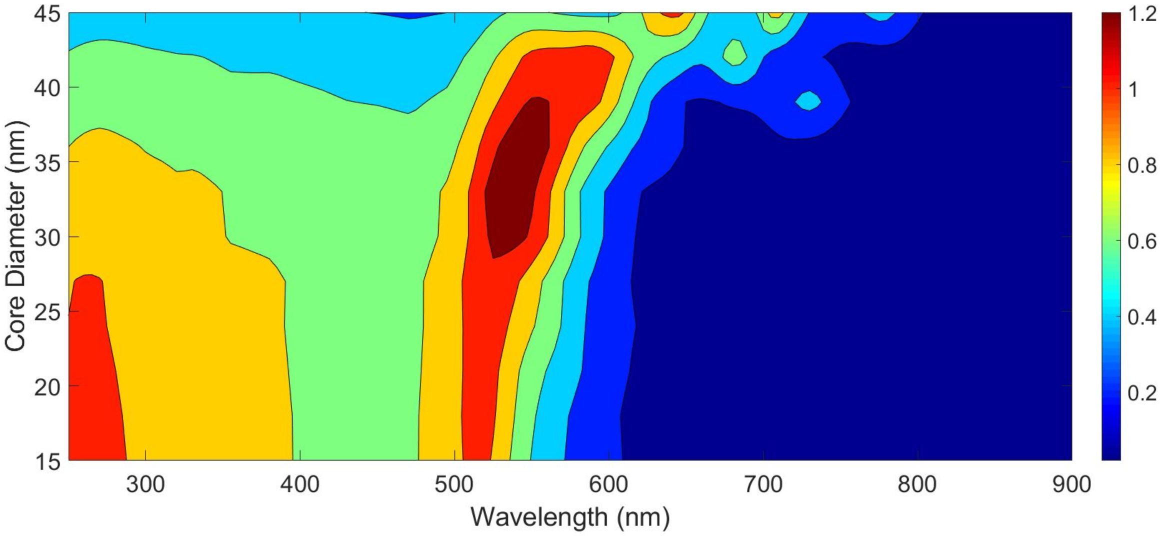

Figure C.4. SiO_2 core with Au shell with D_s=50 nm: Contour plot of absorption efficiency as a function of wavelength for FNP size.

C.2. Metal Core - Dielectric Shell

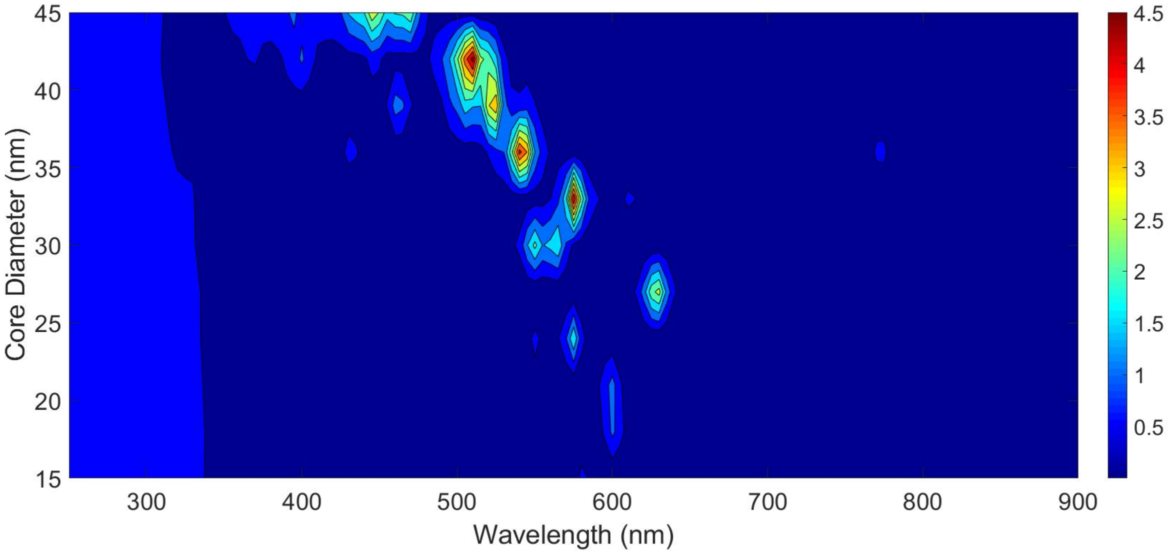

Figure C.5. Ag core with GaP shell with D_s=50 nm: Contour plot of absorption efficiency as a function of wavelength for FNP size.

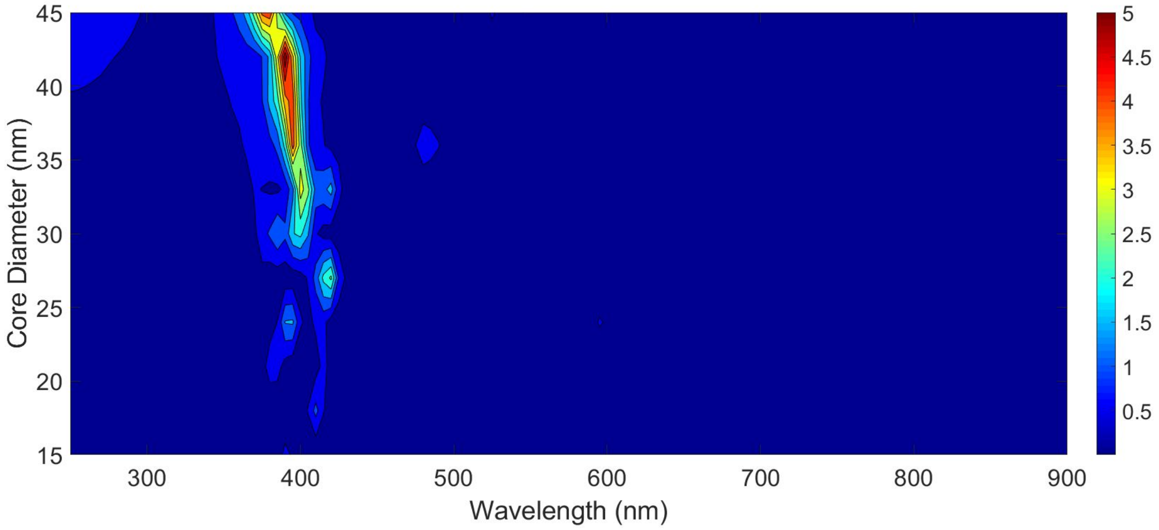

Figure C.6. Ag core with SiO_2 shell with D_s=50 nm: Contour plot of absorption efficiency as a function of wavelength for FNP size.

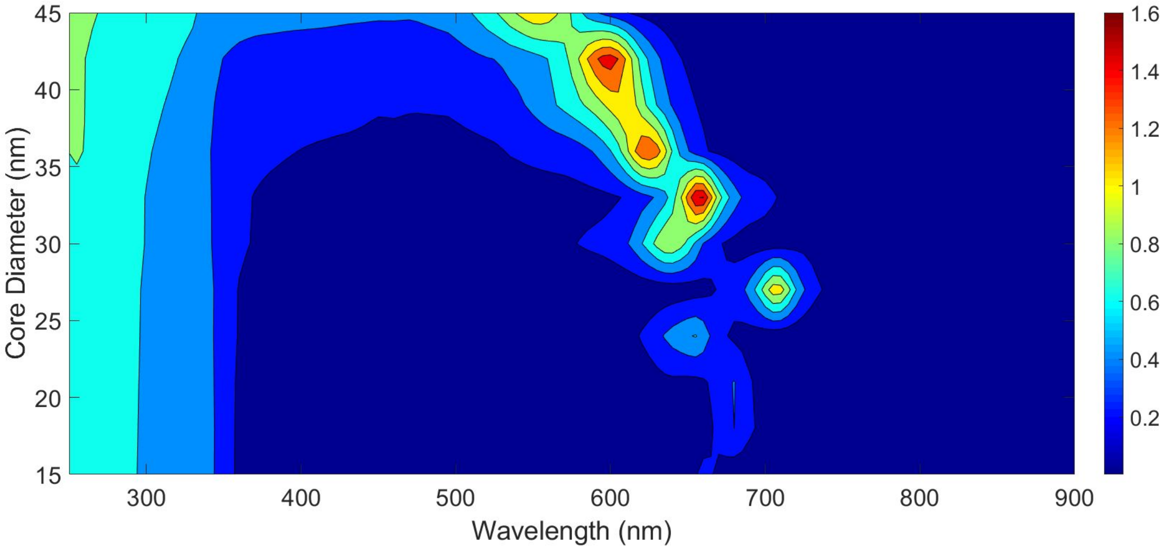

Figure C.7. Au core with GaP shell with D_s=50 nm: Contour plot of absorption efficiency as a function of wavelength for FNP size.

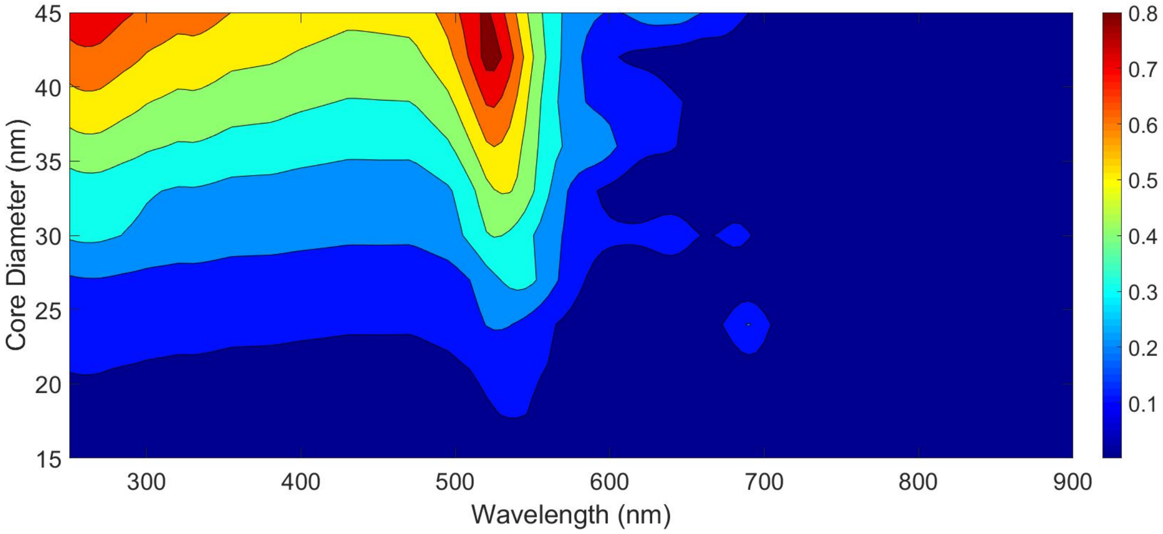

Figure C.8. Au core with SiO_2 shell with D_s=50 nm: Contour plot of absorption efficiency as a function of wavelength for FNP size.

APPENDIX D: FIXED CORE CASES WITH AFM AND TM-WAVE

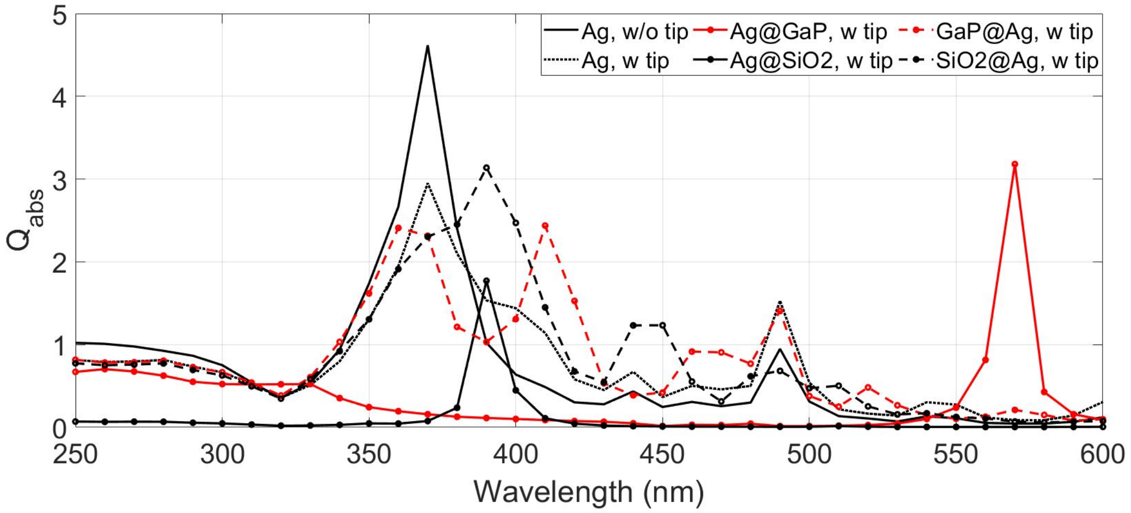

Figure D.1. Spectral Q_{abs} values for single AgNP, and dielectric pairs with both Ag core and Ag shell under Si AFM tip at coordinate (0, 0, 52) nm. Fixed size with D_c=20 nm, D_s=50 nm for core-shell NPs.

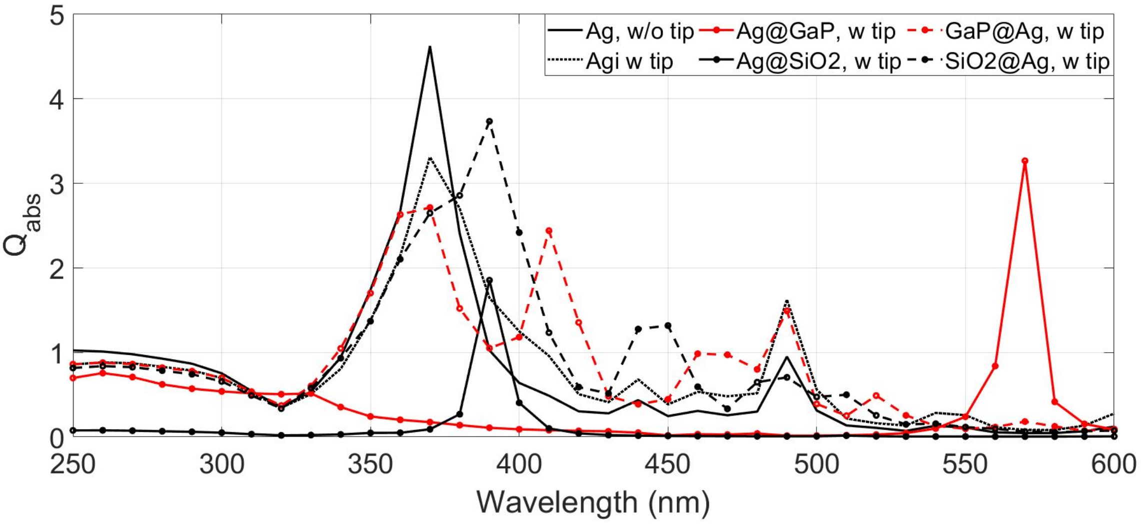

Figure D.2. Spectral Q_{abs} values for single AgNP, and dielectric pairs with both Ag core and Ag shell under GaP AFM tip at coordinate (0, 0, 52) nm. Fixed size with D_c=20 nm, D_s=50 nm for core-shell NPs.

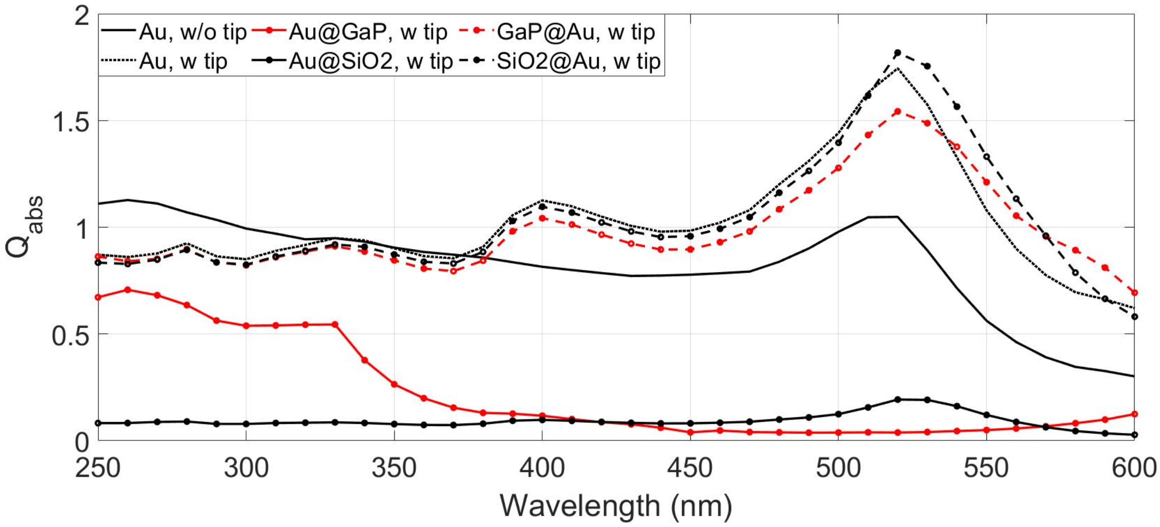

Figure D.3. Spectral Q_{abs} values for single AuNP, and dielectric pairs with both Au core and Au shell under Si AFM tip at coordinate (0, 0, 52) nm. Fixed size with D_c=20 nm, D_s=50 nm for core-shell NPs.

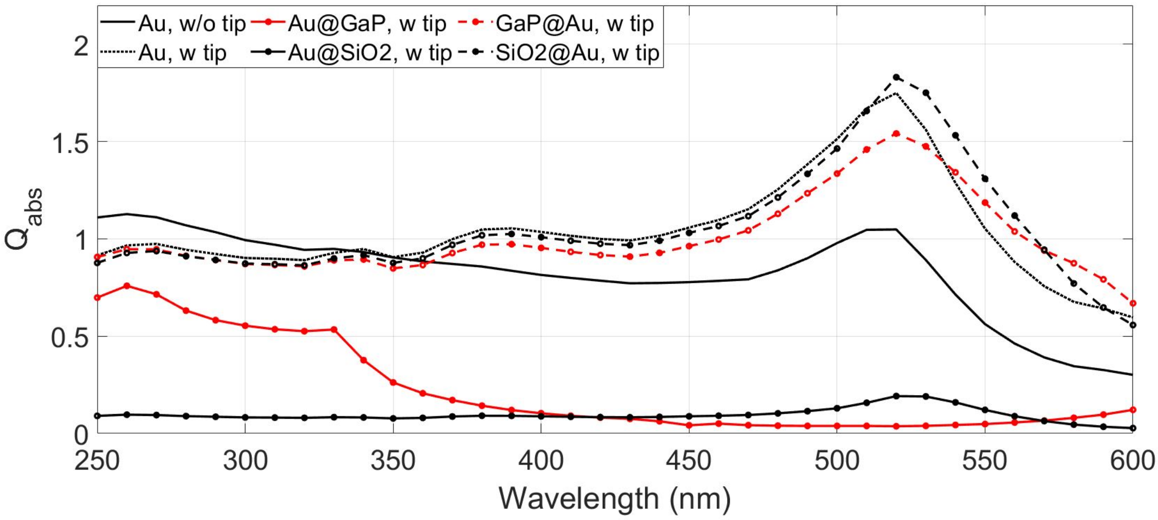

Figure D.4. Spectral Q_{abs} values for single AuNP, and dielectric pairs with both Au core and Au shell under GaP AFM tip at coordinate (0, 0, 52) nm. Fixed size with D_c=20 nm, D_s=50 nm for core-shell NPs.

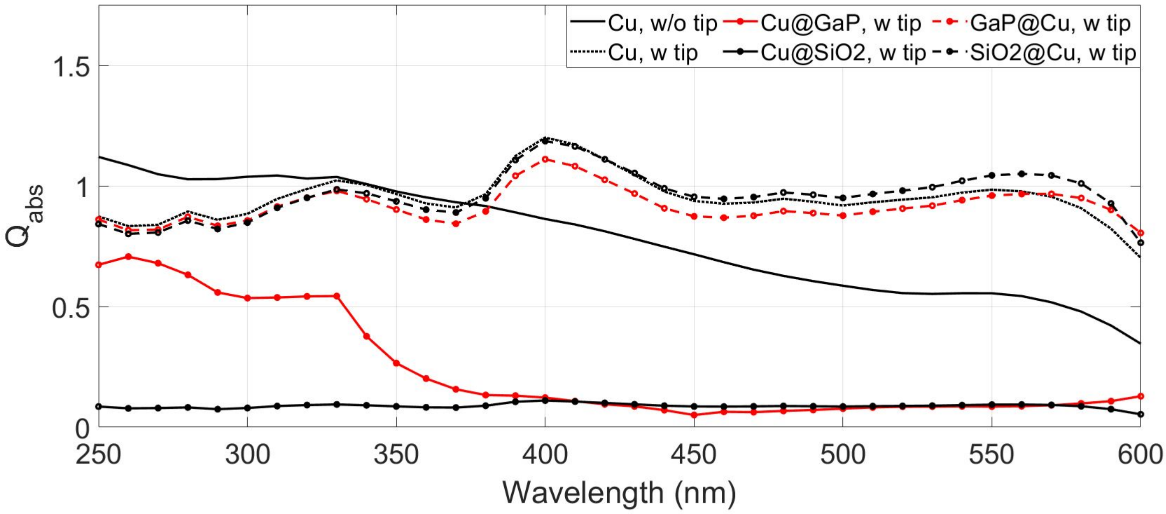

Figure D.5. Spectral Q_{abs} values for single CuNP, and dielectric pairs with both Cu core and Cu shell under Si AFM tip at coordinate (0, 0, 52) nm. Fixed size with D_c=20 nm, D_s=50 nm for core-shell NPs.

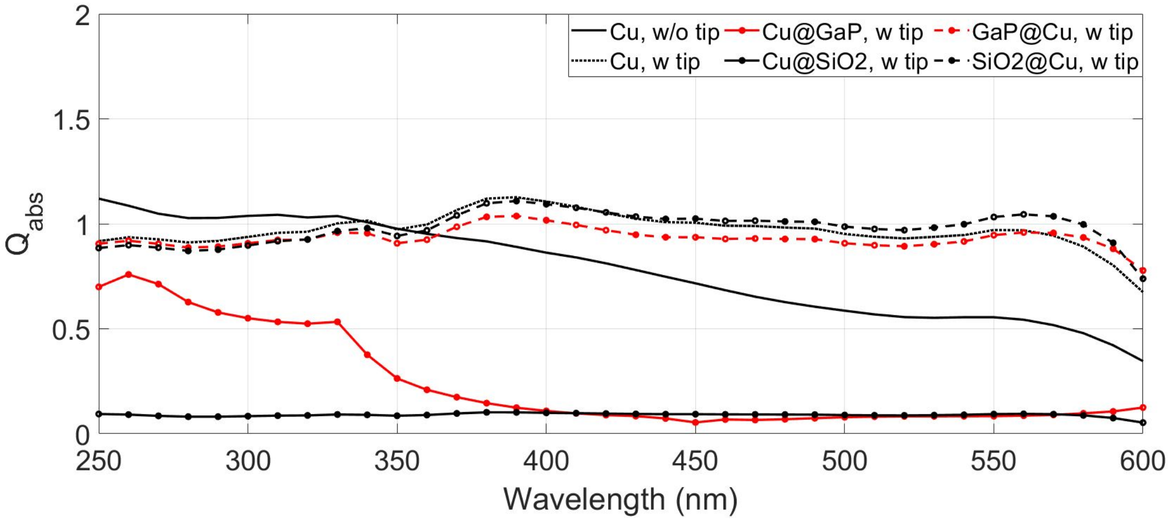

Figure D.6. Spectral Q_{abs} values for single CuNP, and dielectric pairs with both Cu core and Cu shell under GaP AFM tip at coordinate (0, 0, 52) nm. Fixed size with D_c=20 nm, D_s=50 nm for core-shell NPs.

D.1. Selected Pair: Ag@GaP Under GaP AFM Tip

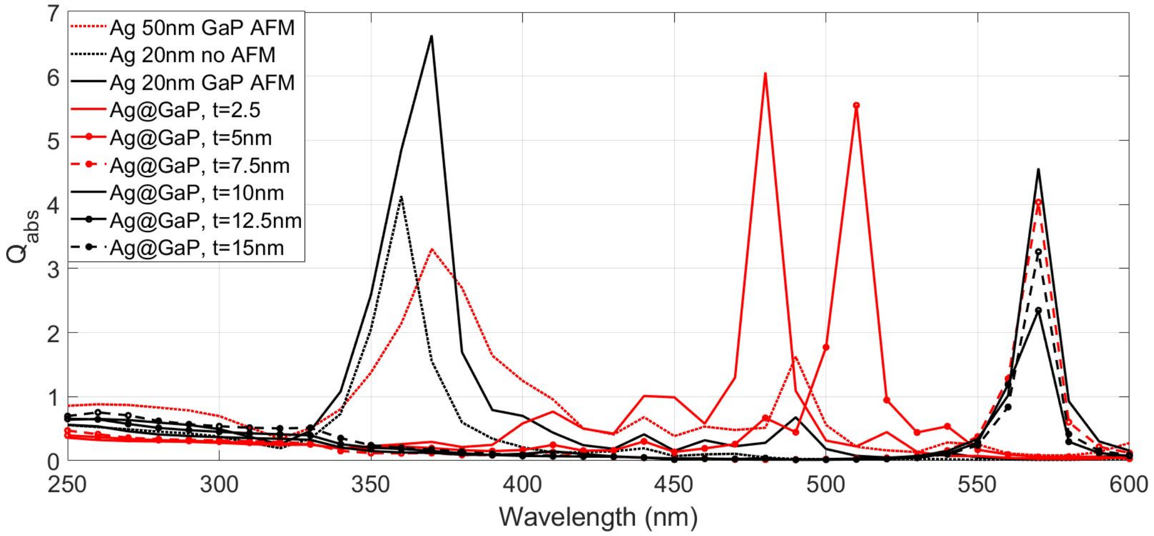

Figure D.7. Spectral Q_{abs} values of Ag core-GaP shell FC cases under an GaP tip. Shell thickness, t_s, is varied between 0-15 nm.

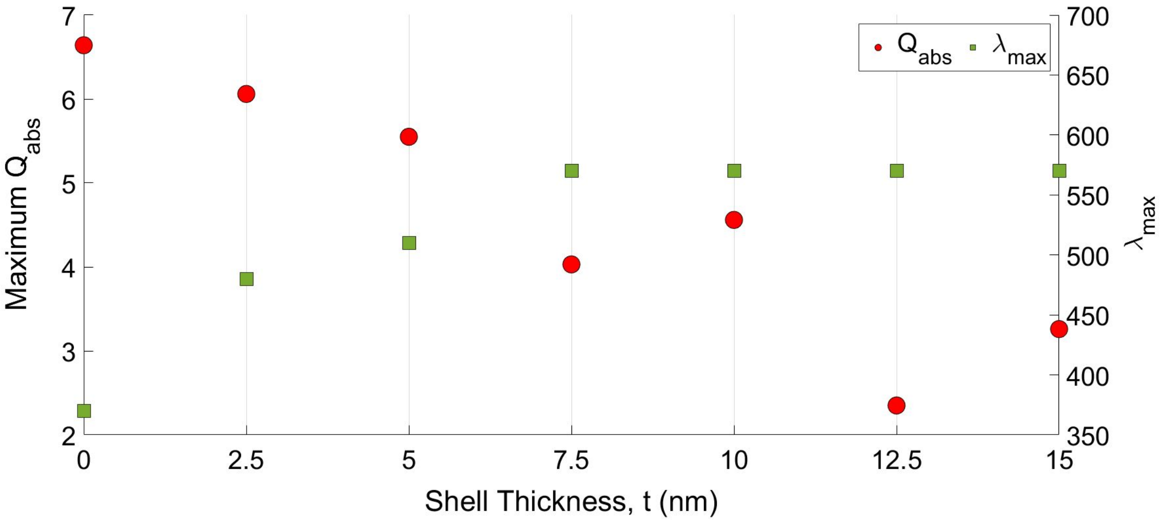

Figure D.8. Spectral Q_{abs} values of Ag core-GaP shell FC cases under an GaP tip. Shell thickness, t_s, is varied between 0-15 nm.

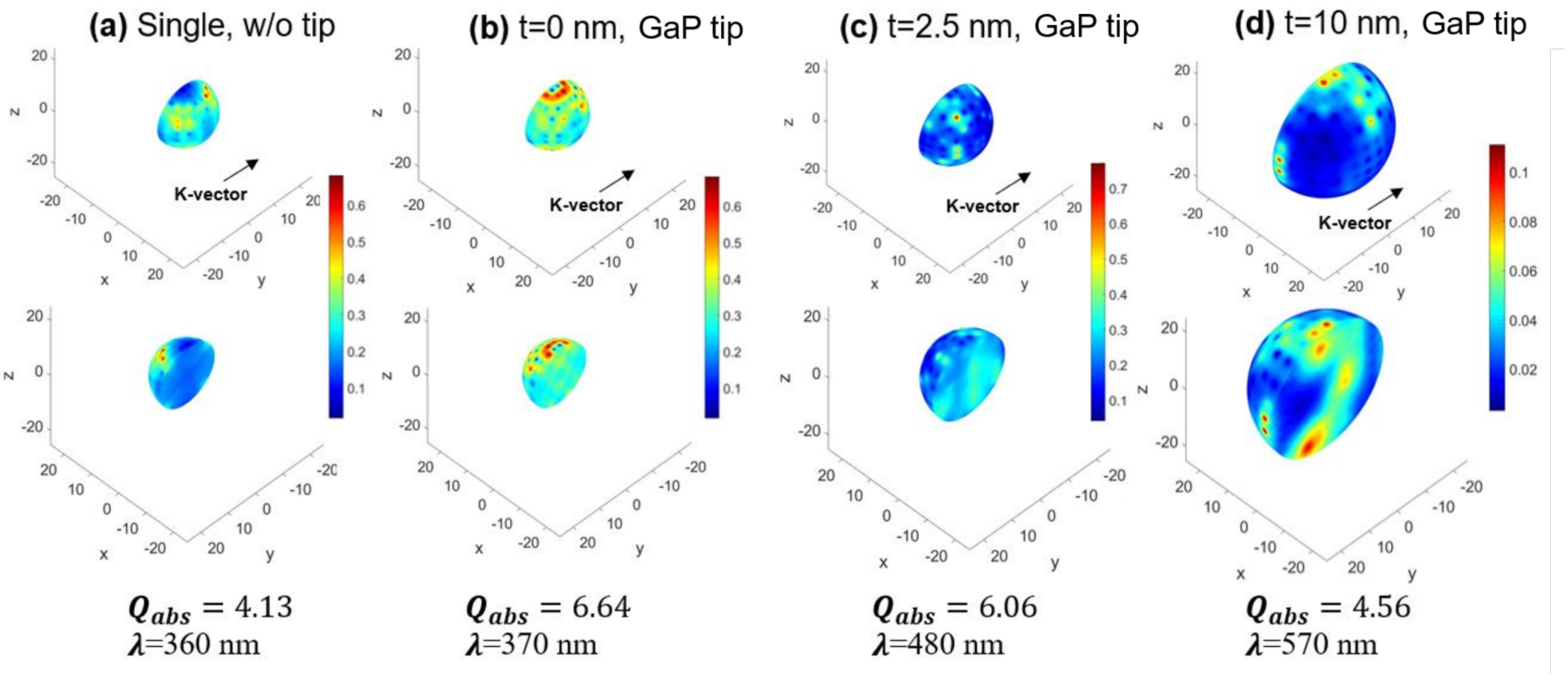

Figure D.9. Normalized field intensity plots of (a) single AgNP (D=20 nm) without the tip, (b) single AgNP (D=20 nm) with GaP tip, (c) Ag core-GaP shell D_c=20 nm, t_s=2.5 nm, with GaP tip, (d) Ag core-GaP shell D_c=20 nm, t_s=2.5 nm, with GaP tip.